Supporting Information

for

Mitigating the Climate Forcing of Aircraft Contrails by Small-Scale Diversions and Technology Adoption

Roger Teoh[1], Ulrich Schumann[2], Arnab Majumdar[1] and Marc E.J. Stettler[1]*

[1] Centre for Transport Studies, Department of Civil and Environmental Engineering, Imperial College London, London, SW7 2AZ, United Kingdom

[2] Deutsches Zentrum für Luft- und Raumfahrt, Institute of Atmospheric Physics, 82234 Oberpfaffenhofen, Germany

* Corresponding author: m.stettler@imperial.ac.uk

Supporting Information Details:

- Number of pages: 75
- Number of figures: 43
- Number of tables: 7

Nomenclature

ACC	Area control center
AEDT	Aviation Environmental Design Tool
AEIC	Aviation Emissions Inventory Code
AFR	Air-to-Fuel Ratio
AGWP	Absolute global warming potential (yr W m^{-2} kg^{-1})
AGTP	Absolute global temperature potential
ATD	Air traffic density (km^{-1} h^{-1})
ATM	Air traffic management
BADA	Base of Aircraft Data
BC	Black carbon
$c_{p,a}$	Heat capacity at constant pressure of air (= 1005 J kg^{-1} K^{-1})
$c_{p,e}$	Heat capacity for combustion products (= 1250 J kg^{-1} K^{-1})
$C_{BC,c}$	Black carbon mass concentration at the combustor exit
$C_{BC,e}$	Black carbon mass concentration at the engine exit plane
$C_{BC,i}$	Black carbon mass concentration at the instrument sampling point
C_D	Coefficient of drag
CERM	Contrail Evolution and Radiation Model
CI	Confidence interval
CoCiP	Contrail Cirrus Prediction Model
d	Distance travelled by an aircraft between waypoints (m)
D	Aerodynamic drag (N)
D_{fm}	Mass mobility exponent
D_{TEM}	Transmission electron microscopy exponent
DAC	Double annular combustor
ECMWF	European Centre for Medium-Range Weather Forecasts
EDB	Aircraft Emissions Databank
ENRI	Electronic Navigation Research Institute
EF	Contrail energy forcing (J or J m^{-1})
EI_{CO2}	Emissions index for CO_2 (= 3.15 kg kg^{-1})
EI_m	Black carbon mass emissions index (g kg^{-1})
EI_n	Black carbon number emissions index (kg^{-1})
ERA5 EDA	ECMWF Reanalysis 5, ten-member ensemble
ERA5 HRES	ECMWF Reanalysis 5, high resolution realisation
ETA	Overall propulsion efficiency
F	Aircraft engine thrust (N)
$F_{00,max}$	Maximum rated thrust at sea level with zero speed (N)
$F/F_{00,max}$	Aircraft engine thrust setting as a % of $F_{00,max}$ (also equivalent to $\dot{m}_f/\dot{m}_{f,max}$)
FA	Fractal Aggregates
FAA	Federal Aviation Administration
FOA3	First Order Approximation-3
FOX	Formation and Oxidation method
GCM	General circulation model
GMD	Geometric mean diameter
GS	Ground speed (m s^{-1})

65	GSD	Geometric standard deviation
66	H_p	Aircraft altitude (feet)
67	IAGOS	In-Service Aircraft for a Global Observing System
68	ICAO	International Civil Aviation Organization
69	ImFOX	Improved Formation and Oxidation method
70	ISSR	Ice supersaturated region
71	IWC	Specific ice water content (g m^{-3})
72	k_{TEM}	Transmission electron microscopy prefactor
73	LCV	Lower calorific value of kerosene (= 43.2 MJ kg^{-1})
74	LES	Large eddy simulations
75	LW	Longwave radiative forcing (W m^{-2})
76	Ma	Mach Number
77	m_0	Initial aircraft mass (kg)
78	$\dot{m}_f$	Aircraft fuel mass flow rate (kg s^{-1})
79	$\dot{m}_{f,max}$	Aircraft maximum fuel mass flow rate on the ground (kg s^{-1})
80	MODIS	Moderate Resolution Imaging Spectroradiometer
81	MOZAIC	Measurement of Ozone and Water Vapour by Airbus in-service aircraft
82	NMB	Normalised mean bias
83	OLR	Outgoing longwave radiation (W m^{-2})
84	P_{amb}	Ambient pressure (Pa)
85	p_{ice}	Saturation pressure over ice water surfaces (Pa)
86	P_2	Compressor inlet pressure (Pa)
87	P_3	Combustor inlet pressure (Pa)
88	PN	Particle number
89	PSD	Particle size distribution
90	q	Specific humidity (kg kg^{-1})
91	Q	Volume of exhaust gas per kg of fuel burned (m^3 kg^{-1})
92	R_0	Real gas constant for air (= 287.05 m^2 K^{-1} s^{-2})
93	R_1	Real gas constant for water vapour (= 461.51 m^2 K^{-1} s^{-2})
94	R_{earth}	Radius of the earth (= 6.371×10^6 m)
95	R^2	Coefficient of determination
96	RHi	Relative humidity with respect to ice
97	RHi_c	Enhancement of specific humidity by division of RHi_c (= 0.9)
98	ROCD	Rate of climb and descent (ft min^{-1})
99	RF	Radiative forcing (W m^{-2})
100	RF′	Local contrail radiative forcing, change in energy flux per contrail area (W m^{-2})
101	RMSE	Root mean square error
102	RNP	Required Navigation Performance
103	RSR	Reflected solar radiation (W m^{-2})
104	S	Reference wing surface area
105	S_{Earth}	Surface area of Earth (= 5.101×10^{14} m^2)
106	SAC	Single annular combustor
107	SCOPE11	Smoke Correlation for Particle Emissions CAEP11
108	SDR	Solar direct radiation (W m^{-2})
109	SFC	Specific fuel consumption (kg s^{-1} N^{-1})
110	SG	Savitzky-Golay filter

111	SN	Smoke number
112	SW	Shortwave radiative forcing ($W\ m^{-2}$)
113	SI	Supporting Information
114	T	Thrust acting parallel to the aircraft velocity vector (N)
115	T_2	Compressor inlet temperature (K)
116	T_3	Combustor inlet temperature (K)
117	T_4/T_2	Ratio of turbine inlet to the compressor inlet temperature
118	T_4	Turbine inlet temperature (K)
119	T_{amb}	Ambient temperature (K)
120	T_{fl}	Flame temperature at the combustion chamber (K)
121	TAS	True airspeed ($m\ s^{-1}$)
122	TISR	Incident solar radiation at the top of atmosphere ($J\ m^{-2}$)
123	TSR	Top net solar radiation ($J\ m^{-2}$)
124	TTR	Top net thermal radiation ($J\ m^{-2}$)
125	TEM	BADA total energy model
126	TOA	Top of the atmosphere
127	U	Horizontal wind component, U-direction ($m\ s^{-1}$)
128	UID	Aircraft engine unique identification number
129	V	Horizontal wind component, V-direction ($m\ s^{-1}$)
130	Z_{ice}	Contrail ice particle number per unit volume of air (m^{-3})
131	δ_{loss}	Correction to account for particle losses at the instrument sampling point (nm)
132	n_p	Aircraft engine compressor efficiency (= 0.9)
133	ρ_0	Material density of black carbon (= 1770 $kg\ m^{-3}$)
134	ρ_{eff}	Effective density of black carbon aggregates (= 1000 $kg\ m^{-3}$)
135	ρ_4	Density of air at the combustor exit
136	ρ_a	Ambient air density (= 1.2 $kg\ m^{-3}$)
137	τ	Contrail optical depth
138	τ_c	Optical depth of natural cirrus
139	ω	Vertical velocity ($Pa\ s^{-1}$)
140	γ	Ratio of specific heats (= 1.4)
141	π_{00}	Maximum engine pressure ratio at sea level static conditions
142	[A, B]	95% confidence interval, where A is the lower bound and B is the upper bound

Table of Contents

S1 Summary of Overall Methodology

A flow chart of the overall methodology used to achieve the aims and objectives of this study is shown in Figure S1.

In summary, aircraft trajectory data over the Japanese Airspace is provided by an aircraft activity dataset, the CARATS Open Data[1], which is further described in §S2.1. Given the 3D trajectories, the fuel consumption and engine thrust settings for each aircraft is then estimated using the Base of Aircraft Data (BADA) total energy model[2] (highlighted in §S2.3). Next, we apply the newly developed Fractal Aggregates (FA) model[3] (discussed in §S3) to estimate the aircraft black carbon (BC) number emissions index (EI_n in kg^{-1}) for specific aircraft-engine types and different engine powers. This approach improves the current assumption made by existing studies in specifying a constant EI_n for all aircraft types and operating conditions. The estimated EI_n, together with meteorological data from the European Centre for Medium-Range Weather Forecasts (ECMWF) is then used as inputs to the Contrail Cirrus Prediction Model (CoCiP)[4] to model the contrail characteristics and climate forcing with an uncertainty bound (§S4 and §S5). Finally, two mitigation strategies with different timeframes are proposed to minimise the climate forcing of aircraft contrails: (i) A small-scale strategy of selectively diverting flights with the largest contrail forcing could be implemented at present day (§S6); and (ii) a widespread adoption of new technologies such as aircraft powered by cleaner-burning double annular combustor (DAC) engines could be implemented over the long term (§S7).

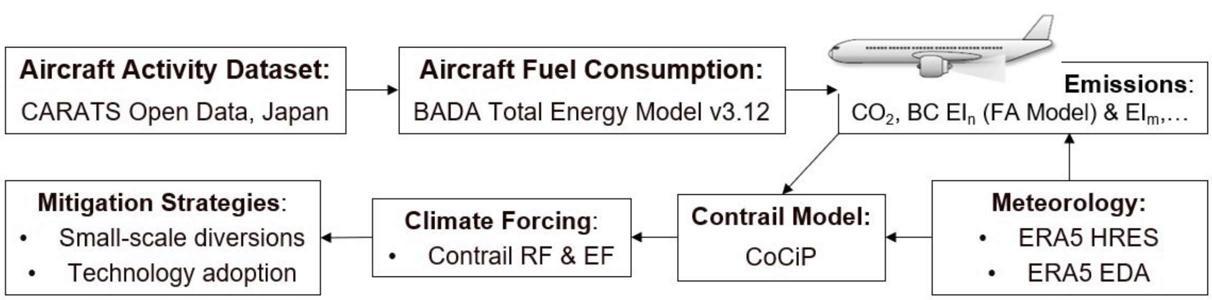

Figure S1: Flow chart of the overall methodology to achieve the aims & objectives of this study.

S2 Aircraft Activity Dataset: CARATS Open Data

S2.1 Background Information

The CARATS Open Data is an aircraft activity dataset supplied by the Electronic Navigation Research Institute (ENRI) that contains high-resolution trajectory data from individual aircraft in the four main Area Control Centers (ACC) in Japan: Tokyo, Fukuoka, Sapporo and Naha ACC. For each waypoint, the following variables are provided:

- Times in Japan Standard Time (JST, GMT+9)
- Flight ID (censored)
- Latitude, longitude (in degrees) and altitude (in feet).
- ICAO aircraft type designator.

The aircraft 3D positional data (latitude, longitude and altitude) is tracked and recorded approximately every 10 s by en-route radars, which are operated by the Ministry of Land Infrastructure and Transport's Civil Aviation Bureau. One-week periods of continuous air traffic data are recorded bimonthly from May 2012 to March 2013, and detailed time periods provided by the CARATS Open Data are presented in Table S1.

Table S1: Detailed time periods provided by the CARATS Open Data

Year	Week	Start	End	Duration (Days)
2012	1	07-May	13-May	7
	2	09-Jul	15-Jul	7
	3	03-Sep	09-Sep	7
	4	05-Nov	11-Nov	7
2013	5	07-Jan	13-Jan	7
	6	04-Mar	10-Mar	7
			TOTAL	42

* For each week, all data starts on a Monday (15:00 UTC) and ends on a Sunday (14:59 UTC)

Figure S2 shows the aircraft trajectories and a two-dimensional (2D) visualisation of the spatial domain that is covered by the CARATS Open Data, while Figure S3 provides a three-dimensional (3D) visualisation of the same data. We note that international flights (42.5% of flights in the dataset) have incomplete trajectories because the aircraft position outside the Japanese airspace are not recorded. On a given day, 57.5% of the flights have an origin-destination pair within Japan (identified when a flight records a climb, cruise and descent phase), 15.0% of flights originates from Japan to an international destination, 15.2% of flights land in Japan from an international origin, while 12.3% of the flights are overflights with no recorded take-off & landings in Japan (red trajectories in Figure S3).

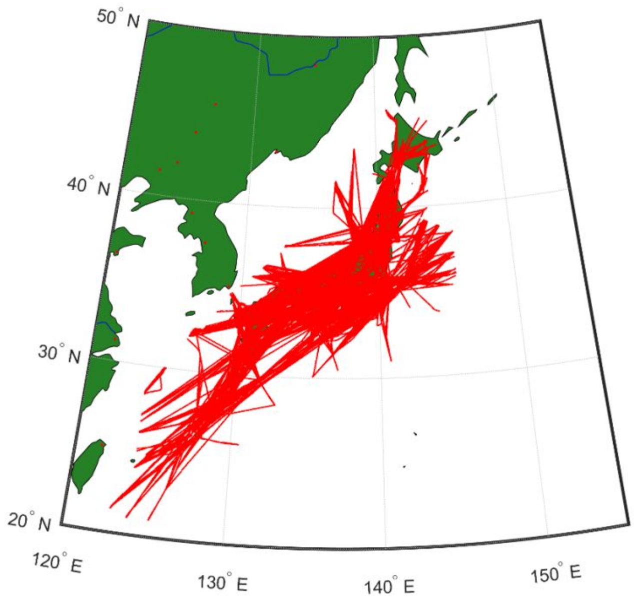

Figure S2: 2D visualisation of all flight trajectories in the CARATS Open Data on the 7th of May 2012.

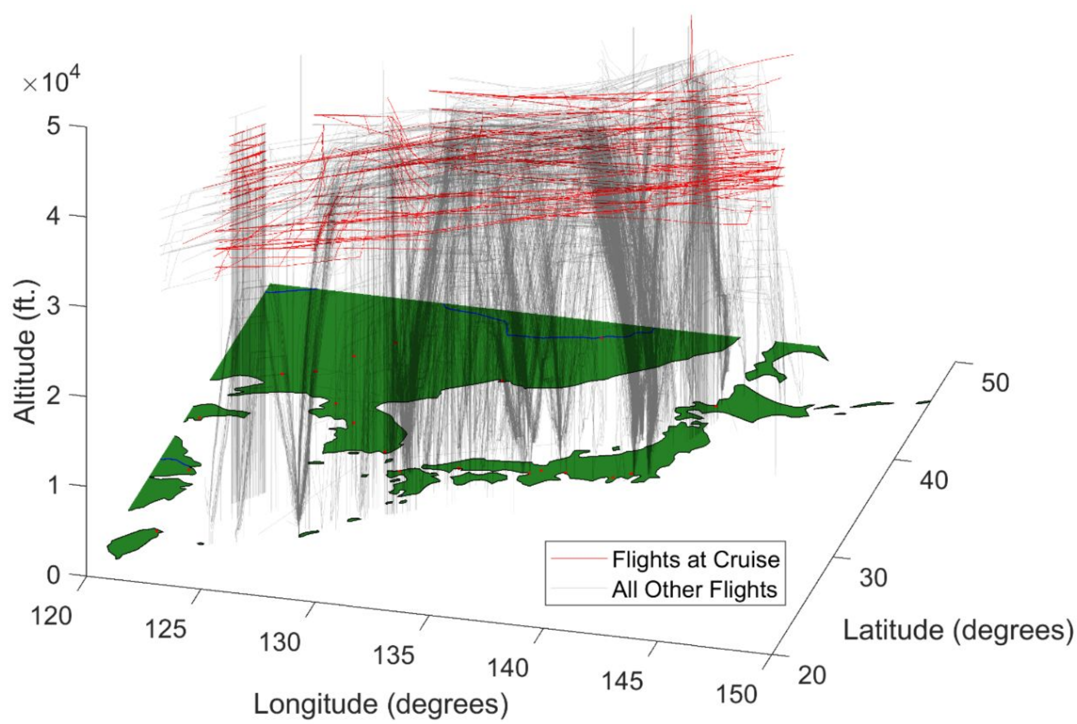

Figure S3: 3D visualisation of all flight trajectories in the CARATS Open Data on the 7th of May 2012. Flights that takes-off and/or land in Japan are marked with a black trajectory (87.7% of flights), while international overflights are marked with a red trajectory (12.3% of flights).

We note that approximately 9% of the flights in the CARATS Open Data are turboprops (Figure S4). However, given that nearly 90% of the contrails are formed at altitudes of between 7.5 km (24,500 feet) to 18.7 km (60,000 feet)[5], turboprops generally do not contribute to contrail formation as their altitudes do not exceed 25,000 feet (shown in the histogram in Figure S5).

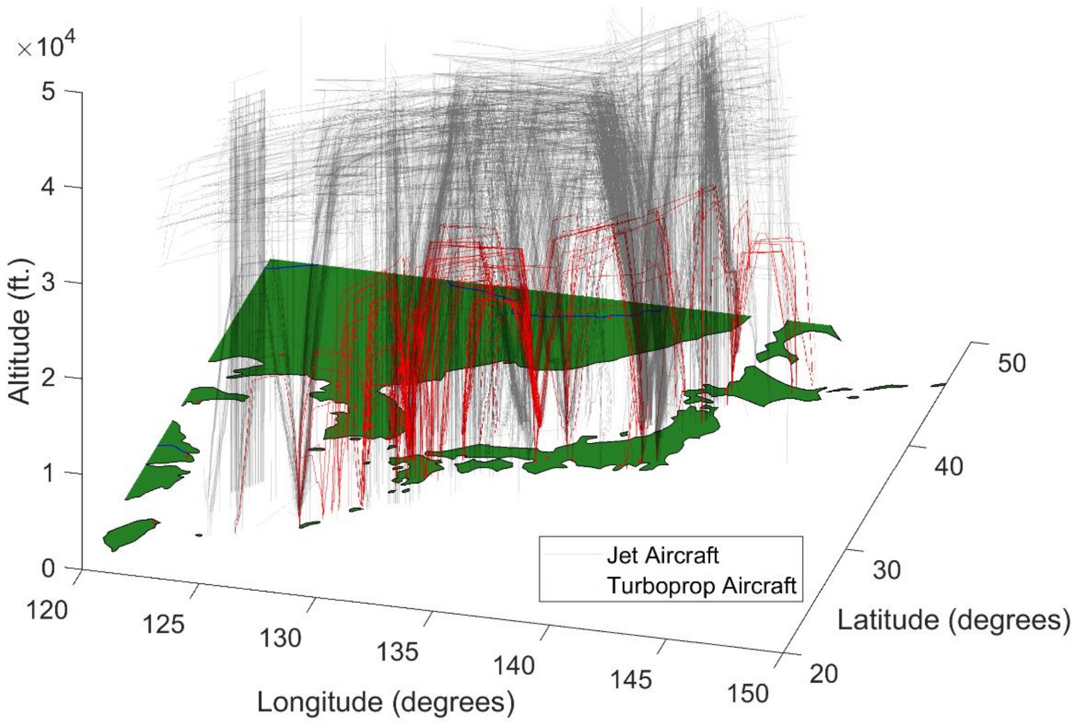

Figure S4: 3D visualisation of trajectories from turboprop aircraft (red trajectories) which generally flies at a lower altitude relative to jet aircraft (black trajectories), no higher than 25,000 feet.

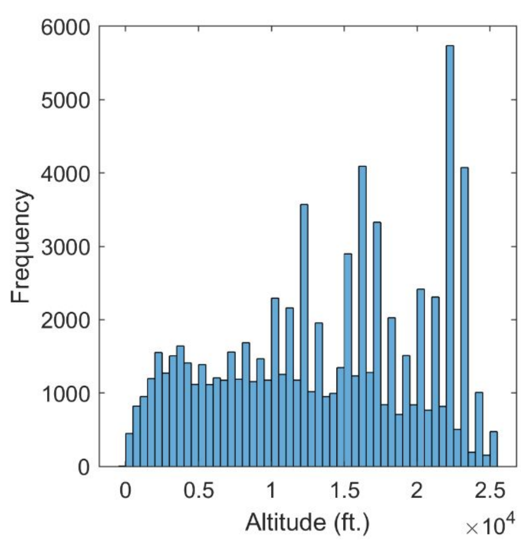

Figure S5: Altitude distribution for all waypoints from turboprop aircraft on the 7th of May 2012.

S2.2 Error Correction, Data Smoothing & Calculation of Required Parameters

Distinct patterns of erroneous data that are included in the CARATS Open Data were previously reported by the Japan Civil Aviation Bureau (JCAB)[1]. The errors include duplicated waypoints (0.24% of the dataset), waypoints with zero altitudes (0.06% of the dataset; example shown in Figure S6a) or above the service ceiling altitude of a given aircraft type (0.002% of the dataset), and an unrealistic rate of climb and descent (ROCD) that exceed the aircraft specifications (0.04% of the dataset; example shown in Figure S6b).

Firstly, for sets of waypoints originating from the same flight, consecutive rows of data that have the same longitude, latitude, and altitude are flagged as duplicates and removed. We then attempt to correct the altitude of erroneous waypoints with an unrealistic ROCD or altitude (zero in mid-flight or above the service ceiling altitude of an aircraft) via linear interpolation if the calculated ROCD between waypoint (i-1) to (i+j) is computed to be within the aircraft performance specifications of the given aircraft type provided by Eurocontrol[2]. A constraint of j_{max}=5, which limits the correction algorithm to look up to 5 waypoints ahead is typically sufficient to rectify up to 80% of the erroneous waypoints. The remaining 20% of erroneous waypoints that do not fit with the criterion (of having a realistic ROCD after interpolation) are subsequently removed from the dataset. Figure S6 provide examples of the flight trajectories (in red) that have been corrected with the above methodology.

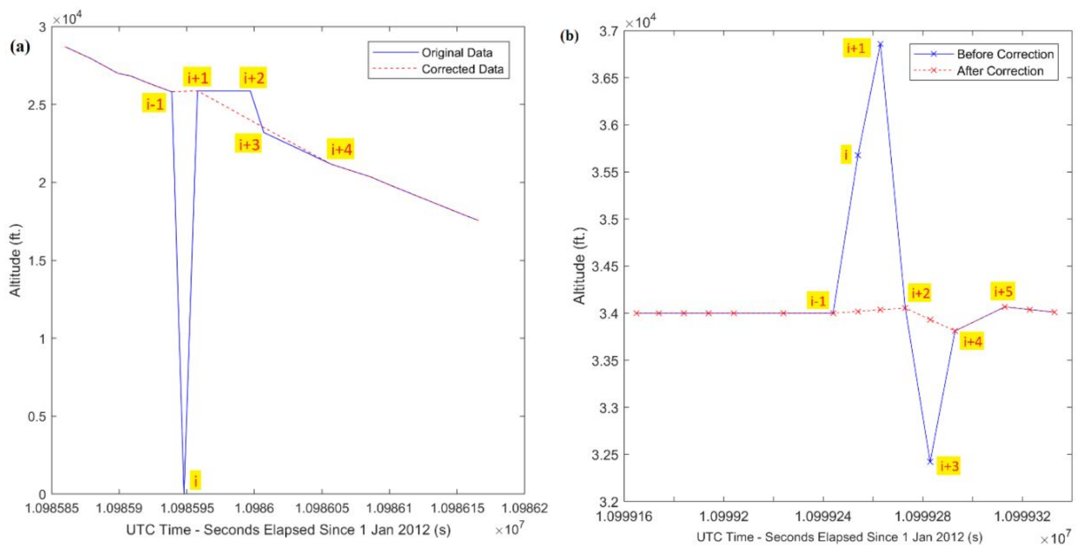

Figure S6: Examples of erroneous waypoints (trajectories in blue) with (a) zero altitudes, and (b) an unrealistic ROCD that exceeds their respective aircraft performance. The erroneous waypoints are subsequently corrected using linear interpolation (trajectories in red).

The presence of aircraft positional errors (mainly the latitude and longitude) was highlighted[6] in the CARATS Open Data. This is due to the use of radar to track aircraft positions where the radar accuracy is ± 4.0 NM (or ± 7400 m) for a Required Navigation Performance (RNP) Type 4 standard[7]. Given that aircraft positional data is recorded every 10s throughout the flight, we note that these errors are non-cumulative and are likely to average out[8]. Nevertheless, prior to estimating several variables such as the distance between waypoints, ground speed (GS), and true air speed (TAS), we smoothed the latitude, longitude and altitude data using a Savitzky-Golay (SG) filter, which uses a linear least squares methodology to fit successive segments of data points with a low-degree polynomial[9]. The SG filter is able to better preserve the shape and features of the original dataset, while the order of polynomial provides the flexibility to focus on narrower or broad features[10,11]. These characteristics are an advantage relative to a simple moving average, where a bias could be introduced if the second derivative of the underlying dataset or function is non-zero[10]. For the smoothing of aircraft positional data (latitude, longitude and altitude), we used a time period of 12 corresponding to approximately two minutes of data[8], and a second order polynomial to capture narrower features, such as cases where aircraft trajectories change rapidly. Figure S7a presents the data smoothing results with a SG filter for an aircraft trajectory in a holding pattern. The results show that the use of a second-order polynomial in the SG filter is superior relative to a simple moving average in terms of capturing narrower features in the smoothed trajectory.

The distance travelled by an aircraft between waypoints (*d*) is calculated using the Haversine Formula[12],

$$d\,[\mathrm{m}] = \left({d_{\mathrm{vertical}}}^2 + {d_{\mathrm{horizontal}}}^2\right)^{0.5} \tag{S1}$$

$$\text{where}\quad d_{\mathrm{vertical}}[\mathrm{m}] = \mathrm{Altitude(i+1)} - \mathrm{Altitude(i)}, \tag{S2}$$

$$d_{\mathrm{horizontal}}[\mathrm{m}] = R_{\mathrm{earth}} \times [2 \times \mathrm{atan2}(\sqrt{a}, \sqrt{1-a})], \text{ and} \tag{S3}$$

$$a = \left(\sin\left(\frac{\delta\,\mathrm{lat}}{2}\right)\right)^2 + \cos(\mathrm{lat1})\cos(\mathrm{lat2})\left(\sin\left(\frac{\delta\,\mathrm{lon}}{2}\right)\right)^2, \tag{S4}$$

where R_{earth} is the radius of Earth (6.371×10^6 m), and δlat and δlon are the difference in latitude and longitude between two waypoints in radians.

Next, the GS is computed by dividing the distance travelled with the time difference between two waypoints, while the TAS is converted from the GS using ambient wind data from the European Centre for Medium-Range Weather Forecast (ECMWF) ERA5 ten-member ensemble (EDA)[13],

$$\mathrm{V_{TAS}}\ [\mathrm{m\ s^{-1}}] = \begin{pmatrix} \mathrm{TA}S_{\mathrm{Lon}} \\ \mathrm{TA}S_{\mathrm{Lat}} \end{pmatrix} = \begin{pmatrix} \mathrm{G}S_{\mathrm{Lon}} \\ \mathrm{G}S_{\mathrm{Lat}} \end{pmatrix} - \begin{pmatrix} \mathrm{ERA5_U} \\ \mathrm{ERA5_V} \end{pmatrix}, \tag{S5}$$

where $\mathrm{ERA5_U}$ and $\mathrm{ERA5_V}$ are the U- and V-component of wind from the ERA5 EDA reanalysis.

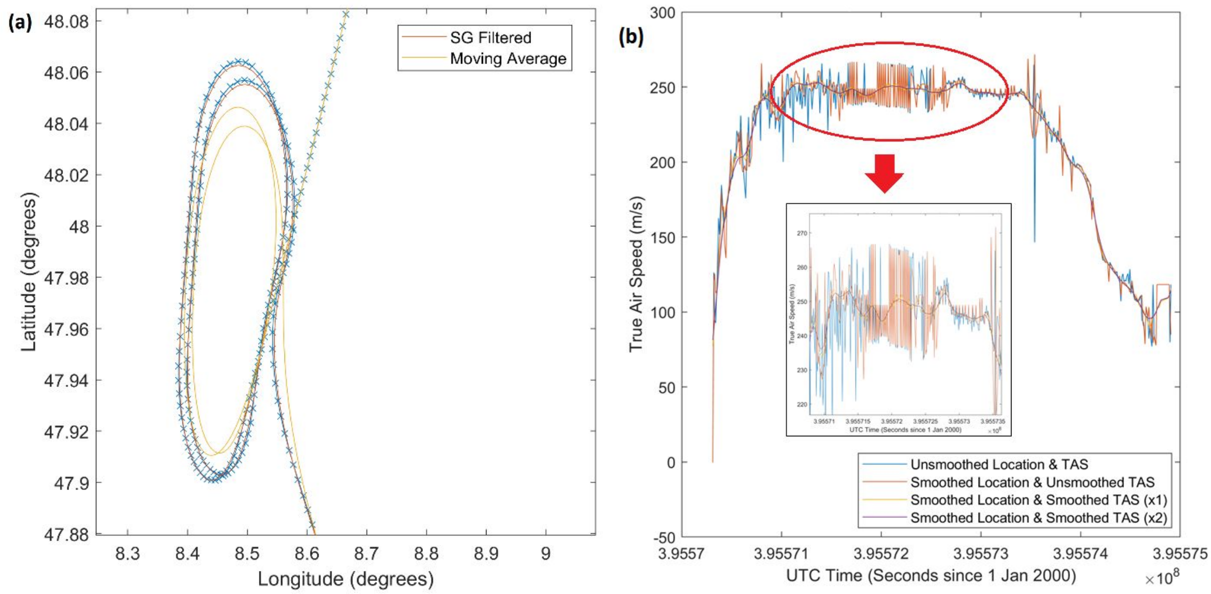

Figure S7: Examples of the smoothed trajectories using the SG filter on the (a) latitude and longitude (second-order polynomial), and (b) TAS (first-order polynomial) from an example flight in the CARATS Open Data. For both cases, the SG filter is applied with a time period of 12.

Given that time data is reported as an integer second in the CARATS Open Data, errors due to the rounding of time will lead to additional uncertainties and noise in the estimated ground speed and TAS. We note that this error source could be significant as each waypoint is only 10s apart. To address this, the estimated TAS is smoothed again with the SG filter (120 s time period[8] and a first-order polynomial to minimise the effects of unrealistic peaks and troughs in the TAS), and then re-smoothed for the second time similar to the methodology of the European Commission[14]. Figure S7b shows that the large noise in the TAS is significantly reduced following the use of a SG filter, and this is crucial in obtaining realistic values for the estimated fuel mass flow rate ($\dot{m}_{\mathrm{f}}$) as will be shown in Figure S8 in §S2.3.

Finally, we calculate the Mach number (Ma) for each waypoint,

$$\mathrm{Ma} = \frac{\mathrm{V}_{\mathrm{TAS}}}{\sqrt{\kappa \mathrm{R} T_{\mathrm{amb}}}}, \tag{S6}$$

where κ is the ratio of heat capacities of air (1.4), R_0 is the real gas constant for air (287.05 $\mathrm{m}^2\ \mathrm{K}^{-1}\ \mathrm{s}^{-2}$), and T_{amb} is the ambient temperature (in Kelvins) obtained from the ERA5 EDA. Using Eq. (S6), the Ma is estimated to range from 0.70 to 0.85 during the cruise phase of flight (Figure S8).

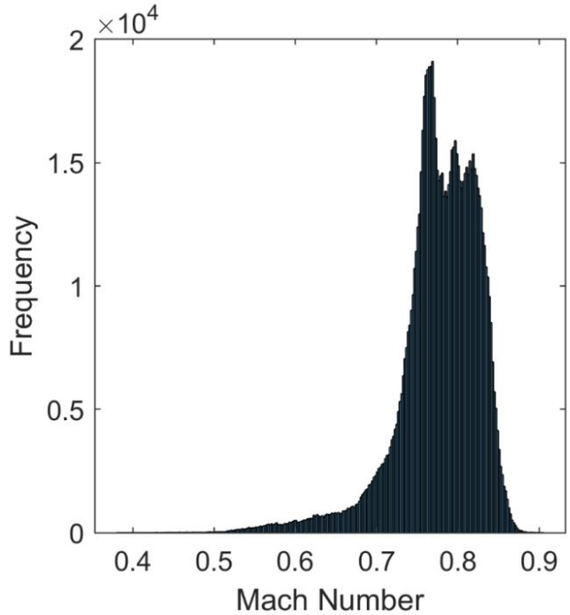

Figure S8: Mach number distribution for all waypoints above 25,000 feet on the 7th of May 2012.

S2.3 Calculation of Aircraft Mass and Fuel Consumption

The Base of Aircraft Data Version 3.12 (BADA 3) total energy model (TEM) by Eurocontrol[2] is used to estimate the thrust, $\dot{m}_{\mathrm{f}}$ (in units of kg s^{-1}) and aircraft mass (m) for each waypoint,

$$(T - D)V_{\mathrm{TAS}} = \mathrm{m}\mathrm{g}_0 \frac{dh}{dt} + \mathrm{m}V_{\mathrm{TAS}} \frac{dV_{\mathrm{TAS}}}{dt}, \tag{S7}$$

where T is the thrust acting parallel to the aircraft velocity vector (in units of N), D is the aerodynamic drag (in units of N), h is the aircraft altitude (in units of m), and g_0 is the gravitational acceleration (9.81m s^{-2}). The initial aircraft mass (m_0) is estimated iteratively, assuming an average aircraft load factor of 75.5% (ref.[15]). Eq. (S7) is rearranged to calculate T,

$$T_{\text{climb \& cruise}} = D + \frac{1}{V_{\mathrm{TAS}}}\left[m g_0 \frac{dh}{dt} + m V_{\mathrm{TAS}} \frac{dV_{\mathrm{TAS}}}{dt}\right], \tag{S8}$$

$$\text{where } D = \frac{C_{\mathrm{D}} \rho {V_{\mathrm{TAS}}}^2 S}{2} \tag{S9}$$

C_{D} is the coefficient of drag, S is the reference wing surface area, and ρ is the ambient air density. Details on the C_{D} for specific aircraft types are provided in Eurocontrol[2]. Eq. (S8) is only applicable when the aircraft is operating at climb and cruise conditions. Given that the Eq. (S8) could produce negative thrust values, T in the descent phase is calculated as follows,

$$T_{\text{descent}} = \mathrm{C}_{\mathrm{T,des}} \times T_{\text{max,climb}}, \tag{S10}$$

where $C_{T,\mathrm{des}}$ is the aircraft-specific altitude descent thrust coefficient and $T_{\text{max,climb}}$ is the maximum climb thrust at a given atmospheric condition. For further methodological details on T_{descent}, the reader is referred to Eurocontrol[2].

Next, the thrust specific fuel consumption (SFC) and $\dot{m}_{\mathrm{f}}$ is calculated for each waypoint,

$$\mathrm{SFC}_{\text{jet}} = C_{f1}\left(1 + \frac{V_{\mathrm{TAS}}}{C_{f2}}\right) \tag{S11}$$

$$\mathrm{SFC}_{\text{turboprop}} = C_{f1}\left(1 - \frac{V_{\mathrm{TAS}}}{C_{f2}}\right)\left(\frac{V_{\mathrm{TAS}}}{1000}\right) \tag{S12}$$

$$\dot{m}_{\text{f,climb}} = \mathrm{SFC} \times T\ , \tag{S13}$$

$$\dot{m}_{\text{f,cruise}} = \mathrm{SFC} \times T C_{fcr}, \tag{S14}$$

$$\dot{m}_{\text{f,descent}} = C_{f3}\left(1 - \frac{H_p}{C_{f4}}\right), \tag{S15}$$

where $\mathrm{H_p}$ is the altitude (in units of feet), and the thrust specific fuel consumption coefficients ($\mathrm{C_{f1}}$, $\mathrm{C_{f2}}$, $\mathrm{C_{f3}}$ and $\mathrm{C_{f4}}$) and cruise fuel flow correction coefficient ($\mathrm{C_{fcr}}$) are provided in Eurocontrol[2]. Figure S9 provides an example of the estimated $\dot{m}_{\mathrm{f}}$ for one flight in the CARATS Open Data. The use of smoothed inputs of aircraft positional data (latitude, longitude and altitude) and TAS is crucial as it provides more realistic values of acceleration ($\frac{dV_{\mathrm{TAS}}}{dt}$) and ROCD ($\frac{dh}{dt}$), and therefore significantly reduced the noise in the estimated $\dot{m}_{\mathrm{f}}$.

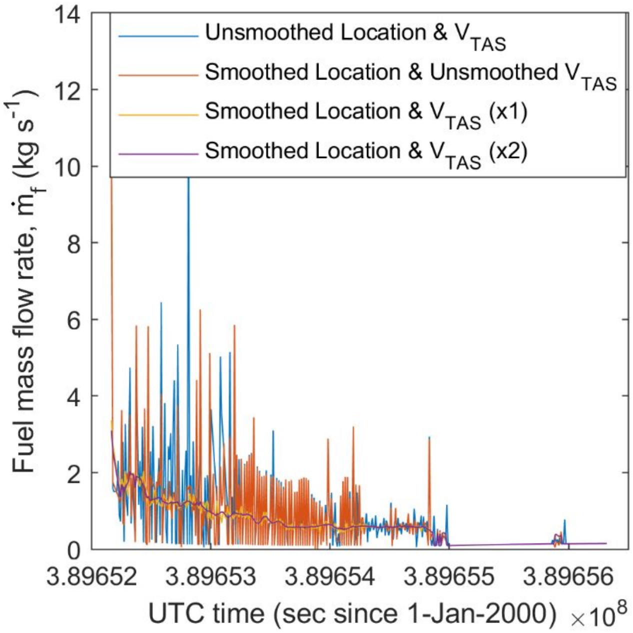

Figure S9: Example of the estimated $\dot{m}_f$ for one flight using the BADA3 TEM, where unsmoothed and smoothed inputs of aircraft positional data (latitude, longitude and altitude) and TAS are used.

To understand the error correction methodology and the use of smoothed parameters (such as the 3D aircraft positional data and TAS previously described in §S2.2), we validated the estimated $\dot{m}_f$ (from this study) against the $\dot{m}_f$ of one flight in the CARATS Open Data that was separately estimated and available from Shigetomi et al.[6]. Although the $\dot{m}_f$ from Shigetomi et al.[6] is also estimated with the BADA3 TEM, several key differences are noted: (i) the aircraft positional data is collected using a more accurate GPS sensor (with an average error value of ± 8m) instead of en-route radars (with an accuracy of ± 4.0 NM, or ± 7400 m); (ii) data on the ambient upper atmospheric winds was retrieved from the Japan Meteorological Agency's Numerical Weather Archive; and (iii) a constant aircraft mass of 208,700 kg was assumed for all waypoints. To be consistent with the inputs used by Shigetomi et al.[6], we assumed a constant aircraft mass (208700 kg) for all waypoints in this validation, but modelled the aircraft mass to decrease over time (according to the total fuel consumption between two waypoints) for every other application in this study. The validation results (presented in Figure S10) shows that the estimated $\dot{m}_f$ (from this study) is in good agreement with the validation dataset[6]. For each waypoint, the estimated $\dot{m}_f$ in the cruise phase is within ± 10%, and the total fuel consumption for this specific flight agrees to ± 3%.

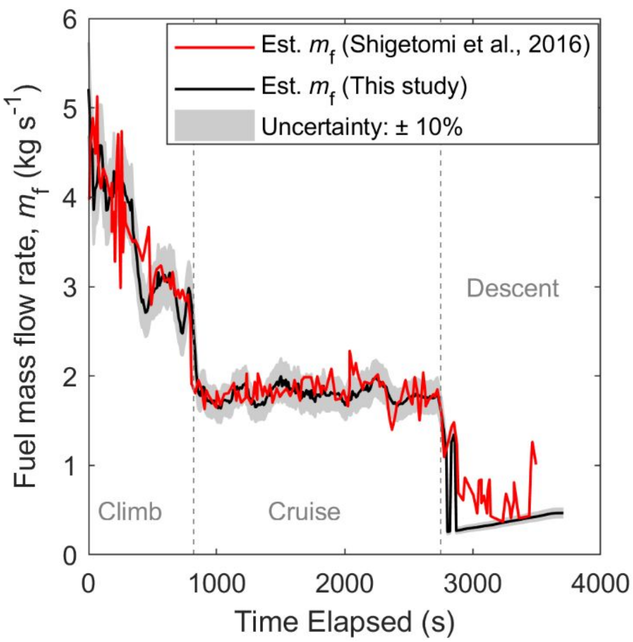

Figure S10: Validation of the $\dot{m}_{\mathrm{f}}$ (estimated using the error correction and data smoothing methodology described in §S2.2 and §S2.3) against data from Shigetomi et al. [6] where $\dot{m}_{\mathrm{f}}$ is estimated from GPS-collected aircraft positional data for one flight (Flight ID FLT2279 on the 14th of July 2012).

Following the estimation of $\dot{m}_{\mathrm{f}}$, the engine thrust settings ($\frac{F}{F_{00,\mathrm{max}}}$, where F_{00},max is the maximum rated thrust at sea level and zero speed) is then calculated based on the assumption that it is interchangeable[16–19] with the ratio of $\dot{m}_{\mathrm{f}}$ to the engine-specific maximum fuel flow on the ground ($\frac{\dot{m}_{\mathrm{f}}}{\dot{m}_{\mathrm{f,max}}}$), of which the aircraft-engine assignments are matched using compiled data from Stettler et al.[20], and $\dot{m}_{\mathrm{f,max}}$ is obtained from the ICAO Aircraft Emissions Databank (EDB)[21]. This assumption ($\frac{F}{F_{00,\mathrm{max}}} = \frac{\dot{m}_{\mathrm{f}}}{\dot{m}_{\mathrm{f,max}}}$) was previously validated by Stettler et al.[18], where data from the ICAO EDB showed that the above assumption holds for most of certified engines at the four certification test points (7%, 30%, 85% and 100% $\frac{F}{F_{00,\mathrm{max}}}$). In this study, the $\frac{F}{F_{00,\mathrm{max}}}$ (or $\frac{\dot{m}_{\mathrm{f}}}{\dot{m}_{\mathrm{f,max}}}$) is used to estimate the combustor inlet pressure (P_3) and the air-to-fuel ratio (AFR), both of which are required to estimate the BC geometric mean diameter (GMD) and the BC number emissions index ($\mathrm{EI_n}$ in kg^{-1}), as will be described in §S3.

For each waypoint, uncertainties in the $\dot{m}_{\mathrm{f}}$ is accounted for by propagating the uncertainties in T_{amb} and the upper atmospheric winds (speed and direction) that are provided by the ERA5 EDA meteorological dataset, as will be discussed in §S4.4. Over the six one-week periods, the total fuel burn and CO_2 emissions attributable to the Japanese airspace is 681.86 ± 0.03 Gg and 2147.9 ± 0.1 Gg respectively. We note that this uncertainty bound does not include the known limitations of BADA3[2] where the fuel consumption could be underestimated when aircraft are flying at suboptimal altitudes as discussed in the main text.

Finally, we calculate the overall propulsion efficiency (ETA) for each waypoint,

$$\mathrm{ETA} = \frac{T\,V_{\mathrm{TAS}}}{\dot{m}_{\mathrm{f}}\,\mathrm{LCV}}, \tag{S16}$$

where LCV is the lower calorific value of kerosene (43.2 MJ kg^{-1}). For waypoints in the descent phase, we note that the ETA computed using Eq.(S16) provides unrealistic values of greater than 1 because BADA3 calculates T at the descent phase as a function of H_p and are independent from the acceleration and ROCD. To resolve this, we assigned the ETA values for each waypoint at the descent phase to be zero because the engine is nearly at idle without providing any useful thrust.

S2.4 Identification of Aircraft Powered by a Double Annular Combustor

Aircraft powered by a Singular Annular Combustor (SAC) gas turbine engine are representative of the current aviation fleet (around 84% of the aircraft recorded in the CARATS Open Data), while the remaining 16% of aircraft in the CARATS Open Data is powered by a DAC engine. The main difference between SAC and DAC engines, for the purpose of this study, are their different BC emissions characteristics: ground measurements that are available show that the BC mass emissions index (EI_m in g kg^{-1}) from a SAC engine tends to follow a U-shaped curve, with higher EI_m at very low and high thrust settings, with a minimum around $\frac{F}{F_{00,\mathrm{max}}} \approx 30\%$ (ref.[16,18,22]). Conversely, DAC engines operate in two stages: at low $\frac{F}{F_{00,\mathrm{max}}}$, the pilot stage operates with a low AFR (fuel-rich combustion) and through-flow velocity where only the outer annulus of the combustor is fuelled; and at $\frac{F}{F_{00,\mathrm{max}}} > 25\%$, the main stage is activated with higher AFR (leaner combustion) and through-flow velocity[23]. As the engine is operating at the lean combustion mode, an oxygen-rich environment (higher AFR) decreases the formation rate and increase the oxidation rate of BC[24]. Therefore, the BC emissions characteristics for a DAC engine is similar to a SAC engine at the pilot stage (where EI_m increases with $\frac{F}{F_{00,\mathrm{max}}}$), but the BC EI_n, EI_m and GMD significantly decrease during the main combustion stage[25,26], as shown in SI §S3.2.

Data from the ICAO EDB[21] is used to identify aircraft powered by a DAC. On the whole, 19 aircraft gas turbine engines were identified as a DAC, which the names and their respective unique identification number (UID) for DAC engines are compiled in Table S2.

Table S2: Identification of aircraft gas turbine engines with a DAC.

No.	Engine Name (UID No.)	No.	Engine Name (UID No.)
1	CFM56-5B1/2 (2CM016)	11	GE90-110B1 (7GE097)
2	CFM56-5B1/2P (3CM020)	12	GE90-113B (7GE098)
3	CFM56-5B2/2 (2CM017)	13	GE90-115B (7GE099)
4	CFM56-5B2/2P (4CM037)	14	GE90-76B (2GE052, 3GE062, 6GE087)
5	CFM56-5B3/2P (4CM038)	15	GE90-77B (3GE059, 3GE063, 6GE088)
6	CFM56-5B4/2 (2CM018)	16	GE90-85B (2GE053, 3GE064, 6GE089)
7	CFM56-5B4/2P (3CM021)	17	GE90-90B (3GE060, 3GE065, 6GE090)
8	CFM56-5B6/2 (2CM019)	18	GE90-92B (3GE061, 3GE066)
9	CFM56-5B6/2P (3CM022)	19	GE90-94B (6GE091, 8GE100)
10	CFM56-5B9/2P (7CM050)		

The aircraft-engine assignments list that was previously compiled by Stettler et al.[20] is then used to link the DAC engines (identified in Table S2) to specific aircraft types. In particular, we note that the Boeing 777 series are primarily powered by the General Electric GE90-90B DAC engine. Although alternative SAC engine types such as the Pratt & Whitney PW4000 and the Rolls-Royce Trent 800 were also used to power the first-generation Boeing 777's (such as the B777-200 and B777-300), we have assumed that all Boeing 777's in the CARATS Open Data are powered by the GE90-90B DAC engine. This is justified because the GE90-90B is the only engine option provided to power the second-generation Boeing 777's (such as the B777-300ER and B777F). Based on this assumption, we note that approximately 16% of the aircraft in the CARATS Open Data are powered by a DAC.

S3 Estimating the Aircraft BC Number Emissions Index

S3.1 Existing Methodologies available to Estimate the Aircraft BC EI_n

Fractal Aggregates (FA) Model

The Fractal Aggregates (FA)[3] model, presented in Eq. (2) in the main text, is used to estimate the BC EI_n, which is identified as a critical input parameter for contrail models[4]. The FA model was previously validated[3] with measurements of BC emissions from two aircraft gas turbines at ground and cruise conditions using data from the SAMPLE III.2[25] and NASA ACCESS[27] experimental campaigns.

For each waypoint, the FA model estimates the EI_n from the mass emissions index (EI_m in g kg^{-1}), particle size distribution (PSD) and morphology. However, given that the input parameters, such as the EI_m, GMD, geometric standard deviation (GSD), the mass-mobility exponent (D_{fm}), as well as the transmission electron microscopy prefactor and exponent (k_{TEM} and D_{TEM}) are only measured from a small-number of aircraft-engine combinations, we review existing models and develop predictive relationships to estimate these parameters at cruise conditions (presented in the §S3.2).

SCOPE11 Methodology

The Smoke Correlation for Particle Emissions CAEP 11 (SCOPE11) methodology[28] was recently made available to estimate the aircraft BC: (i) EI_m at the landing and take-off cycle (LTO) using measurements of smoke number (SN); and (ii) the EI_n from the EI_m, GMD and GSD. The equation used for component (ii) is outlined below,

$$\mathrm{EI_n} = \frac{\mathrm{EI_m}}{(\frac{\pi}{6})\rho_{\mathrm{eff}}\mathrm{GMD}^3 \exp\left(4.5(\ln(\mathrm{GSD}))^2\right)}, \tag{S17}$$

where $\rho_{\mathrm{eff}} = 1000\ \mathrm{kg\ m}^{-3}$ is the effective density of BC aggregates, while the GSD is specified to be constant at 1.8 across engine thrust settings. For component (i), the equations used to estimate the EI_m, Eq. (S23) to Eq. (S26), will be shown in the next subsection. The exit plane GMD is estimated as follows,

$$\mathrm{GMD[nm]} = \mathrm{a}\ \mathrm{C_{BC,C}}^{b}, \tag{S18}$$

where $a = 5.08 \pm 0.55$ nm, $b = 0.185 \pm 0.015$, and $C_{BC,C}$ (in units of μg m^{-3}) is the BC mass concentration at the combustor exit and is estimated from the equation below,

$$\mathrm{C_{BC,c}} = \mathrm{C_{BC,e}}(1 + \beta_{\mathrm{mix}})\frac{\rho_4}{\rho_a}, \tag{S19}$$

where $C_{BC,e}$ is the BC mass concentration at the engine exit plane estimated using Eq. (S24) in the next subsection, ρ_4 is the density of air at the combustor exit, and ρ_a is the ambient air density. We note that the use of Eq. (S18) to estimate the GMD could be limited as it requires inputs of $C_{BC,C}$ which have large uncertainties, as will be shown in the next subsection.

Validation of the FA Model and SCOPE11 Methodology

To select an appropriate methodology to estimate the BC EI_n, we compared the performance of the FA model (Eq. 1 in the main text) and component (ii) of the SCOPE11 methodology (Eq. S17) by validating the estimated EI_n against the EI_n measured on the ground (SAMPLE III.2[25]) and cruise (NASA ACCESS[27]) conditions. The metrics used for this validation are the coefficient of determination (R^2), root mean square error (RMSE) and normalised mean bias (NMB). For both methodologies, the EI_n are estimated using measurements of the BC EI_m, GMD and GSD, which are provided by the SAMPLE III.2 and NASA ACCESS datasets. Input parameters governing the aggregate morphology (D_{fm}, k_{TEM} and D_{TEM}) that are required by the FA model are fixed at a constant value for reasons that will be described in §S3.2. For further methodological details of this validation and the datasets involved, the reader is referred to the literature[3].

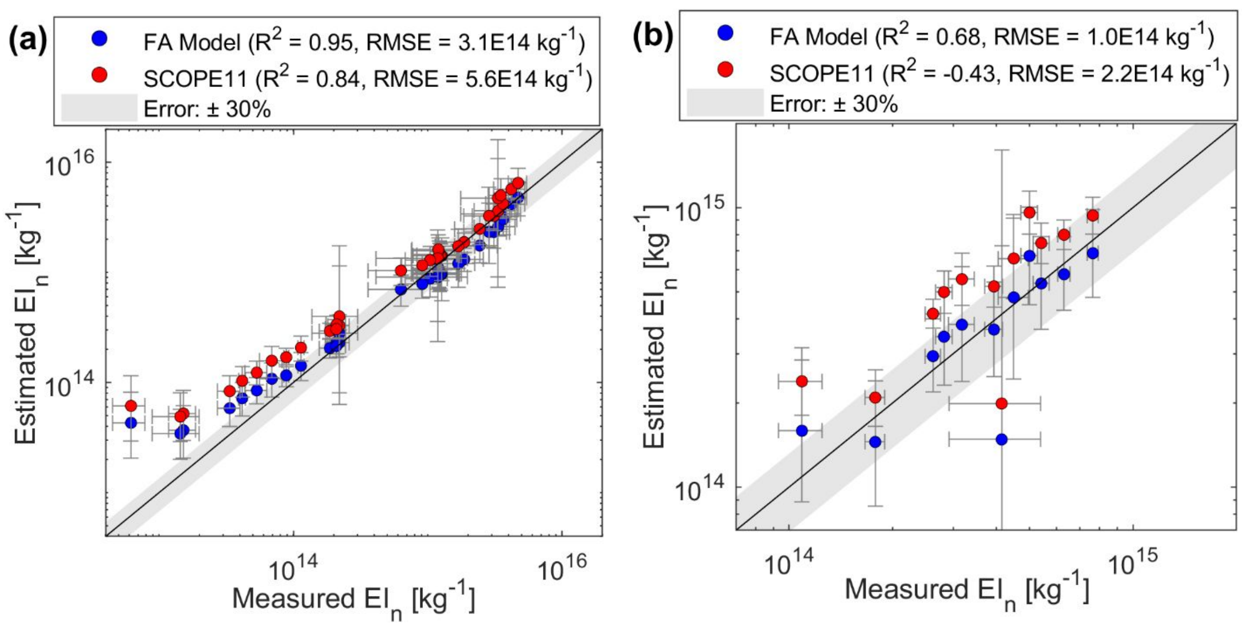

Figure S11: Validation of the FA model and SCOPE11 methodology against EIn measured (a) on the ground using data from the SAMPLE III.2 campaign[25], and (b) at cruise conditions using data from the NASA ACCESS campaign[27]. Error bars denote precision errors from repeated measurements at a 95% CI.

Figure S11 presents the validation results for the FA model and SCOPE11 methodology: For both ground and cruise conditions, the aircraft BC EI_n is more accurately predicted using the FA model (Ground: $R^2 = 0.95$, $RMSE = 3.10 \times 10^{14}\ kg^{-1}$, $NMB = +26.6\%$; Cruise: $R^2 = 0.69$, $RMSE = 1.01 \times 10^{14}\ kg^{-1}$, $NMB = +2.4\%$) relative to the SCOPE11 methodology (Ground: $R^2 = 0.84$, $RMSE = 5.57 \times 10^{14}\ kg^{-1}$, $NMB = +81.1\%$; Cruise: $R^2 = -0.43$, $RMSE = 2.16 \times 10^{14}\ kg^{-1}$, $NMB = +46.0\%$). The slight improvement in performance from the FA model could be due to the use of more accurate coefficients for the BC aggregate morphology (i.e. D_{fm}, k_{TEM} and D_{TEM}), as evaluated in Teoh et al.[3]. We note that the FA model was derived from the theory of fractal aggregates[3] and does not require any calibration or fitting with experimental datasets. Given that both models are subjected to the same input variables (EI_m, GMD and GSD) but with slightly different coefficients, the FA model predicts the same pattern as the SCOPE11 but decreased by a roughly constant factor.

S3.2 Review and Specification of Model Input Parameters for the FA Model

The following input parameters are required by the FA model to estimate BC EI_n from aircraft: engine thrust settings ($\frac{F}{F_{00,max}}$), BC mass emissions index (EI_m in g kg^{-1}), mass-mobility exponent (D_{fm}), BC material density (ρ_0), GMD, GSD, and the k_{TEM} and D_{TEM} prefactor-exponent pair. Existing models and datasets are reviewed in this subsection to develop predictive relationships in estimating these parameters at cruise conditions.

Assessment of Different BC EI_m Estimation Methods

A number of models are available to estimate the BC mass concentration (C_{BC}, in units of mg m^{-3}) for aircraft powered by SAC engines. The BC EI_m is then calculated by multiplying C_{BC} with the volume of exhaust gas per kg of fuel burned (Q, in units of m^3 kg^{-1}). For example, several methodologies[28–30] rely on aircraft SN measurements provided by the ICAO EDB to estimate C_{BC}. SN is quantified optically by comparing the difference in reflectance of a filter paper before and after it is stained by the engine exhaust[31]. However, SN measurements in the ICAO EDB are limited to the four certification test points at 7%, 30%, 85% and 100% $\frac{F}{F_{00,max}}$ measured on the ground. Several studies have also found that the First Order Approximation-3 (FOA3) could underestimate the EI_m by up to one order of magnitude at low SNs[16,20,30]. This is because the filtration efficiency significantly deteriorates when the mobility diameter (d_m) of BC aggregates is < 100 nm (ref.[30]) and the GMD emitted by modern aircraft typically lies between 10 and 50 nm (ref.[32,33]). Therefore, the SN values for some engine types (provided by the ICAO EDB) could be zero at all four certification test points[21]. Although Agarwal et al.[28] have shown that the SCOPE11 model successfully addressed the issue of zero SN and improved the C_{BC} estimates relative to earlier SN methodologies[29,30], it is not calibrated to model the EI_m at cruise conditions. The respective methodologies that rely on SN measurements are summarised as follows,

1) <u>First Order Approximation Method – FOA3</u>

$$C_{BC}\left[\frac{mg}{m^3}\right] = 0.0694(SN)^{1.24}. \tag{S20}$$

2) <u>Correlations from Stettler et al.</u>[30]

$$C_{BC}\left[\frac{mg}{m^3}\right] = 0.0472(SN)^{1.42} \quad \text{, for GMD = 60 nm} \tag{S21}$$

$$C_{BC}\left[\frac{mg}{m^3}\right] = 0.236(SN)^{1.126} \quad \text{, for } 20 \le \text{GMD} \le 30 \text{ nm} \tag{S22}$$

3) <u>SCOPE11 Methodology:</u>

Firstly, the C_{BC} at the instrument sampling point ($C_{BC,i}$) is calculated,

$$C_{BC,i}\left[\frac{\mu g}{m^3}\right] = \frac{648.4\exp(0.0766 \times SN)}{1 + \exp(-1.098(SN - 3.064))} \tag{S23}$$

A system loss correction factor (k_{slm}) is then applied as a multiplicative factor to calculate the C_{BC} at the engine exit plane ($C_{BC,e}$),

$$C_{BC,e} = C_{BC,i} \times k_{slm} \tag{S24}$$

$$\text{where } k_{slm} = \ln\left(\frac{a_1 C_{BC,i}(1 + \beta_{mix}) + a_2}{C_{BC,i}(1 + \beta_{mix}) + a_3}\right), \tag{S25}$$

$a_1 = 3.219 \pm 0.135$, $a_2 = 312.5 \pm 119.1 \mu g\ m^{-3}$, $a_3 = 42.6 \pm 19.4\ \mu g\ m^{-3}$, and β_{mix} is the bypass ratio for mixed-flow engines (zero otherwise). Finally, the $EI_{m,e}$ is calculated by multiplying $C_{BC,e}$ with the volume of exhaust gas per kg of fuel burned (Q),

$$EI_{m,e} = C_{BC,e} \times Q, \tag{S26}$$

$$\text{where } Q = 0.776AFR + 0.767, \text{ for engines with an unmixed exhaust nozzle,} \tag{S27}$$

$$Q_{mixed} = 0.776AFR(1 + \beta_{mixed}) + 0.767 \text{ for engines with a mixed nozzle.} \tag{S28}$$

The predictive relationship for the Air-to-Fuel Ratio (AFR) as a function of $\frac{F}{F_{00,\mathrm{max}}}$ has been validated[18,34] and is calculated as follows,

$$\mathrm{AFR}\left[\frac{\mathrm{kg-air}}{\mathrm{kg-fuel}}\right] = \left(0.0121\left(\frac{F}{F_{00,\mathrm{max}}}\right) + 0.008\right)^{-1}. \tag{S29}$$

Alternatively, the Formation and Oxidation (FOX)[18] and the Improved FOX (ImFOX)[16] methods estimate the C_{BC} based on the thermodynamic and physical mechanisms by which BC is formed and oxidised. Although these methods do not rely on SN inputs, they were calibrated to model the EI_m for aircraft gas turbine engines with a SAC, which are representative of the current aviation fleet (around 84% of the aircraft recorded in the CARATS Open Data). For estimates of EI_m at cruise, the FOX method prescribes the Döpelheuer & Lecht scaling method[35], while the ImFOX method circumvents the use of this scaling equation by using different relationships for the AFR versus $\frac{F}{F_{00,\mathrm{max}}}$ at cruising altitude compared to on the ground. The FOX and ImFOX methodologies are summarised as follows:

4) <u>Formation and Oxidation Method (FOX):</u>

The $C_{BC,i}$ in the FOX method is calibrated using BC measurements from the instrument sampling point, and is calculated as follows,

$$C_{BC,i}\left[\frac{\mathrm{mg}}{\mathrm{m}^3}\right] = \dot{m}_f\left(A_{form}e^{\left(\frac{-6390}{T_{fl}}\right)} - A_{ox}\mathrm{AFR} \times e^{\left(-\frac{19778}{T_{fl}}\right)}\right) \tag{S30}$$

where A_{form} and A_{ox} are constants of 356 mg s kg^{-1} m^{-3} and 608 mg s kg^{-1} m^{-3} respectively, the AFR is calculated using Eq. (S29), and T_{fl} is the flame temperature at the combustion chamber,

$$T_{fl}[\mathrm{K}] = 0.9T_3 + 2120. \tag{S31}$$

T_3 is the combustor inlet temperature,

$$T_3[\mathrm{K}] = T_2\left(\frac{P_3}{P_2}\right)^{\frac{\gamma-1}{\gamma n_p}}, \tag{S32}$$

where γ is the ratio of specific heats (1.4), and n_p is the compressor efficiency (0.9), P_3 is the combustor inlet pressure, P_2 and T_2 are the respective compressor inlet pressure and temperature, and are calculated as follows,

$$P_3[\mathrm{atm}] = P_2(\pi_{00} - 1)\left(\frac{F}{F_{00,\mathrm{max}}}\right) + P_2, \tag{S33}$$

$$P_2[\mathrm{atm}] = P_{\mathrm{amb}}\left(1 + \frac{\gamma - 1}{2}{M_a}^2\right)^{\frac{\gamma}{\gamma - 1}}, \tag{S34}$$

$$T_2[\mathrm{K}] = T_{\mathrm{amb}}\left(1 + \frac{\gamma - 1}{2}{M_a}^2\right), \tag{S35}$$

where π_{00} is the maximum engine pressure ratio at SLS conditions (obtained from the ICAO EDB[21]), P_{amb} is the ambient pressure, T_{amb} is the ambient temperature, and Ma is the aircraft Mach number. We note that these thermodynamic equations (T_{fl}, T_3, P_3, P_2 and T_2) are widely used in the literature to model the thermodynamic performance of jet engines[18,28,36], and have also been validated with data provided by flight data recorders[18,34].

To scale the C_{BC} from ground to cruise conditions, the Döpelheuer & Lecht scaling equation[35] is used,

$$\mathrm{C_{BC}}\left[\frac{\mathrm{mg}}{\mathrm{m}^3}\right] = \mathrm{C_{BC,ref}}\left(\frac{\mathrm{AFR_{ref}}}{\mathrm{AFR}}\right)^{2.5}\left(\frac{P_3}{P_{3,\mathrm{ref}}}\right)^{1.35}\left(\frac{e^{20000/T_{\mathrm{fl}}}}{e^{20000/T_{\mathrm{fl,ref}}}}\right), \tag{S36}$$

where the reference condition is set at 100% $\frac{F}{F_{00,\mathrm{max}}}$. The BC EI_m is then calculated using Eq. (S26), where Q is calculated as follows,

$$\mathrm{Q} = 0.776(\mathrm{AFR}) + 0.877. \tag{S37}$$

5) <u>Improved FOX Method (ImFOX)</u>

The $C_{BC,i}$ in the ImFOX method is calculated as follows,

$$C_{\mathrm{BC,i}}\left[\frac{\mathrm{mg}}{\mathrm{m}^3}\right] = \dot{m}_{\mathrm{f}} \times e^{(13.6 - \mathrm{H})} \times \left(A_{\mathrm{form}}e^{\left(\frac{-6390}{T_4}\right)} - A_{\mathrm{ox}}\mathrm{AFR} \times e^{\left(-\frac{19778}{T_4}\right)}\right), \tag{S38}$$

where A_{form} at cruise and A_{ox} are constants of 295 mg s kg^{-1} m^{-3} and 608 mg s kg^{-1} m^{-3} respectively, H is the fuel hydrogen mass (in percentage terms) which is approximately 13.8% for conventional fuels), and T_4 is the turbine inlet temperature,

$$T_4[\mathrm{K}] = 490 + 42266(\mathrm{AFR})^{-1}, \tag{S39}$$

where the AFR for ground and cruise conditions are separately calculated (below) to circumvent the need for a cruise scaling equation such as the Döpelheuer & Lecht equation.

$$\mathrm{AFR_{ground}} = 71 - 35.8\left(\frac{F}{F_{00,\max}}\right) \tag{S40}$$

$$\mathrm{AFR_{cruise}} = 55.4 - 30.8\left(\frac{F}{F_{00,\max}}\right) \tag{S41}$$

We note that Eq. (S39) was derived specifically for the ImFOX method using data from one engine type (CFM56-2-C1), which could be highly uncertain and might not be applicable to other engine types.

Finally, the BC EI_m and Q are calculated using Eq. (S26) and Eq. (S37) respectively.

Given the need to estimate the EI_m at cruise conditions, we have conducted further assessments between the FOX and ImFOX methods by validating them with the limited number of aircraft EI_m measured at cruising altitudes. These measurements were mainly collected by the SULFUR[37,38] and NASA ACCESS [27] experimental campaigns, containing 9 data points from 4 different engines.

Figure S12 presents the validation results for the FOX and ImFOX methods. For the CFM56-2-C1 engine, the cruise EI_m is better predicted using the ImFOX (NMB = +19.4%) relative to the FOX method (NMB = -38.4%), which is likely due to the fact that the ImFOX used the same dataset for model calibration. However, for the remaining three engines which were operated at a reduced engine power, the estimated EI_m have a closer resemblance to the FOX (NMB = +37.2%) than the ImFOX method (NMB = +134.2%). Therefore, we are unable to verify if the accuracy of the ImFOX estimated EI_m holds for other aircraft-engine combinations because of the limited number of cruise measurements available.

For all four engines, the ImFOX estimated EI_m at cruise conditions are consistently higher than the FOX method across the range of $\frac{F}{F_{00,\max}}$. Although this appears to be inconsistent when compared with existing studies, which showed that the FOX generally estimates a higher EI_m on the ground relative to the ImFOX[16,22], the smaller cruise EI_m estimates from the FOX is likely due to the use of the Döpelheuer & Lecht scaling equation[35]. While there are suggestions that this scaling equation significantly underestimated cruise EI_m by 84% when compared with measured data from the CFM56-2-C1 engine[16], we were unable to verify this statement based on the results in Figure S12a, which showed that the average NMB from the FOX is -38.4%. The significant underestimation of EI_m (-84%), as suggested in the literature[16] could be due to a different specification of the ground reference condition for the Döpelheuer & Lecht scaling equation[35]. When cruise EI_m measurements from all nine points in Figure S12 are included, however, the overall NMB from the FOX (-13.2%) suggest that the potential underestimation in cruise EI_m as a result of the Döpelheuer & Lecht scaling equation[35] might be less significant. This could also be attributed to the FOX tending to overpredict the EI_m on the ground, thereby reducing the effects of the Döpelheuer & Lecht scaling equation in underestimating the cruise EI_m.

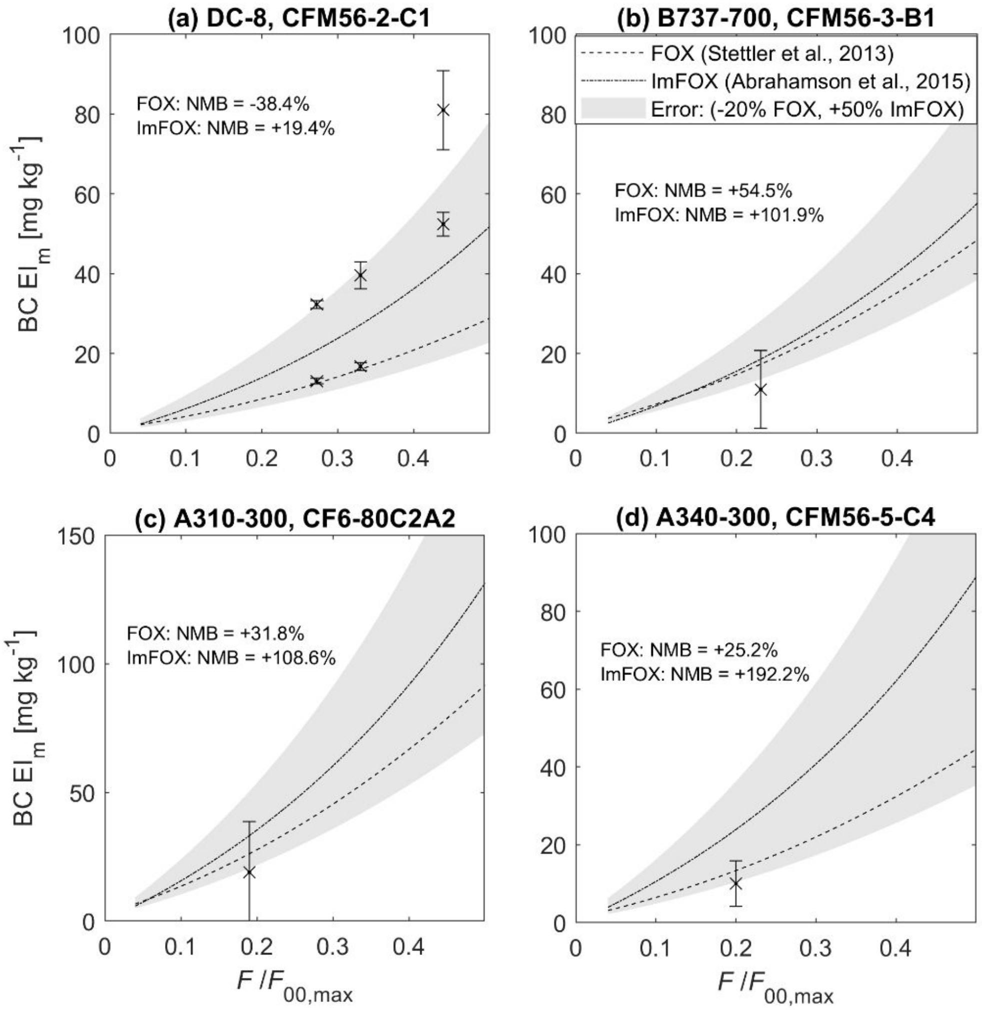

Figure S12: Validation of the FOX and ImFOX methods against cruise EI_m measurements from the: (a) NASA ACCESS; and (b) (c) and (d) SULFUR experimental campaigns. Error bars denote precision errors from repeated measurements with a 95% CI. Detailed data tables can be found in Table S3.

Table S3: Compilation of cruise EI_m measurements from the NASA ACCESS (6 data points) and SULFUR (3 data points) experimental campaigns.

Aircraft (Engine)	Measured EI_m (mg kg^{-1})							
	Average	Std dev (1.96σ)	$\dot{m}_f$ (kg s^{-1})	$\dot{m}_{f,max}$ (kg s^{-1})	$F/F_{00,max}$	π_{00}	FL (km)	Mach No
DC-8 (CFM56-2-C1)[27]	80.97	9.859	0.373	0.849	0.439	23.5	10.7	0.84
	39.58	3.352	0.28	0.849	0.33	23.5	10.7	0.725
	32.26	1.019	0.231	0.849	0.272	23.5	10.7	0.6
	52.44	2.999	0.373	0.849	0.439	23.5	10.7	0.84
	16.71	0.980	0.28	0.849	0.33	23.5	10.7	0.725
	13.08	0.706	0.231	0.849	0.272	23.5	10.7	0.6
B 737-300 (CFM56-3-B1)[37]	11	9.800	0.213	0.946	0.23	22.44	7.92	0.49
A310-300 (CF6-80C2A2)[37]	19	19.600	0.4	2.152	0.19	27.79	7.92	0.53
A340-300 (CFM56-5C4)[38]	10	5.880	0.2912	1.456	0.2	31.1	9.5	0.64

Overall, the validation results show that further work is required to improve the accuracy of aircraft EI_m estimates at cruise, but it is beyond the scope of this research. Given the uncertainties in the available EI_m estimation methodologies and the lack of understanding on the uncertainty distribution, we assume that the EI_m is uniformly distributed between -20% and +50% of the FOX and ImFOX estimates respectively. This uncertainty bound covers 8 out of the 9 data points when error bars are accounted for (Figure S12). Further details on the methodology of applying these uncertainties can be found in §S3.4.

We also note that the data used to calibrate the FOX and ImFOX methods were not corrected for particle line losses, which therefore represent measurements at the instrument sampling point and could underestimate EI_m by up to a factor of two[28]. Although a system loss correction factor (k_{slm}, estimated as a function of C_{BC}) was proposed[28] to correct for the EI_m to represent emissions at the engine exit plane, we have decided against applying it because of the already large uncertainties in the estimated C_{BC} and EI_m. Instead, we assume that the effects of k_{slm} are captured in the asymmetrical uncertainty bounds of the EI_m (shown in Figure S12).

Finally, given that DAC engines have different emissions characteristics relative to SAC engines, the models and predictive relations that was previously specified (FOA3, correlations from Stettler et al.[30], SCOPE11, FOX and ImFOX) cannot be used to estimate the EI_m and GMD for aircraft powered by a DAC. However, to the best of our knowledge, there are currently no models that are available to estimate the EI_m for aircraft with a DAC engine, which represents up to 16% of the aircraft in the CARATS Open Data. Using measurements of EI_m from experimental campaigns[25,26], we interpolated the EI_m in the pilot stage as a function of T_4/T_2, the ratio of turbine inlet to the compressor inlet temperature, for reasons that will be shown in the next subsection, while assuming an average EI_m of 3.25 mg kg^{-1} in the lean combustion stage. An exponential trendline is selected to estimate the EI_m for DAC engines in the pilot stage (as shown in Figure S13 and Eq. S42) because it provided the highest R^2 (0.866) relative to a quadratic ($R^2 = 0.846$) relationship, while a best-fit linear trendline gives a negative EI_m when the T_4/T_2 is below 2.08.

$$\mathrm{EI}_{\mathrm{m,DAC}}[\mathrm{mg\ kg}^{-1}] = 0.0032\exp(3.6956\tfrac{T_4}{T_2}), \qquad \tfrac{T_4}{T_2} < 2.85 \tag{S42}$$

As will be shown in Figure S15b, the DAC engine operates in pilot stage when T_4/T_2 is below 2.85. To calculate the T_4/T_2 for each waypoint, we first calculate T_4 [28],

$$T_4[\mathrm{K}] = \frac{\mathrm{AFR}\, c_{\mathrm{p,a}}\, T_3 + \mathrm{LCV}}{c_{\mathrm{p,e}}\,(1 + \mathrm{AFR})}, \tag{S43}$$

where $c_{p,a}$ (1005 J kg^{-1} K^{-1}) and $c_{p,e}$ (1250 J kg^{-1} K^{-1}) are the heat capacity at constant pressure of air and for combustion products, LCV is the lower calorific value of kerosene (43.2 MJ kg^{-1}), and AFR and T_3 are calculated using Eq. (S29) and Eq. (S32) respectively.

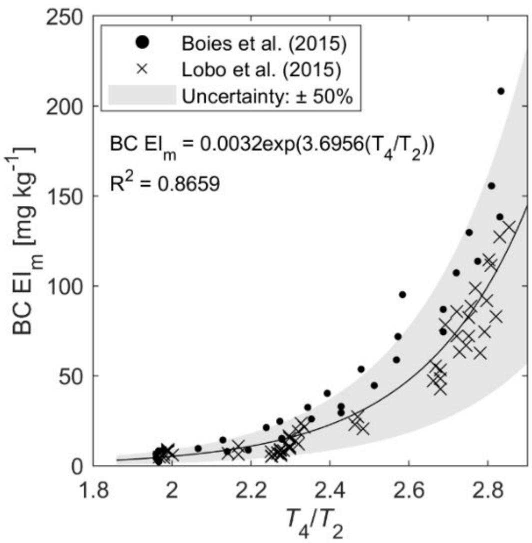

Figure S13: Predictive relations to estimate the BC EI$_m$ (applicable for ground and cruise conditions) as a function of T_4/T_2 for DAC engines in the pilot stage. Data used in this figure is extracted from the literature[25,26].

Particle Size Distribution and Morphology

For both ground and cruise conditions, the GMD of BC emitted by SAC engines (and DAC engines in the pilot stage) typically range from 15 nm to 45 nm, and increases linearly with $\frac{F}{F_{00,\max}}$ [22,26,27,32], while DAC engines operating in the main combustion stage have a constant GMD of around 18 to 23nm [25].

For SAC engines, we compiled measurements of GMD collected at ground[26,32] and cruise conditions[27], and developed a new predictive relationship to estimate the GMD at the engine exit plane as a function of T_4/T_2,

$$\mathrm{GMD_{SAC}}[\mathrm{nm}] = 2.5883\left(\frac{T_4}{T_2}\right)^2 - 5.3723\left(\frac{T_4}{T_2}\right) + 16.721 + \delta_{\mathrm{loss}}, \qquad \text{(S44)}$$

where T_4 is calculated using Eq. (S43) and δ_{loss} is a correction factor used to account for particle losses at the instrument sampling point. To quantify δ_{loss}, we used: (i) data from the SAMPLE III.2[25] and NASA ACCESS[27] campaigns to compare the measured GMD at the instrument sampling point with the estimated GMD at the engine exit plane (calculated with the SCOPE11 method[28], Eq. (S18), using measurements of $\mathrm{EI_m}$); and (ii) data from Durdina et al.[22] where both the measured GMD at the instrument sampling point and the corrected GMD at the engine exit plane are presented. Given the absence of a systematic trend for δ_{loss} versus T_4/T_2 (shown in Figure S14), δ_{loss} is assumed to be uniformly distributed between -3 and -8.5 nm, which covers 95% of the data points when error bars are included.

Figure S15a shows that Eq. S44 is applicable to engines operating at both ground and cruise conditions because the engine parameters have been non-dimensionalised in the form of T_4/T_2. Contrary to prior work[39], the $\frac{F}{F_{00,\mathrm{max}}}$ is not selected as an explanatory variable to estimate the GMD based on the following reasons: Firstly, the engine has to operate at a higher power than indicated by the $\frac{F}{F_{00,\mathrm{max}}}$ to produce the same F at cruise relative to ground conditions. This is because of the reduced air density where maximum thrust that can be produced at cruise is lower than the denominator, $F_{00,\mathrm{max}}$ [40], and engine-specific data on the maximum thrust at cruise is not readily available; Similarly, more work has to be done by the engine to achieve the same T_4 at cruise relative to ground conditions because the ambient temperature (and T_2) is lower than on the ground[41]. Therefore, given the small sample size for cruise BC measurements, the use of T_4/T_2 overcomes the limitations in the use of $\frac{F}{F_{00,\mathrm{max}}}$ in estimating the cruise GMD.

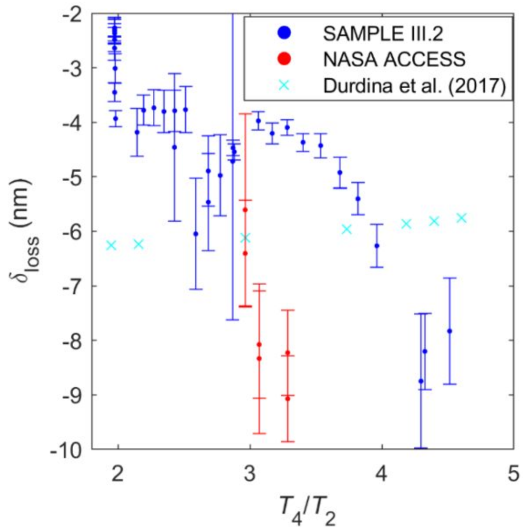

Figure S14: Quantification of δ_{loss} (estimated GMD at the engine exit plane minus the measured GMD at the instrument sampling point) vs. T_4/T_2 using data from various experimental campaigns[22,25,27].

For DAC engines (Figure S15b), we performed a linear regression on the measurements taken during the SAMPLE III.2 campaign[25] to approximate the GMD in the pilot stage as a function of T_4/T_2 (Eq. S45) while assuming an average GMD of 20 nm in the main combustion stage (Eq. S46). This is based on the rationale that T_4/T_2 can be universally used to estimate the GMD at ground and cruise conditions (as shown in Figure S15a). A step by step procedure to estimate the GMD for both SAC and DAC engines is presented as a flow chart in Figure S16.

$$\mathrm{GMD}_{\mathrm{DAC,\ pilot}}[\mathrm{nm}] = 26.33\left(\frac{T_4}{T_2}\right) - 35.98 + \delta_{\mathrm{loss}} \qquad , \frac{T_4}{T_2} < 2.85 \qquad \text{(S45)}$$

$$\mathrm{GMD}_{\mathrm{DAC,\ main}}[\mathrm{nm}] = 20 + \delta_{\mathrm{loss}} \qquad , \frac{T_4}{T_2} \geq 2.85 \qquad \text{(S46)}$$

For both SAC and DAC engines, we assume that the estimated GMD (Eq. S44 to S46) has an uncertainty of ± 20%. This uncertainty is formulated using a data comparison approach, where 95% of the experimental measurements are covered by the specified uncertainty bound (Figure S15). An alternative estimate of the uncertainty in GMD can be obtained by propagating uncertainty in $\frac{F}{F_{00,\mathrm{max}}}$, which is required to estimate T_4/T_2. If we assume a ± 10% uncertainty in $\frac{F}{F_{00,\mathrm{max}}}$ (ref.[20] and Figure S10), we estimate a ± 5.5% propagated uncertainty in GMD, which is within the ± 20% confidence interval (CI) defined empirically. In particular, we used the empirical approach ahead of error propagations because of data limitations where uncertainties introduced by the equations used to calculate the AFR and various thermodynamic quantities (P_2, T_2, T_3, P_3 and T_4, which are required to estimate the GMD) remains unquantified.

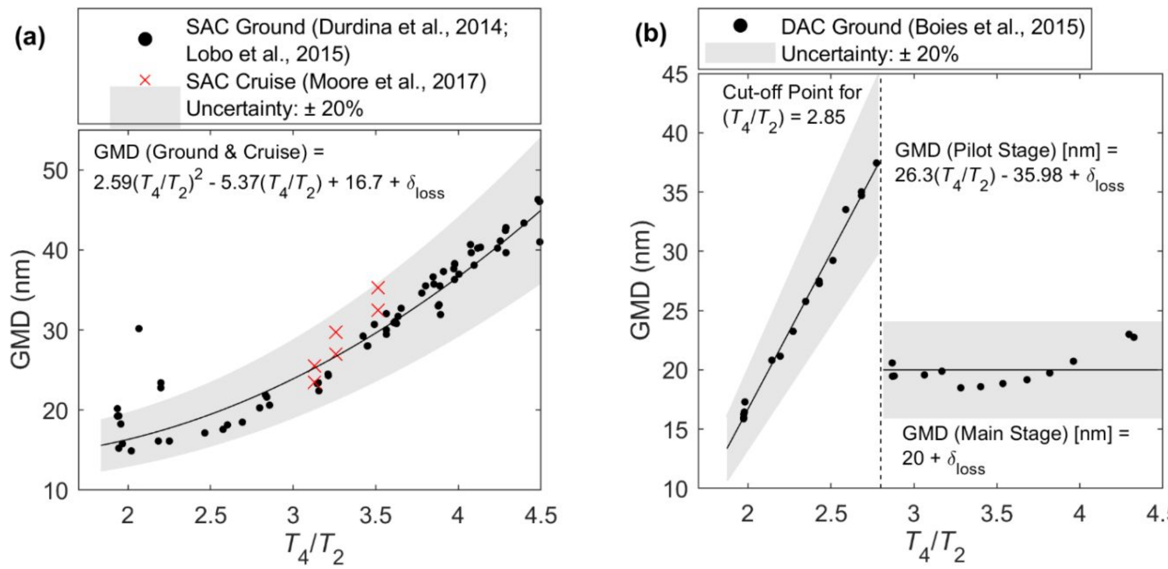

Figure S15: Predictive relations to estimate the GMD (applicable for ground and cruise conditions) as a function of T_4/T_2 for (a) SAC, and (b) DAC engines in the pilot and main combustion stage.

An alternative correlation that estimates the GMD as a function of C_{BC} is also available[28], but we have refrained from using it because of the large uncertainties in the required input parameter (C_{BC}, which have to be estimated from the FOX and/or ImFOX methods).

For both SAC and DAC engines, we assume a fixed GSD value of 1.80 to represent values at the engine exit plane[28]. This is based on several experimental observations[22,25–27] that have found that the GSD is approximately constant across $\frac{F}{F_{00,\max}}$ (and T_4/T_2).

For values of D_{fm}, ground measurements have shown that the D_{fm} for SAC engines increase and peak at around 2.8 as $\frac{F}{F_{00,\max}}$ increases[32,42], while DAC engines have a limited range of between 2.73 and 3 across different $\frac{F}{F_{00,\max}}$ [43]. Given that the T_4/T_2 at cruise and take-off conditions are within 5% [41], we therefore assume a constant D_{fm} value of 2.76 for both SAC and DAC engines at cruise conditions[3]. The BC material density (ρ_0) is assumed to be 1770 kg m^{-3}, while the prefactor and exponent coefficients of k_{TEM} and D_{TEM} have constant values of 1.621×10^{-5} and 0.39 for an aircraft gas turbine engine[3,44,45].

Finally, data from the SULFUR campaign[37,38], of which cruise measurements of EI_n and EI_m are available, are used to validate the predictive equations used to estimate the GMD (Eq. S44 to S46) and the assumed values for the GSD (1.80), D_{fm} (2.76), ρ_0 (1770 kg m^{-3}), k_{TEM} (1.621×10^{-5}) and D_{TEM} (0.39). For this validation, we assume that $\delta_{loss} = 0$, representing emissions at the instrument sampling point because the reported EI_n and EI_m were not corrected for particle line losses. The result (Figure S17) shows a good agreement between the measured and estimated EI_n (R^2 = 0.62) and the average NMB is +7.6%. While the EI_n is overestimated for older aircraft (ATTAS & B707, average NMB of +36%), it is not representative of the current fleet.

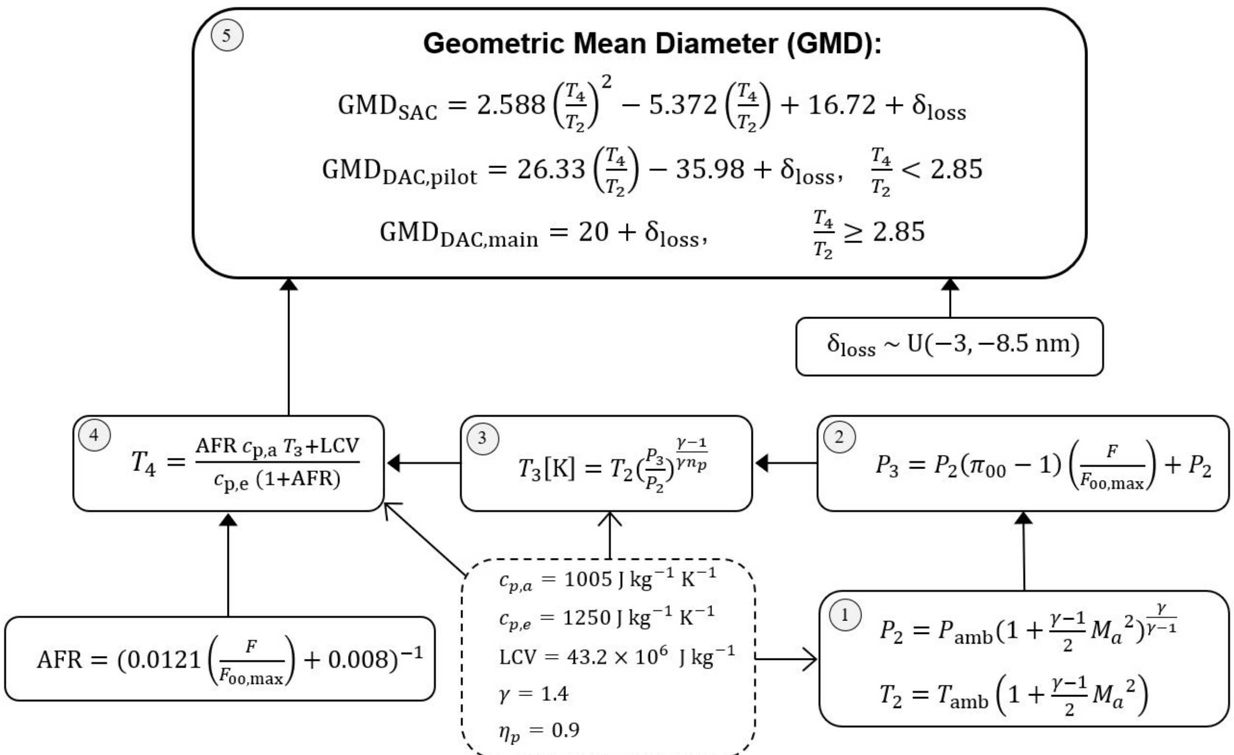

Figure S16: Flow chart on the step by step procedure to estimate the GMD for both SAC and DAC engines.

Table S4: Validation of the estimated EI_n (calculated using the FA model with predictive inputs of GMD, GSD and D_{fm}) against aircraft cruise measurements from the SULFUR experimental campaign[37,38], where measurements of EI_n, EI_m and $F/F_{00,max}$ are available.

Measured Values				Estimated Values - FA Model			
Aircraft (Engine)	**$F/F_{00,max}$**	**EI_n (kg^{-1})**	**EI_m (g kg^{-1})**	**GMD (nm)**	**GSD**	**D_{fm}**	**EI_n (kg^{-1})**
B 737-300 (CFM56-3-B1)[37]	0.23	3.50E+14	0.011	22.48	1.8	2.76	2.74E+14
A310-300 (CF6-80C2A2)[37]	0.19	6.00E+14	0.019	21.89	1.8	2.76	5.11E+14
ATTAS (M45H Mk501)[37]	0.30	1.70E+15	0.1	23.69	1.8	2.76	2.15E+15
A340-300 (CFM56-5C4)[38]	0.25	1.80E+14	0.01	25.02	1.8	2.76	1.84E+14
B707-307C, (PW JT3D-3B) [38]	0.80	1.70E+15	0.5	39.58	1.8	2.76	2.48E+15

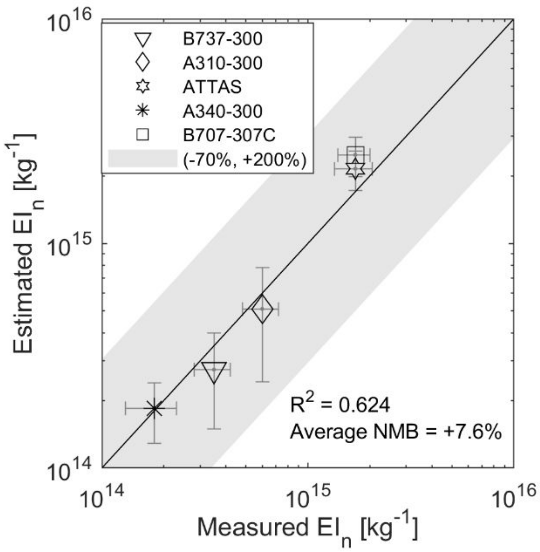

Figure S17: Validation of the FA model (using predictive inputs of GMD, and constant values of GSD, D_{fm}, ρ_0, k_{TEM} and D_{TEM}) against aircraft cruise measurements from the SULFUR experimental campaign, where the measured EI_n, EI_m and $F/F_{00,max}$ are available. Horizontal error bars denote precision errors from repeated measurements with 1σ, while vertical error bars for the estimated EI_n accounts for 1σ of the measured BC EI_m. Detailed data tables can be found in Table S4.

S3.3 User Manual for the FA Model to Estimate Aviation BC EI_n

The computational steps to implement the FA model at cruise conditions is explained in detail (below), and Figure S18 shows a flow chart containing the procedures to estimate the aircraft EI_n.

STEP 1: Estimate the aircraft engine thrust settings ($\frac{\dot{m}_f}{\dot{m}_{f,max}}$ or $\frac{F}{F_{00,max}}$) by dividing the fuel mass flow rate ($\dot{m}_f$) by the maximum fuel mass flow rate ($\dot{m}_{f,max}$), of which the $\dot{m}_f$ for each waypoint is estimated using BADA3 (as explained in §S2.3), while the $\dot{m}_{f,max}$ for each engine is available in the ICAO EDB[21]. Once $\frac{F}{F_{00,max}}$ is available, the T_4/T_2 for each waypoint is estimated according to the procedure outlined in Figure S16.

STEP 2: For SAC engines, the range of BC EI_m is estimated using both the FOX and ImFOX method. In summary, different inputs parameters are required by the FOX and ImFOX model to estimate the BC EI_m: the $\frac{F}{F_{00,max}}$, TAS, and engine pressure ratio (π_{00}, available in the ICAO EDB[21]) are required by the FOX model; and inputs of $\frac{F}{F_{00,max}}$ and the hydrogen content of fuel (H=13.8% for conventional fuel) are required by the ImFOX model. For further details, the equations and detailed description of each methodology can be found in §S3.2. For DAC engines, the BC EI_m in the pilot stage is estimated using Eq. (S42), while assuming a constant $\mathrm{EI_m}$ of 3.25 mg kg^{-1} in the lean combustion stage. The combustion stage of a DAC engine, such as the pilot and lean combustion stage, can be determined using T_4/T_2.

STEP 3: The BC GMD is also estimated using inputs of T_4/T_2: Eq. (S44) for SAC engines, and Eq. (S45) and (S46) for DAC engines. The δ_{loss} is assumed to be uniformly distributed between -3 to -8.5nm to account for particle losses in the sampling lines, which represent the characteristics of BC emitted at the engine exit plane instead of the instrument sampling point.

STEP 4: For cruise conditions, a constant BC GSD (1.8), D_{fm} (2.76), ρ_0 (1770 kg m^{-3}), k_{TEM} (1.621×10^{-5}) and D_{TEM} (0.39) are assumed for both SAC and DAC engines.

STEP 5: All input parameters required for the FA model are now available, and the BC $\mathrm{EI_n}$ can be estimated using the Eq. (1) in the main text: $\mathrm{EI_n} = \frac{\mathrm{EI_m}}{\rho_0\left(\frac{\pi}{6}\right)(k_{\mathrm{TEM}})^{(3-D_{\mathrm{fm}})}\mathrm{GMD}^{\phi}\exp\left(\frac{\phi^2 \ln(\mathrm{GSD})^2}{2}\right)}$ where $\phi = 3D_{\mathrm{TEM}} + (1 - D_{\mathrm{TEM}})D_{\mathrm{fm}}$.

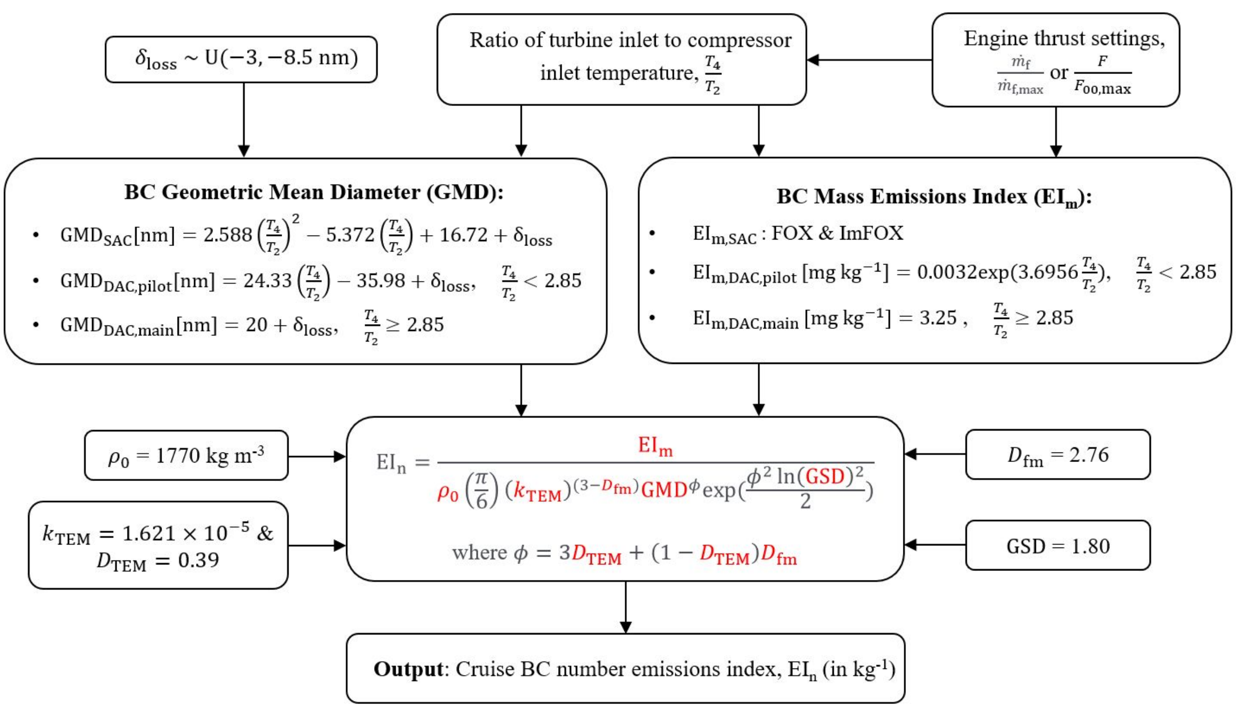

Figure S18: Flow chart outlining the step-by-step procedures to implement the FA model to estimate the aircraft $\mathrm{EI_n}$ at cruise conditions.

S3.4 Uncertainty and Sensitivity Analysis

The aircraft BC EI_n estimated from the FA Model was previously shown[3] to have an asymmetrical uncertainty bound of [-54%, +103%] with a 95% CI. This uncertainty bound assumed that the model input parameters, such as the EI_m, GMD and GSD were experimentally measured from aerosol instruments, and therefore have smaller uncertainties relative to this study where these input parameters have to be estimated (§S3.2).

To account for the larger uncertainties in the estimated input parameters used in this study, we specified an uncertainty bound of -20% and +50% for the estimated $EI_{m,SAC}$ from the FOX and ImFOX methods (Figure S12) with a uniform distribution, a ± 50% uncertainty for the estimated $EI_{m,DAC}$ for both the pilot and main combustion stage (Figure S13), a ± 20% uncertainty for the estimated GMD (Figure S15) and ± 10% for the estimated GSD with a normal distribution[22,25–27,46]. The uncertainties for the remaining parameters, such as the BC ρ_0 (± 7.8%), D_{fm} (± 7.9%), k_{TEM} (± 32.9%) and D_{TEM} (± 18.0%) were previously justified[3] and remains unchanged. We assume that uncertainties in inputs of the FA model are independent and uncorrelated, similar to the approach of Teoh et al.[3], due to the lack of measurement data in the literature to evaluate the potential for covariance between parameters.

A numerical Monte Carlo 10000-member ensemble is used to quantify uncertainty in the estimated EI_n (in line with Teoh et al.[3]) because of the non-linear properties of the FA model with higher-order components. Data from the NASA ACCESS campaign[27] is used as absolute values for the Monte Carlo simulation. As previously shown[3], the differences in uncertainty estimates between model runs typically converge to below 1% after approximately 1000 iterations. The 95% probabilistic systematic coverage interval and the associated uncertainty limits of the FA model outputs was determined using the procedure specified by Coleman & Steele[47]. The result (presented in Figure S19) shows that uncertainty bound for the estimated EI_n is lognormally distributed at [-70%, +200%] with a 95% CI. An additional analysis was conducted to assess the potential for covariance between k_{TEM} and D_{TEM}: uncertainty in the estimated aircraft BC EI_n would have minor differences under the assumption where uncertainties in k_{TEM} and D_{TEM} are correlated, reducing slightly from the original [-70%, +200%] range to [-68%, +191%]. Hence, the treatment of k_{TEM} and D_{TEM} as independent and uncorrelated, in light of data limitations, provides a slightly larger but more conservative uncertainty bound for the estimated BC EI_n.

When applied to quantify the uncertainties of BC EI_n, an uncertainty factor is generated for each flight in each Monte Carlo simulation. The nominal BC EI_n for all waypoints in a given flight is then multiplied with this uncertainty factor. This is because it is unrealistic for the estimated EI_n to vary from waypoint-to-waypoint especially when the engine is operating at a stable state. A variation in uncertainty factor between aircraft (even when they are equipped with the same engine) is more practical as it indirectly accounts for potential differences in BC emissions due to engine degradation and maintenance cycles between flights. While it is acknowledged that uncertainties in the BC EI_n could be correlated with specific engine types and operating condition, it is currently not feasible to quantify the EI_n uncertainties at such a resolution because BC emission characteristics have only been measured from a small subset of aircraft-engine combinations and predominantly on the ground. The upcoming non-volatile particulate matter (nvPM) measurement procedure[48] endorsed by the International Civil Aviation Organisation (ICAO), where measurements of the BC EI_n and EI_m are mandated for new aircraft engines developed after January 2020, may provide data to address this limitation.

Finally, we also used the Sobol' method[49] to conduct a variance-based global sensitivity analysis, and the results show that the estimated GMD contributes to the largest sensitivity to the estimated EI_n, followed by inputs of EI_m, GSD and δ_{loss}.

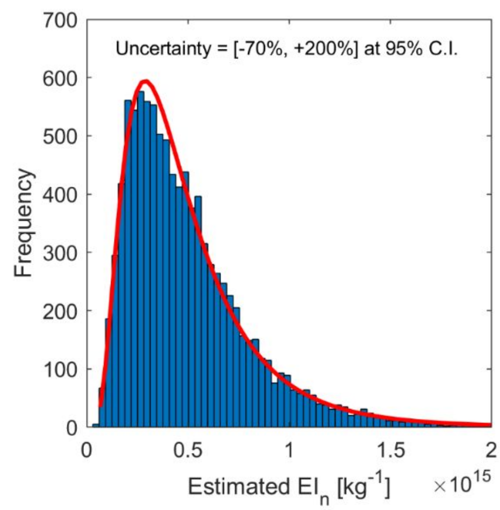

Figure S19: Uncertainty distribution of the FA model outputs (the estimated EI_n for aircraft emissions) when predictive inputs of BC EI_m, GMD, GSD, D_{fm}, k_{TEM} and D_{TEM} are used. The histogram outputs are best fitted with a lognormal distribution (red line).

S3.5 Aircraft Black Carbon Particle Number Emissions from Individual Flights

Figure S20 shows the change in the estimated EI_n for two aircraft trajectories. For the Boeing-737 aircraft powered by SAC engines (Figure S20a), the nominal EI_n ranges from 1.05 to 1.91 $\times 10^{15}$ kg^{-1} in the climb and cruise phase. During the descent phase, EI_n increases from around 0.81 to 2.11 $\times 10^{15}$ kg^{-1}. The higher EI_n in the descent phase is generally due to the decrease in BC GMD as engine power is reduced. Although the estimated BC EI_m (proportional to the estimated EI_n) is also decreasing, the sensitivity analysis (discussed in SI §S3.4) describes how the FA model is most sensitive to the GMD (to which EI_n is inversely proportional). The estimated EI_n for this particular flight is around a factor of 2 higher than the cruise EI_n measurements collected from the NASA ACCESS[27], SULFUR and POLINAT[37,38,50] campaigns because the in-situ measurements were not corrected for particle line losses, which thereby represent values at the instrument sampling point rather than the engine exit plane.

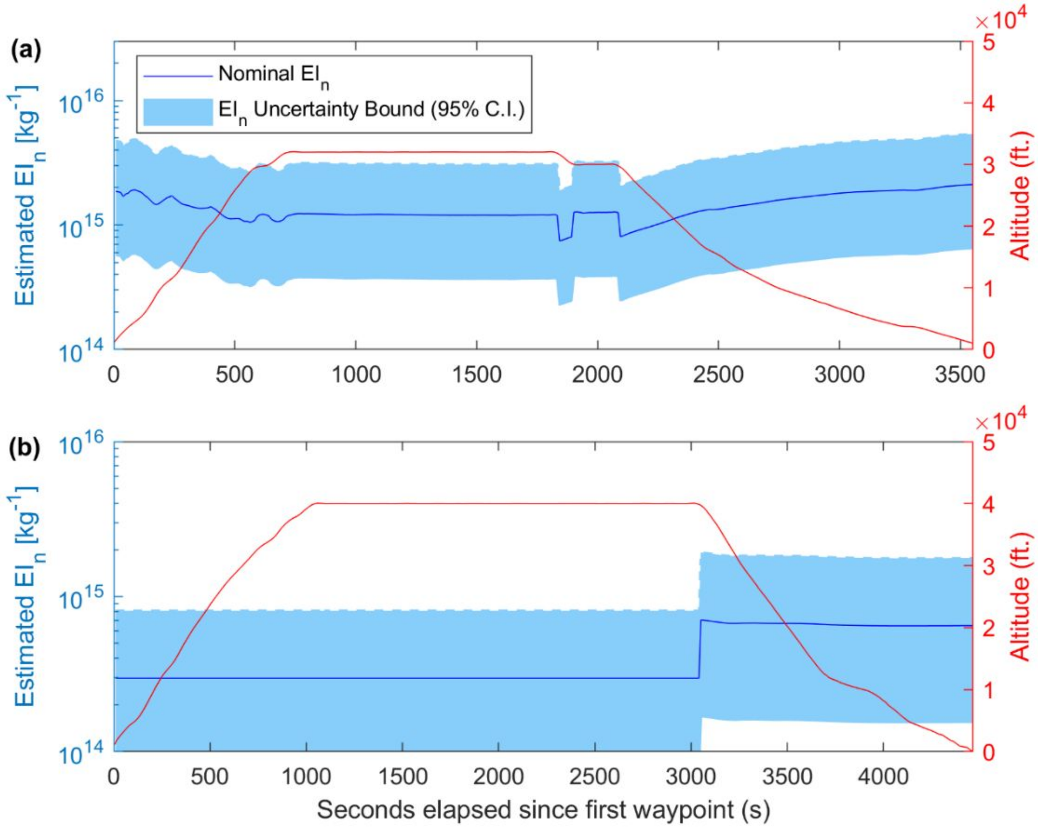

Figure S20: Changes in the estimated EI_n across different phases of flight. For the aircraft in case: (a), the B737-800 (FLT0413, 7th May 2012) was equipped with SAC engines (CFM56-7B26); while (b) the B777-200LR (FLT0257, 7th May 2012) was powered by DAC engines (GE90-90B).

For the Boeing-777 aircraft equipped with DAC engines (Figure S20b), the nominal EI_n in the climb and cruise phase is 76.9% lower than the SAC aircraft, with a constant value of 0.30×10^{15} kg^{-1} because the engines are operating in the lean combustion mode. However, during the descent phase, the DAC engines are operating in the pilot stage and as a result, the nominal EI_n increases by 123% to around 0.65 and 0.71×10^{15} kg^{-1}. The difference in EI_n between a SAC and DAC engine lead to significant implications to the contrail characteristics and climate forcing.

On the whole, the estimated EI_n for the fleet (1.37 [1.35, 1.39] $\times 10^{15}$ kg^{-1}) supports the assumption of previous contrail studies to increase their EI_n from 0.3 to 1 $\times 10^{15}$ kg^{-1} when comparing between simulated and observed contrail properties[4,5,51–54]. In particular, the ice particle numbers measured in young contrails of various airliners at cruise, and the lifetime of contrail cirrus as observed by satellite data could only be explained with models using EI_n estimates of 10^{15} kg^{-1}.

S4 CoCiP Contrail Model and Meteorology

S4.1 CoCiP Model Description

CoCiP is a Lagrangian model used to simulate the life cycle of individual contrail segments from their formation behind an aircraft to dissipation. To estimate the characteristics of contrails (such as the dimensions, ice particle mean radius, τ and lifetime) that are formed along the flight routes, CoCiP calls for inputs of air traffic data (CARATS Open Data), BC PN emissions (FA model) and meteorology. For the latter, we use the ECMWF's ERA5 ten-member ensemble (EDA) and the high resolution realisation (HRES)[13]. Further details on meteorology is discussed in §S4.2.

For this study, the model structure and modifications made in CoCiP are summarised: Firstly, the Schmidt-Appleman criterion[55] is used to determine if a contrail is formed in a given waypoint. The flight segment between two consecutive points forming contrails is a contrail segment. If a contrail is formed in such a segment, CoCiP assumes that the initial number of contrail ice particle is equal to the aircraft BC EI_n, where EI_n is identified as a critical input parameter[4]. While previous applications of CoCiP adopted a constant EI_n of in between 0.24×10^{14} and 10^{15} kg^{-1} for all aircraft types and operating conditions, the FA model now provides an advantage as it enables the EI_n to be estimated for each waypoint as a function of aircraft type and engine thrust settings. A parametric model is then used to simulate the wake vortex phase where the initial contrail properties are calculated after accounting for ice particle number losses due to adiabatic heating and atmospheric mixing. Next, the spatial and temporal evolution of surviving contrail segments are modelled using a Gaussian plume model and integrated using a second-order Runge-Kutta scheme over a sequence of time steps ($\Delta t = 0.5$ h) until its end of life, defined when the: (i) contrail-segment age exceeds 24 h, (ii) the contrail-segment ice particle number per m^3 of air, $\mathrm{Z_{ice}} < 10^3$ m^{-3} , or (iii) $\tau < 10^{-6}$. Finally, the simulated contrail characteristics, as well as the radiation data provided by the ECMWF ERA5 datasets are subsequently used as inputs to a parametric radiative forcing (RF) model[56] to estimate the climate forcing of contrails in the form of local RF (RF', defined as the change in energy flux per contrail area) and energy forcing (EF). The EF per unit contrail length is the time integral of local contrail RF times the contrail width over its lifetime, divided by the initial contrail length. For further details on the model structure, equations and assumptions used in CoCiP, the reader is referred to the literature[4,56].

To reduce the complexity and computational requirements, CoCiP was run in an offline mode with no interaction between atmospheric humidity and contrails, and without the effects of ambient ice nuclei entrainment. The absence of these features does not significantly change the characteristics and climate forcing of contrails: When CoCiP was coupled to a global circulation climate model, the characteristics and climate forcing of contrails changes by around [-30%, +5%] relative to the offline scenario[52]; and the annual mean BC PN concentrations emitted by aircraft in a high density airspace (≈10^6 m^{-3}) [57] is three orders of magnitude greater than the background ice nuclei (≈10^3 m^{-3}, which was assumed by the CERM model[58]). Nevertheless, previous studies which run CoCiP in an offline mode have also validated the modelled contrail properties with in-situ measurements and satellite observations, and the results showed good agreements[4,5,51,53,54,59].

S4.2 Meteorology

The characteristics and climate forcing of contrails are influenced by different meteorological and radiation parameters: T_{amb} and specific humidity (q) affects the contrail formation and persistence; horizontal wind components (U & V), their shear values and vertical velocity (ω) impact the spreading of contrails; and cloud cover and specific ice water content (cloud ice mass per unit volume of air, IWC) affects the optical depth of NWP cirrus (τ_{c}), which, together with the solar direct radiation (SDR), reflected solar radiation (RSR) and outgoing longwave radiation (OLR), affects the contrail radiative forcing.

The ECMWF is cited to be the world-leading weather forecast centre which provides high-quality NWP predictions and reanalysis datasets[60,61], and the ERA5 is a reanalysis dataset that combines historical observational data with models to provide a 4D numerical description of the recent climate. It is the ECMWF's fifth-generation reanalysis data and a successor to the ERA5-Interim reanalysis[62], and contains many improvements such as the incorporation of more extensive observational inputs to the data assimilation system, a higher spatiotemporal resolution and the revaluation of finer meteorological structures in the atmosphere[63]. There are two distinct product types in the ERA5[13]: The HRES contains nominal climate data at a very high spatial (0.25° × 0.25°) and temporal resolution (hourly), while the EDA provides 10-member ensemble means and standard deviations to account for observational, model and boundary condition uncertainties in the reanalysis but at a lower spatial (0.5° × 0.5°) and temporal resolution (3-hourly). The respective characteristics and a comparison between the ERA5 EDA and HRES meteorological dataset is presented in Table S5.

Table S5: Comparison between the ERA5 Ten-Member Ensemble (EDA) and the High-Resolution Realisation (HRES) meteorological dataset from the ECMWF.

	ERA5 EDA	**ERA5 HRES**
Horizontal Grid Resolution	0.5° × 0.5°	0.25° × 0.25°
Vertical Resolution	37 levels up to 1hPa	37 levels up to 1hPa
Temporal Resolution	3-hourly	Hourly
Nominal Values	10-Member Ensemble Mean	Single-Run Realisation
Standard Deviation	✓	X
File Size per day	≈ 1.5 GB	≈ 10 GB
Variables Downloaded	- Specific cloud ice water content - Specific Humidity - Temperature - U-component of wind - V-component of wind	- Vertical Velocity - Geopotential - TOA incident solar radiation - Top net solar radiation - Top net thermal radiation

In this study, we selected both the ECMWF's ERA5 HRES and EDA reanalysis because they are publicly available and contain all the necessary meteorological and radiation data for contrail analysis. Eq. (S47) is used to calculate the relative humidity with respect to ice (RHi),

$$\mathrm{RHi} = \frac{q \times p_w \times \mathrm{R}_1}{p_{\mathrm{ice}}(T_{\mathrm{amb}}) \times \mathrm{R}_0}, \tag{S47}$$

where p_w is the pressure altitude for each waypoint (in units of Pa), R_1 (461.51 J kg^{-1} K^{-1}) and R_0 (287.05 J kg^{-1} K^{-1}) are the real gas constant for water vapour and air respectively, and p_{ice} is the saturation pressure over ice water surfaces[64],

$$p_{\mathrm{ice}}[\mathrm{Pa}] = 100\exp\left[\frac{-6024.5282}{T_{\mathrm{amb}}} + 24.721994 + 0.010613868 T_{\mathrm{amb}} - 1.3198825\times 10^{-5} T_{\mathrm{amb}}^{2} - 0.49382577\ln(T_{\mathrm{amb}})\right]. \tag{S48}$$

We note that the specific humidity (and the RHi) in both the ERA5 EDA and HRES datasets are enhanced in CoCiP by dividing it with RHi_c (= 0.9), in line with previous studies[4,52,65]. This is due to the sub-grid scale variability that cannot be resolved from the resolution of existing meteorological datasets that are available, where a grid cell could be locally supersaturated even though it is sub-saturated on average. For further reasons and details on the enhancement of the specific humidity by CoCiP, the reader is referred to §S4.3.

Due to differences in the data assimilation procedures, we highlight minor differences between the radiation parameters, such as the incident solar radiation at the top of atmosphere (TISR, units of J m^{-2}), top net solar radiation (TSR, units of J m^{-2}) and the top net thermal radiation (TTR, units of J m^{-2}) that are provided by the ERA5 EDA and HRES: The radiation parameters provided by the ERA5 EDA are accumulated values between corresponding time steps, while the ERA5 HRES provides cumulative values from the first time step[66]. To calculate the mean flux in a given time interval (in units of W m^{-2}), the accumulated values are divided by the time period over which the data has been accumulated[66]. To account for these differences, Eq. (S49) to Eq. (S51) are used to calculate the SDR, RSR and OLR for the ERA5 EDA,

$$\mathrm{SDR_{EDA}}\,[\mathrm{W\,m^{-2}}] = \frac{\mathrm{TISR}(t)}{(3\times 3600)}, \tag{S49}$$

$$\mathrm{RSR_{EDA}}\,[\mathrm{W\,m^{-2}}] = \frac{\mathrm{TISR}(t) - \mathrm{TSR}(t)}{(3\times 3600)}, \tag{S50}$$

$$\mathrm{OLR_{EDA}}\,[\mathrm{W\,m^{-2}}] = \frac{\mathrm{TTR}(t)}{(3\times 3600)}, \tag{S51}$$

while Eq. (S52) to Eq. (S54) are used for the ERA5 HRES:

$$\mathrm{SDR_{HRES}}\,[\mathrm{W\,m^{-2}}] = \frac{\mathrm{TISR}(t) - \mathrm{TISR}(t-1)}{3600}, \tag{S52}$$

$$\mathrm{RSR_{HRES}}\,[\mathrm{W\,m^{-2}}] = \frac{[\mathrm{TISR}(t) - \mathrm{TSR}(t)] - [\mathrm{TISR}(t-1) - \mathrm{TSR}(t-1)]}{3600}, \tag{S53}$$

$$\mathrm{OLR}_{\mathrm{HRES}}\,[\mathrm{W\,m^{-2}}] = \frac{\mathrm{TTR}(t) - \mathrm{TTR}(t-1)}{3600}. \tag{S54}$$

Given that the ERA5 EDA provides the ensemble standard deviation (67% CI) for each data point (example in Figure S21), we multiply these figures by 1.96 to account for the uncertainties arising from meteorology to approximate the 95% CI of the characteristics and climate forcing of contrails. The range of contrail outputs estimated using the ERA5 EDA is then compared with the results from a nominal run of CoCiP using the higher-resolution ERA5 HRES to identify any possible discrepancies. Further details on the uncertainty analysis is discussed in §S4.4.

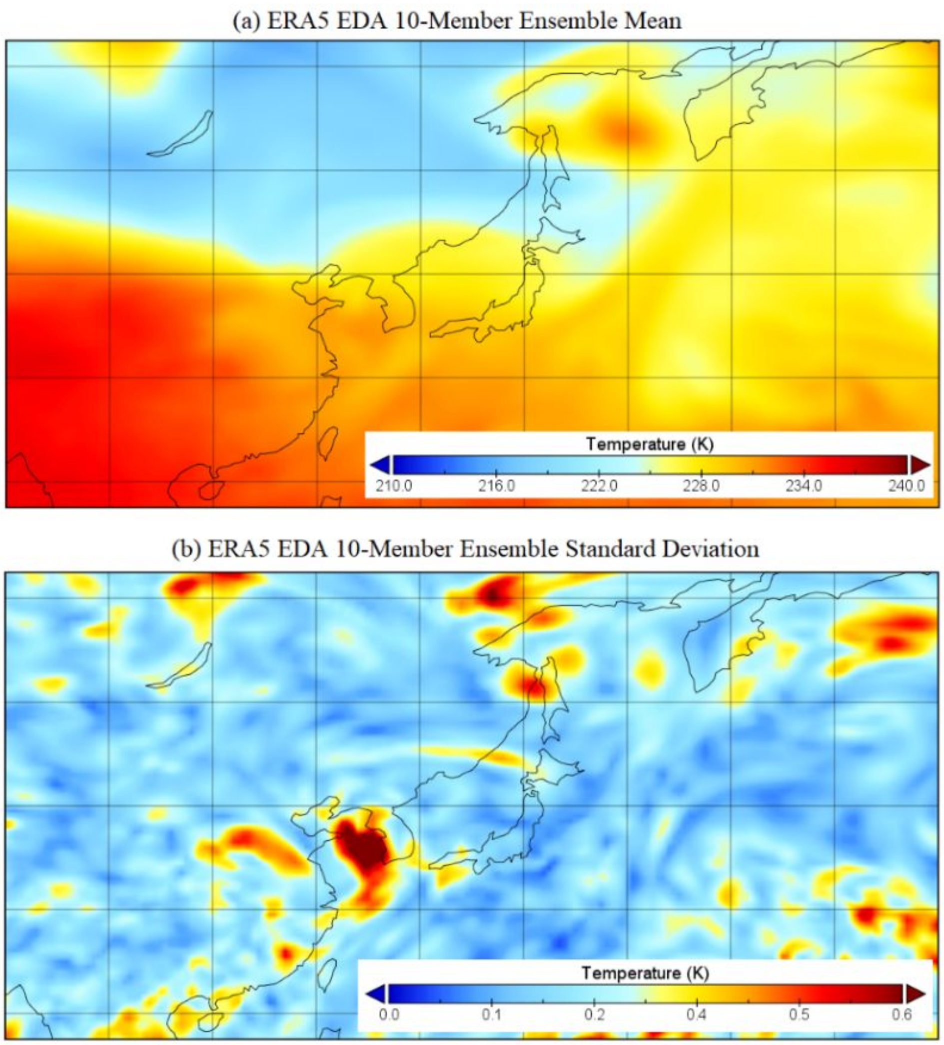

Figure S21: Example of the meteorological data provided by the ERA5 EDA's 10-Member Ensemble (a) Mean, and (b) Standard Deviation at FL360 (36,000 feet) at 00:00 UTC, 7th of September 2012.

S4.3 Validation of the ERA5 EDA Dataset

The ERA5 EDA dataset has also been validated with meteorological data provided by the In-Service Aircraft for a Global Observing System (IAGOS) Measurement of Ozone and Water Vapour by Airbus in-service aircraft (MOZAIC) campaign, a European Research Infrastructure for global observations of atmospheric composition measured from commercial aircraft. The ambient temperature, wind and specific humidity obtained from the MOZAIC campaign were measured in-situ by 28 distinct flights and 42,713 waypoints (trajectories shown in Figure S22). These flights provided by the MOZAIC dataset are flown over the Japanese airspace and within the time period covered by the CARATS Open Data. The RHi is estimated from q using Eq. (S47).

The validation results (presented in Figure S23) show that the ambient temperature and wind (U and V components) between the ERA5 EDA and MOZAIC datasets are in good agreement: The R^2 values range from 0.947 to 0.995, and their respective magnitude and distribution (as shown in the histograms) are generally consistent. However, a comparison of the RHi values showed a lower correlation (R^2 = 0.434). The histogram (Figure S23d) also shows that the RHi from the ERA5 EDA peaks at just slightly above 100%, while a right tail (with higher RHi values of between 120% to 150%) is observed for the MOZAIC dataset.

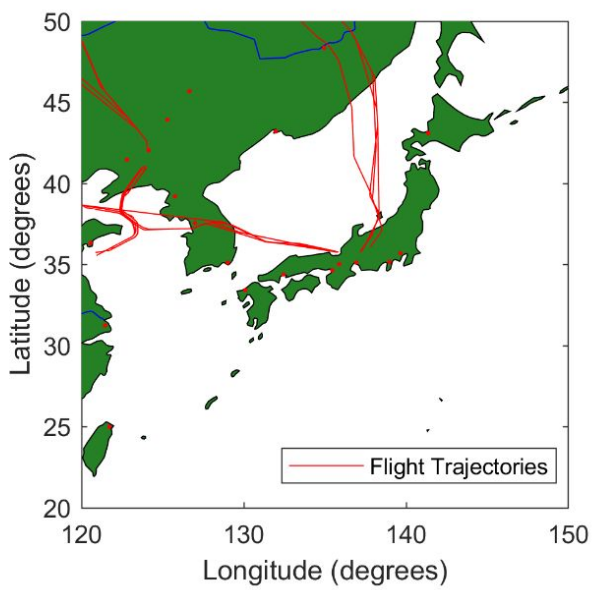

Figure S22: Trajectories of the 28 flights provided by the IAGOS MOZAIC campaign, where in-situ measurements of the ambient temperature, wind and specific humidity were performed.

According to the literature[65,67], the higher RHi values (120% to 150%) from in-situ measurements (MOZAIC) represent in-cloud supersaturation. They are realistic and occur in the atmosphere both in clear and cloudy air with low concentrations of ambient ice particles. However, the ECMWF models (such as the ERA5 EDA and HRES) rarely predict high supersaturations because it uses an approximated method to compute ice supersaturation: Ice in a cloud free grid cell is formed only when the relative humidity reaches the limit for homogeneous ice nucleation. The ECMWF models then adopts a simplified assumption on the relaxation time, defined as the time taken for the ambient supersaturation to dissipate and reach equilibrium at RHi ≈ 100%[68], where all supersaturated humidity are converted into ice and the RHi returns to ice saturation (100%) within one time step[67,69]. In reality, the relaxation time depends on the product of number and size of ambient ice crystals and the deposition of ambient water vapour on the ice crystals: A higher number of ambient ice crystals or a larger size increases the consumption rate of excess water vapour, thereby reducing the relaxation time[70]. Given the adoption of simplified assumptions, the ERA5 EDA shows an RHi distribution with rare occurrences of high ice supersaturations, and in many cases, the ice supersaturation is just above or close to 100%. Therefore, in addition to the reason highlighted in §S4.2, CoCiP tries to correct for this approximate form of ice supersaturation by enhancing the specific humidity (from the ERA5 EDA and HRES) by dividing it with RHi_c (= 0.9) as a workaround, and this approach also accounts for the sub-grid scale variability that cannot be resolved from the resolution of existing ECMWF models.

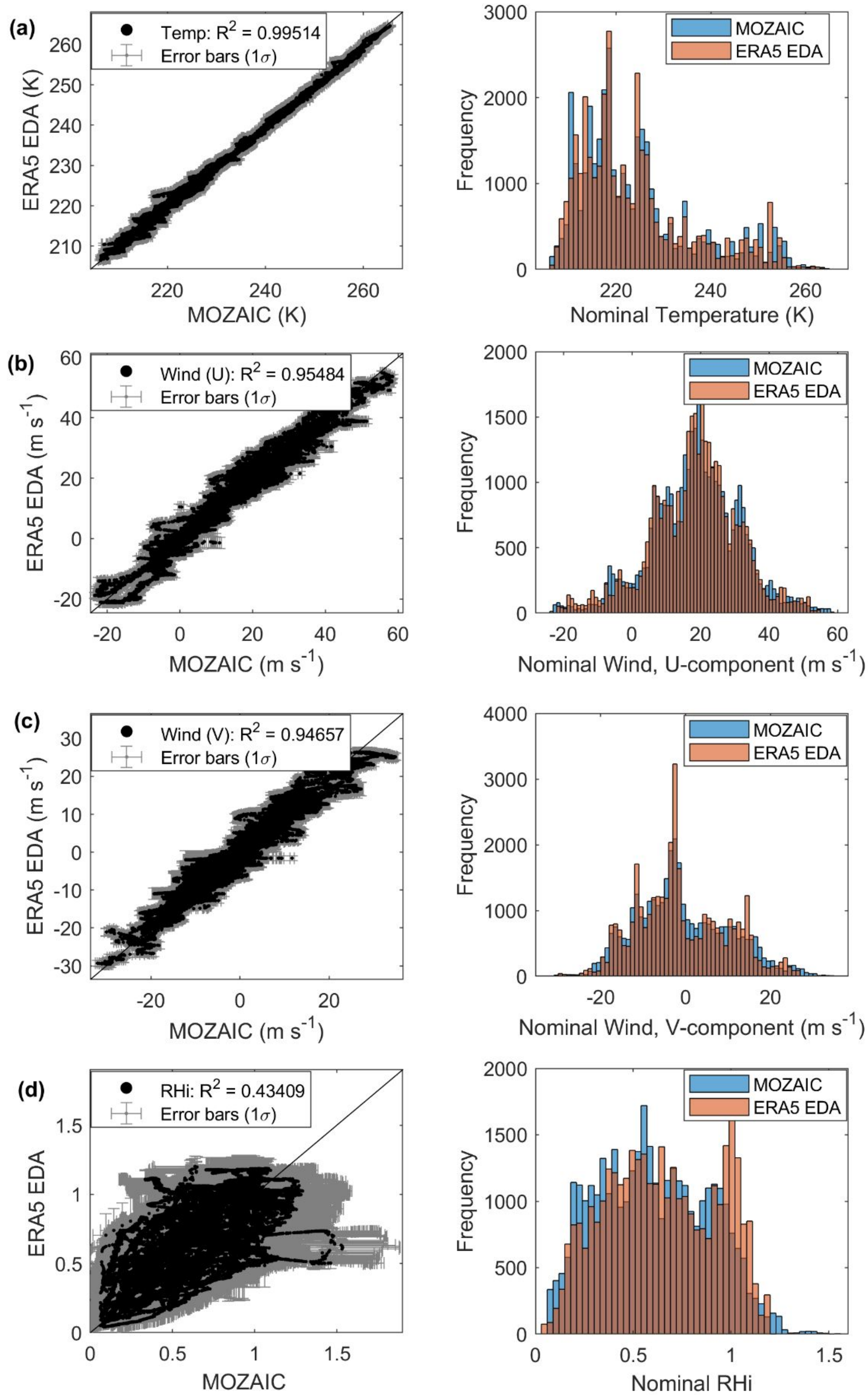

Figure S23: Validation of the ERA5 EDA meteorological dataset against in-situ measurements of the ambient temperature, wind (U & V component) and RHi provided by the IAGOS MOZAIC experimental campaign.

S4.4 Uncertainty Analysis

We implemented CoCiP with a Monte Carlo simulation and assumed that the meteorological uncertainties provided in the ERA5 EDA follow a Gaussian distribution[71]. For each Monte Carlo simulation and time slice, a random uncertainty factor is generated for the required meteorological and radiation parameters from the ERA5 EDA. Hence, this approach assume that the uncertainties are correlated spatially.

While we acknowledge the presence of uncertainties in the RHi_c, this parameter is kept constant at 0.9 because of the limitations in existing datasets where the uncertainty range and distribution cannot be quantified. We attempted a workaround to circumvent the use of RHi_c by using the in-situ RHi measurements provided by the MOZAIC dataset to correct for the RHi provided by the ERA5 datasets, but concluded that a complete assessment is not possible because: (i) in-situ measurements of the RHi were only collected from 28 distinct flights with a limited coverage within the domain of the CARATS Open Data; which leads to (ii) an incomplete dataset to fully capture the spatial distribution and the day-to-day variation of the RHi over Japan; and (iii) uncertainties in the ambient H_2O measurements (which is used to compute the RHi). A second attempt was also made by specifying an arbitrary uncertainty range for the RHi_c in the Monte Carlo simulation: Given that the uncertainties in the RHi_c is not expected to vary temporally, it is more logical to vary the RHi_c between Monte Carlo simulations rather than each time step. However, this approach leads to unrealistic scenarios where one Monte Carlo simulation generates a lot of contrails (RHi_c = 0.85) and another where negligible contrails are produced (RHi_c = 0.95) throughout the six weeks of data. Additionally, the uncertainties introduced by the RHi_c would overshadow all other uncertainties arising from the BC PN emissions and meteorology. Based on these limitations, we therefore refrained from including RHi_c in the uncertainty analysis, and instead stick with the methodology of previous studies[4,52,65] by enhancing the specific humidity (provided by the ERA5 datasets) by dividing it with a constant RHi_c (=0.9).

Uncertainties in aircraft BC PN emissions (previously described in §S3.4) are also propagated to quantify the range of contrail characteristics and climate forcing. The input variables (and their respective uncertainty distribution) that are propagated to the modelled contrail outputs are summarised in Figure S24 and Table S6.

We note that the randomised uncertainty factor applied to each variable and Monte Carlo simulation is also saved as a matrix to ensure that the model outputs are reproducible, of which uncertainties in the aircraft EI_n and meteorology are consistent between the: (i) baseline scenario where contrails forming from original trajectories are modelled (further details in the main text and §S5); and (ii) diversion cases where a selected number of aircraft with the largest contrail EF are diverted by ±2000 feet to minimise the climate forcing of contrails (further description in §S6.1).

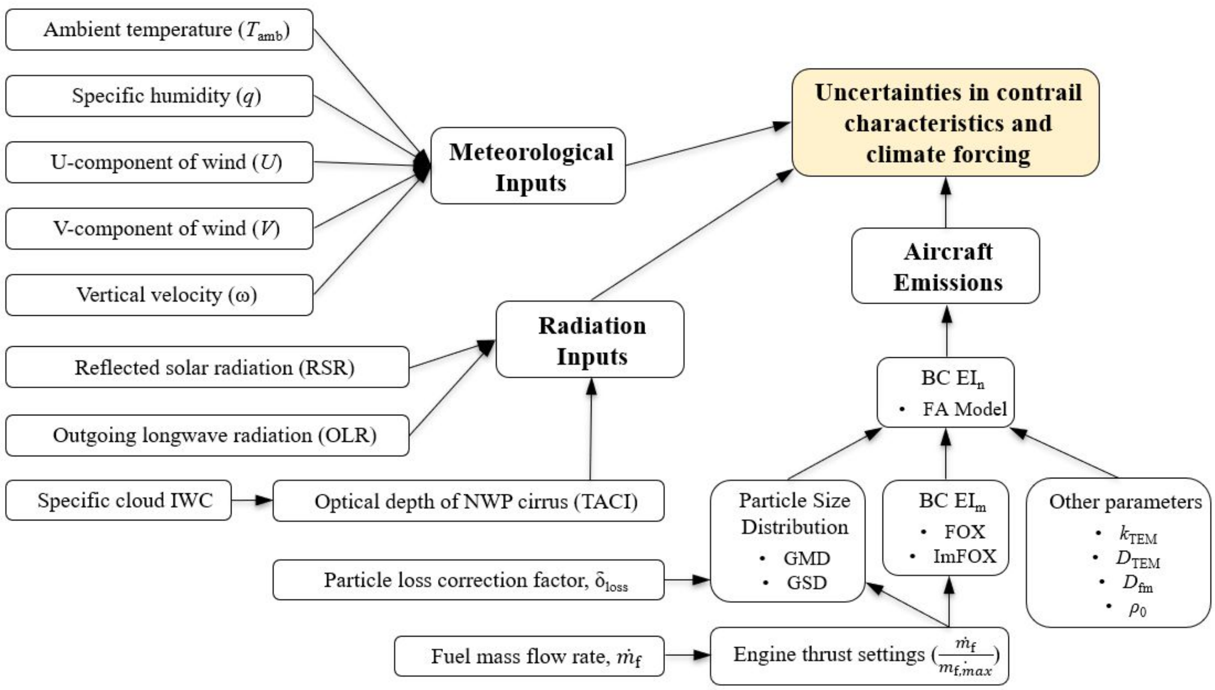

Figure S24: Flow chart of input variables which uncertainties are propagated to the modelled contrail outputs.

Given the computational demands where one CoCiP run for the full six weeks of aircraft movements data over Japan takes approximately 5 h, we have restricted the number of Monte Carlo simulation to 100. To overcome this limitation and ensure a rapid rate of convergence, the stochastic factors applied to model the uncertainties in aircraft PN emissions and meteorology are generated using the Sobol sequence[49], a quasi-random low-discrepancy sequence, and then scrambled using the Matousek-Affine-Owen algorithm[72]. When compared with purely random numbers, the quasi-random numbers (Sobol Sequence) are able to cover the domain of interest more rapidly and evenly, which increases the rate of convergence. Using this approach, the results have shown that the fleet-averaged contrail outputs converges to within 0.1% after 100 runs

(Figure S25), while outputs from individual flights (with larger uncertainties) converge to within 1% (Figure S26). For individual flights, the uncertainty bound in the BC EI_n, contrail characteristics and climate forcing are approximately one to two orders of magnitude larger relative to the fleet-average because uncertainties arising from individual flights cancel out when aggregated over the entire fleet.

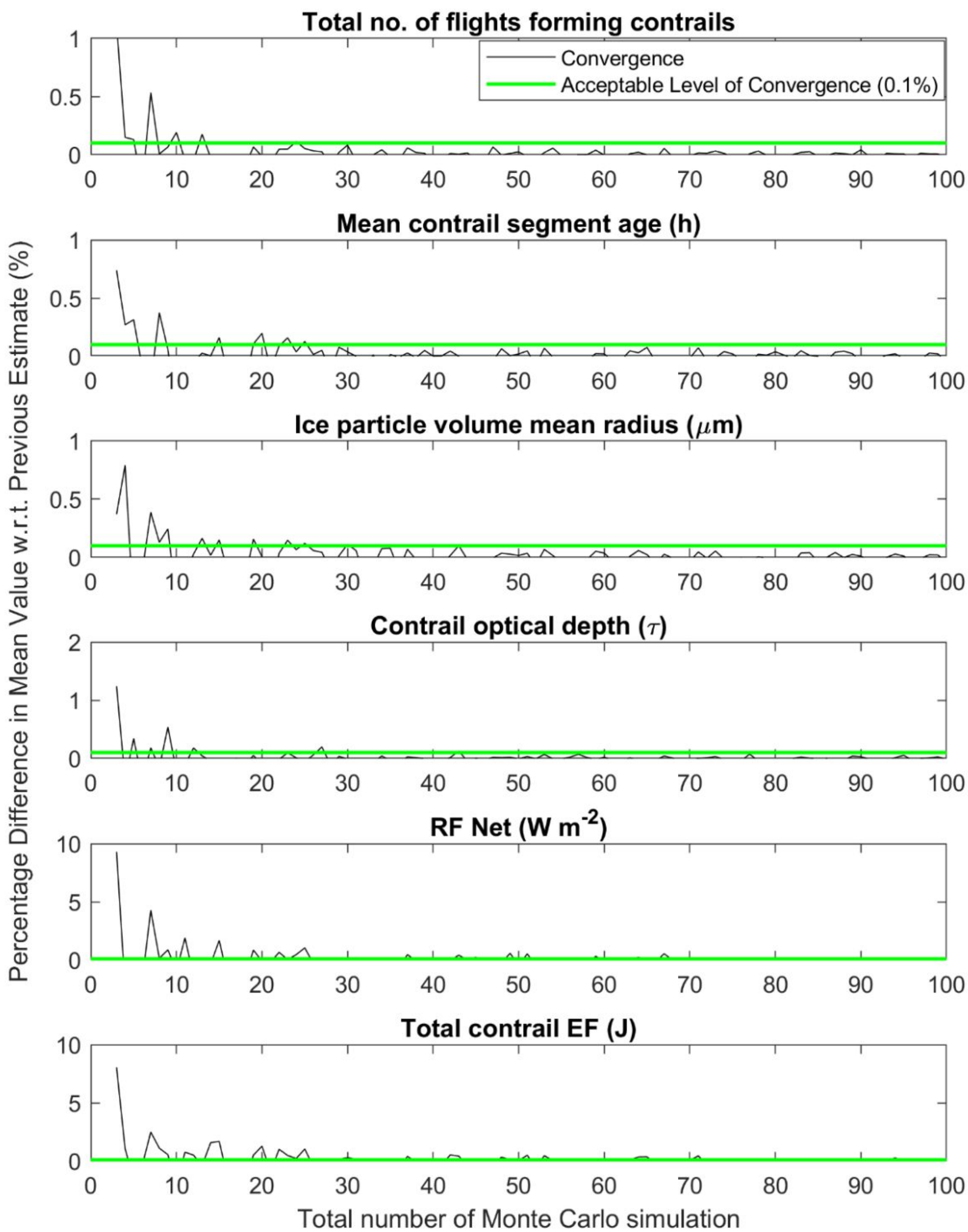

Figure S25: Convergence of the fleet-averaged contrail outputs, such as the (i) total number of flights forming contrails, (ii) mean contrail segment age, (iii) ice particle volume mean radius, (iv) optical depth, (v) net RF and (vi) contrail EF, relative to the number of Monte Carlo simulation. After 100 runs, the percentage difference in mean values with respect to previous estimates are typically below 0.1%.

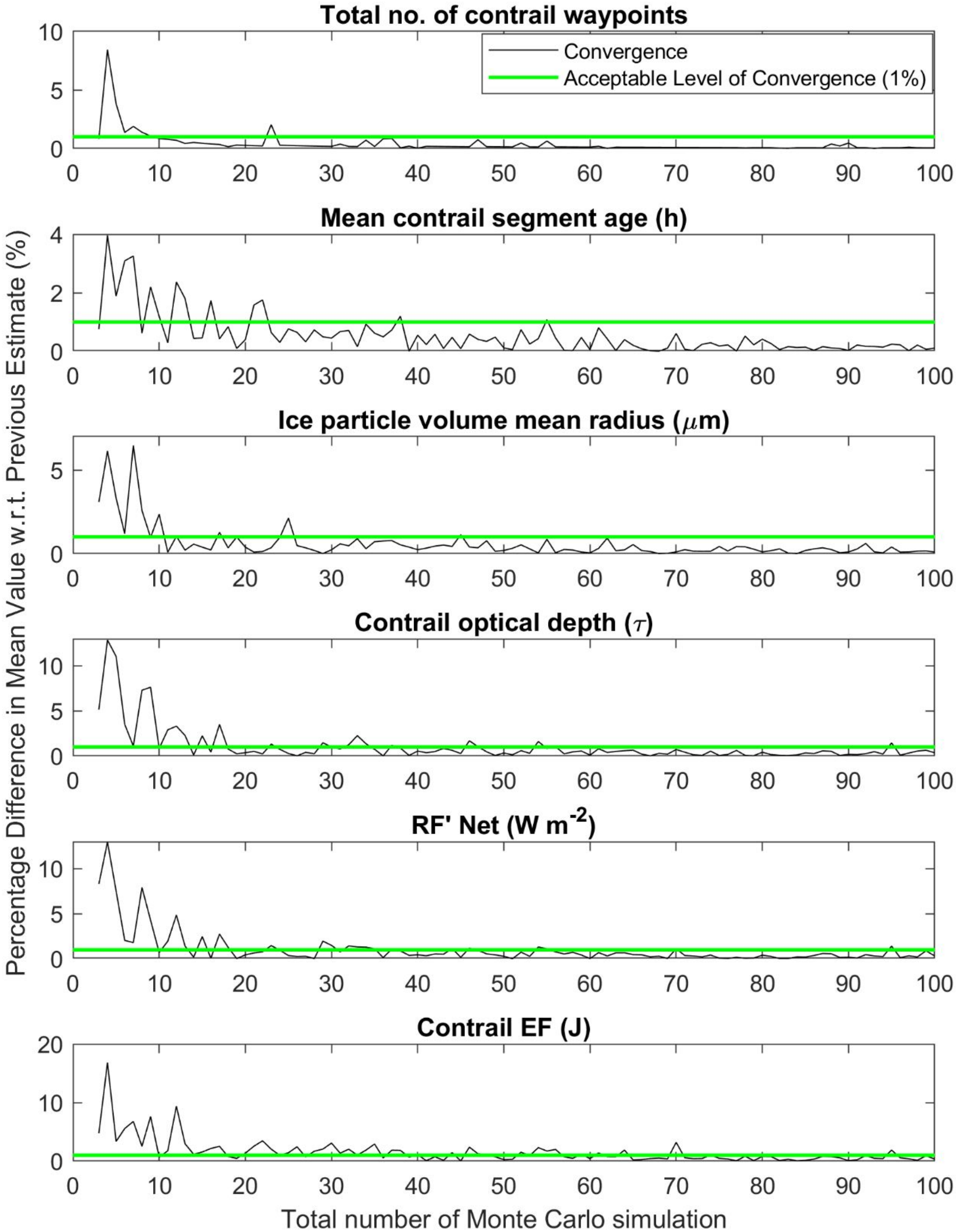

Figure S26: Convergence of the contrail outputs produced by an individual flight (an Airbus A330-300 flight on the 6th of September 2012) relative to the number of Monte Carlo simulations. After 100 runs, the percentage difference in mean values with respect to previous estimates for the (i) total number of contrail waypoints, (ii) mean contrail segment age, (iii) ice particle mean radius, (iv) optical depth, (v) net RF, and (vi) contrail EF converges to below 1%.

Table S6: Summary of the uncertainties and distribution for each input variable, which uncertainties are propagated forward to the modelled contrail outputs.

Input Variables	Units	Uncertainty Distribution	Notes
Aircraft Emissions			
BC EI_n	kg^{-1}	Lognormal	[-70%, +200%] (§S3.4)
- BC EI_m (SAC)	$mg\ kg^{-1}$	Uniform	[-20%, +50%] of FOX & ImFOX outputs (Fig S12)
- BC EI_m (DAC)	$mg\ kg^{-1}$	Uniform	± 50% for both pilot & main stage (Fig S13)
- GMD	nm	Normal	± 20% (Fig S15)
- GSD	-	Normal	± 10% [3]
- k_{TEM}	-	Normal	± 32.9% [45]
- D_{TEM}	-	Normal	± 18.0% [45]
- D_{fm}	-	Normal	± 7.9% [73]
- BC ρ_0	$kg\ m^{-3}$	Normal	± 7.8% [44]
- δ_{loss}	nm	Uniform	[-8.5nm, -3nm] (Fig S14)
- $\dot{m}_f$	$kg\ s^{-1}$	Normal	Uncertainties from T_{amb} & winds (ERA5 EDA)
Meteorological Inputs			
Ambient temperature (T_{amb})	K	Normal	
Specific humidity (q)	$kg\ kg^{-1}$	Normal	
U-component of wind (U)	$m\ s^{-1}$	Normal	10-member ensemble means and standard deviations provided by ECMWF's ERA5 EDA
V-component of wind (V)	$m\ s^{-1}$	Normal	
Vertical velocity (ω)	$Pa\ s^{-1}$	Normal	
Specific cloud IWC	$kg\ kg^{-1}$	Normal	
Radiation Inputs			
Reflected solar radiation (RSR)	$W\ m^{-2}$	Normal	10-member ensemble means and standard deviations provided by ECMWF's ERA5 EDA
Outgoing longwave radiation (OLR)	$W\ m^{-2}$	Normal	

S4.5 CoCiP Programming Language & Modifications

While CoCiP was originally developed and coded using the Fortran programming language[4], we have translated the CoCiP codes from Fortran to MATLAB. This recoding provides several clear advantages such as the improved user interface for debugging purposes, as well as the revision of the code structure and logic to improve the computational efficiency of CoCiP.

For the purpose of this study, several minor modifications have also been made to CoCiP: Firstly, a Monte Carlo loop was added to model the uncertainties of contrails from individual flights, where further information was presented in the SI4.4. Given the high temporal resolution of the CARATS Open Data (where the aircraft positional data is recorded every 10s), the computational time required for CoCiP to complete one Monte Carlo simulation through the six weeks of aircraft activity data is approximately 5 h, or 500 h (20.8 days) of computational time if the number of Monte Carlo simulation is specified to 100. To reduce this computational time, the structure and logic of CoCiP is modified, enabling it to break the overall task into smaller pieces for parallel computing. When the codes are run in an Intel Xeon Processor E5-2640 v4 (10 cores and a processor base frequency of 2.40 GHz) and 64 GB of RAM, we are able to reduce the computational time to approximately 48 h (2 days).

S5 Baseline Contrail Modelling Results (Fleet & Individual Flight)

The characteristics and climate forcing of contrails is modelled for individual flights and then aggregated to obtain average values for the entire fleet (six weeks of aircraft activity provided by the CARATS Open Dataset). The contrail outputs provided by CoCiP are visualised: Figure S27 provides a 3D visualisation of the aircraft flight trajectories together with the location of individual waypoints forming contrails. We note that the CoCiP simulated contrail properties has previously been validated[5,52,74–76] against various satellite observations, in-situ measurements and estimates from large eddy simulations (LES).

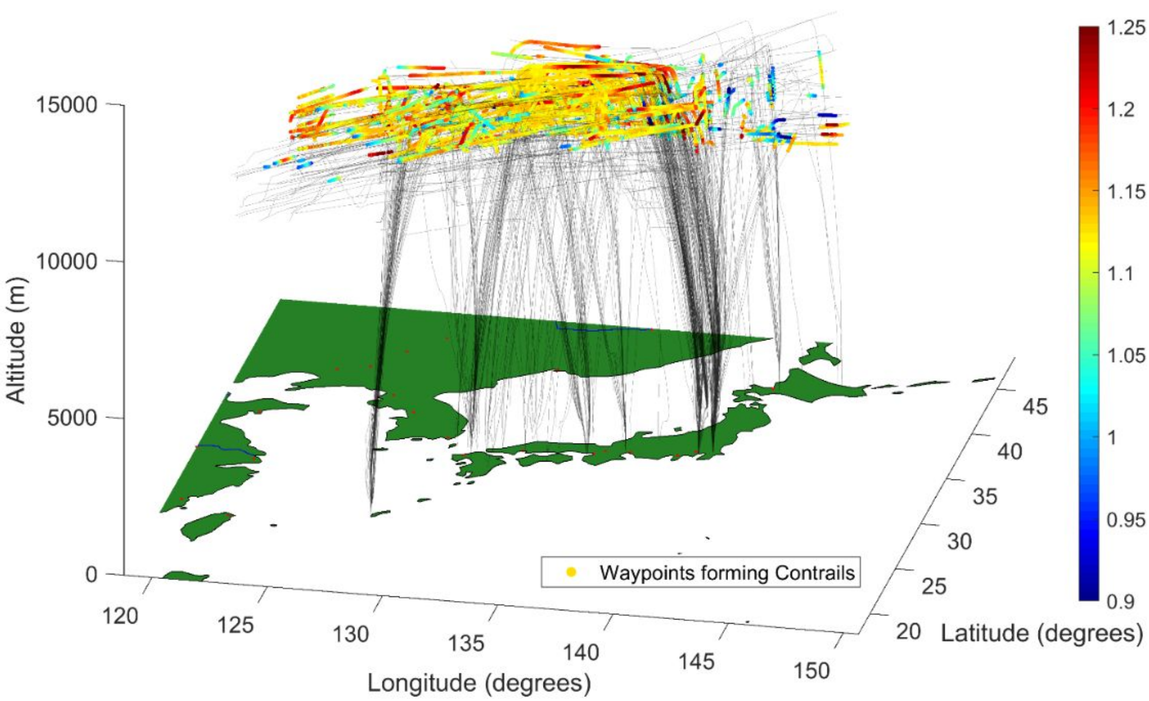

Figure S27: 3D visualisation of the flight trajectories in the CARATS Open Data. The location of individual waypoints forming contrails are also plotted on top of the flight trajectories, together with their the initial RHi for which contrails are formed (colour bar).

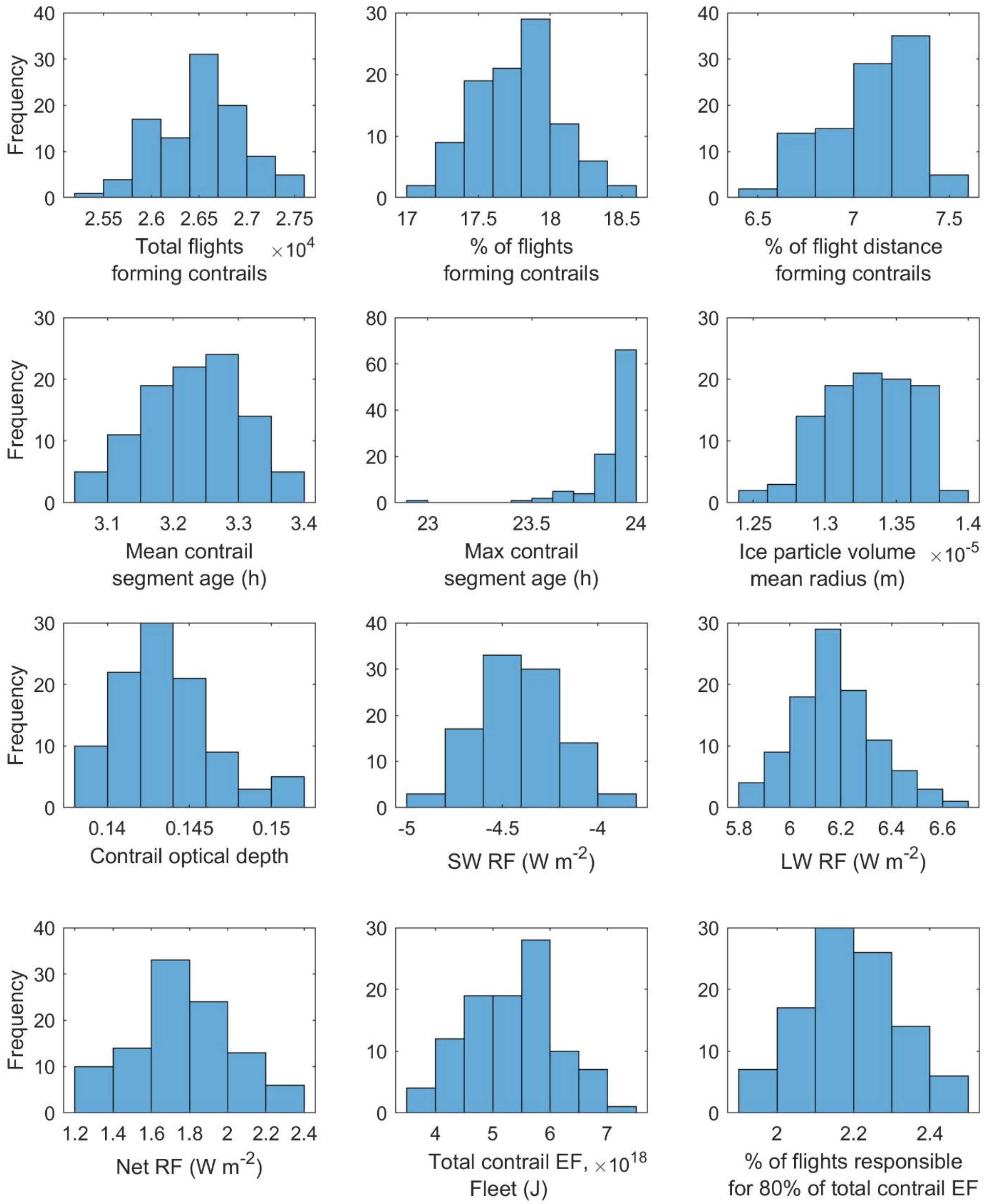

Figure S28: Histograms showing the uncertainty distribution of the fleet statistics, contrail characteristics and climate forcing aggregated across six weeks. These results are simulated using the ERA5 EDA meteorological dataset with a Monte Carlo simulation (100 runs).

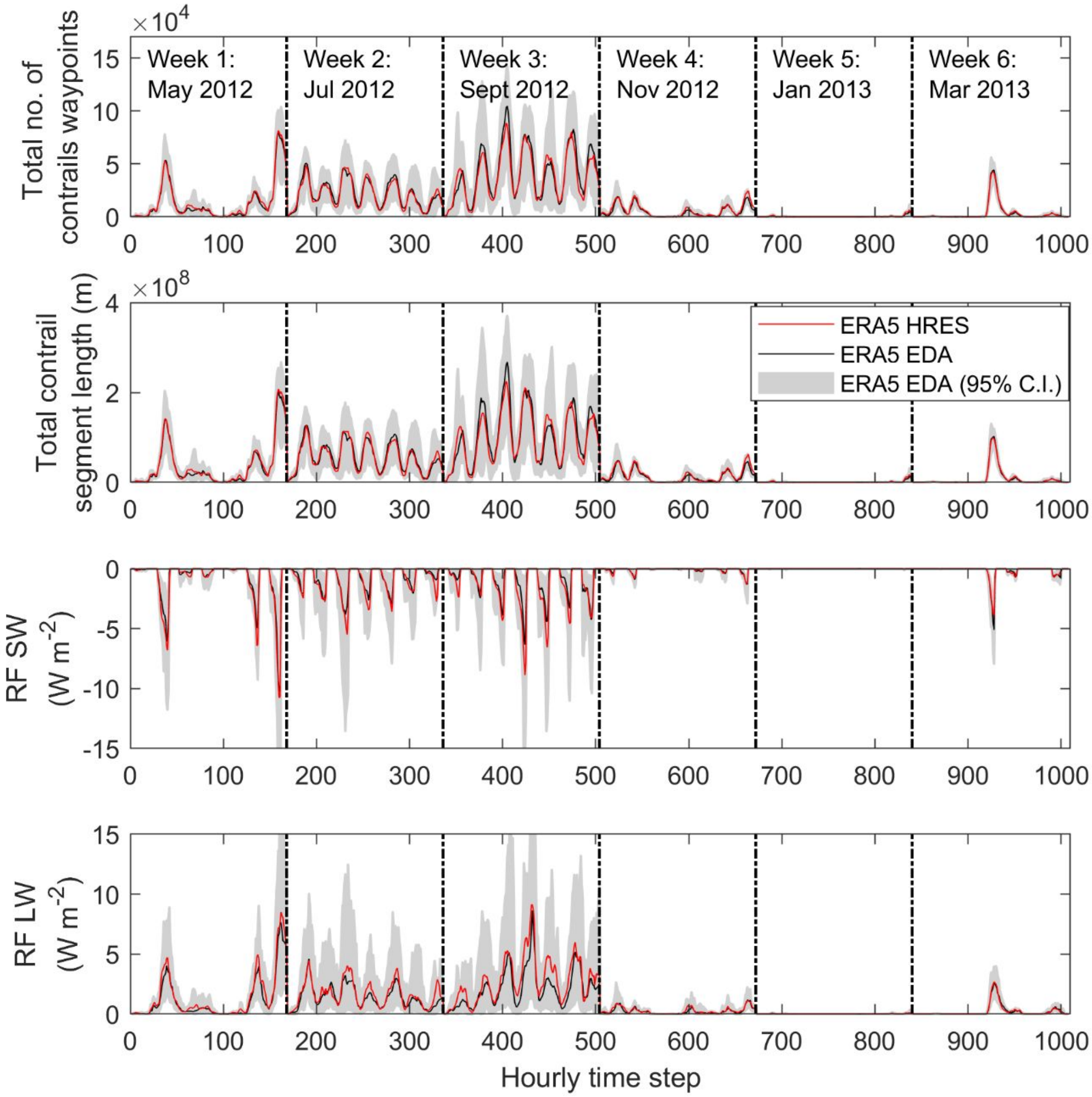

Figure S29: Outputs of the remaining contrail properties that were not presented in Figure 1 in the main text. The hourly time step covers all six weeks of simulation, where each week consist of 168 h (and time step). Contrails are simulated with CoCiP using meteorological inputs from the ERA5 HRES (red line) and the EDA (black lines, and the shaded region represents the 95% CI for the particular time step).

The histograms presented in Figure S28 show the range of the fleet-aggregated contrail characteristics and climate forcing, of which contrails are modelled using the ERA5 EDA meteorological dataset with a Monte Carlo simulation (100 runs). Apart from the maximum contrail segment age and average volume mean radius which follows a beta/exponential and a relatively uniform distribution respectively, the uncertainties for the simulated contrail properties and climate forcing generally follow a normal and lognormal distribution. The ranges of contrail characteristics and climate forcing (simulated using the ERA5 EDA) are also compared with the results from a nominal run of CoCiP using the higher-resolution ERA5 HRES: The hourly outputs for six contrail parameters (such as the total number of flights forming contrails, maximum contrail segment age, average contrail volume mean radius, optical depth (τ), net RF and the contrail EF aggregated across the fleet) were previously presented in Figure 1 in the main text, while Figure S29 shows the results of the remaining parameters (the total number of contrail waypoints, total contrail segment length, and average SW and LW RF for each time step). In general, the contrail properties simulated using the HRES are within the uncertainty bounds that are estimated from the EDA.

Additionally, the contrail characteristics and climate forcing arising from one single flight is also modelled to compare the range of uncertainty relative to the fleet-aggregated results. This flight, a Boeing B747-400 (Flight ID: FLT2429 on the 11th of July 2012), was selected because the nominal contrail EF (estimated with the ERA5 HRES) is the highest in the dataset. The trajectory of this particular flight is shown in Figure S30, and the histograms presented in Figure S31 show the uncertainty range and distribution of the different contrail properties. 100 Monte Carlo simulations for this particular flight takes approximately 30 minutes of computational time.

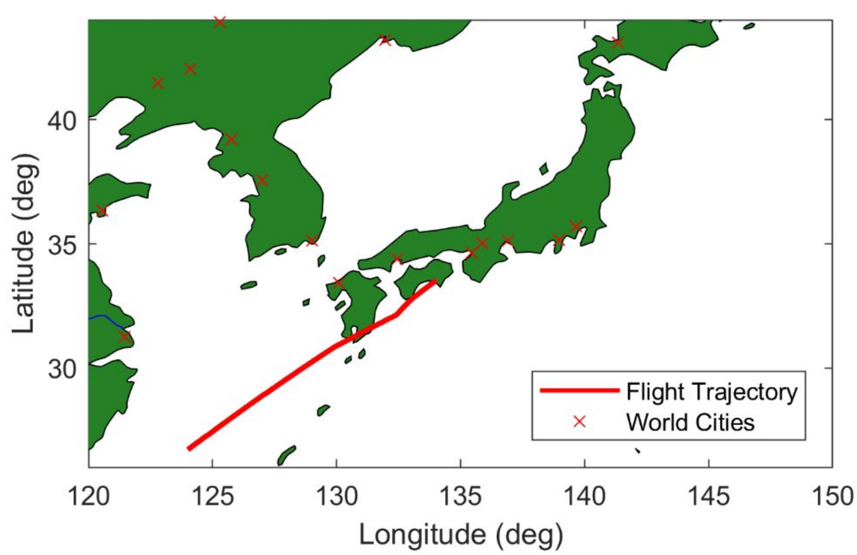

Figure S30: Flight trajectory for FLT2429 on the 11th of July 2012, a Boeing B747-400 which was selected to model the uncertainties in different contrail parameters arising from a single flight.

On average, the uncertainties for each contrail properties are around one to two orders of magnitude larger relative to the fleet-aggregated values: (i) 85.8% [15.6%, 88.4%] of the flight segment form contrails; (ii) the mean and maximum contrail segment ages are 8.10 [1.01, 10.6] h and 12.8 [3.19, 16.2] h respectively; (iii) the contrail τ is 0.104 [0.044, 0.202]; and (iv) the contrail net RF', EF and EF per unit length of contrail are 2.60 [-1.51, 7.14] W m^{-2}, 4.63 [-0.01, 16.6] $\times 10^{15}$ J, and 4.59 [-0.017, 15.4] $\times 10^{9}$ J m^{-1} respectively. Finally, we also note that the nominal contrail EF from this particular flight amounts to 0.086% of the nominal EF produced by the fleet, despite accounting for only 0.0022% of the total flight distance travelled by the fleet.

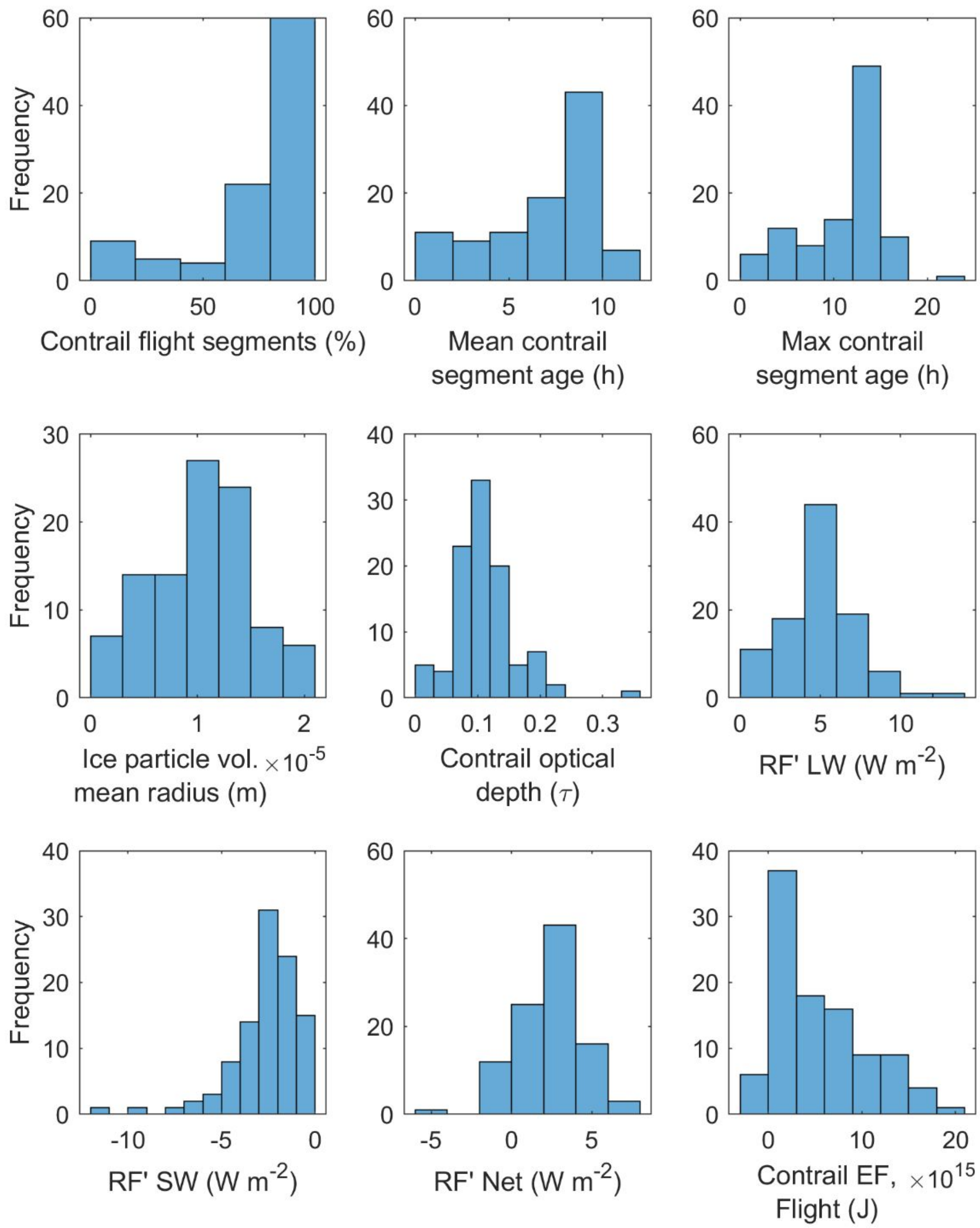

Figure S31: Histograms showing the uncertainty distribution of contrail characteristics and climate forcing that are produced by one single flight (FLT2429 on the 11th of July 2012). These results are simulated using the ERA5 EDA meteorological dataset with a Monte Carlo simulation (100 runs).

S6 Mitigation Solution 1: Small-scale Contrail Diversion Strategy

S6.1 Rationale

Given that only 2.0% to 2.5% of flights contribute to 80% of the contrail EF (as presented in Figure S32, showing the cumulative plot for the total contrail EF vs. the proportion of flights responsible for it), the implementation of a fleet-wide contrail diversion strategy might not be necessary.

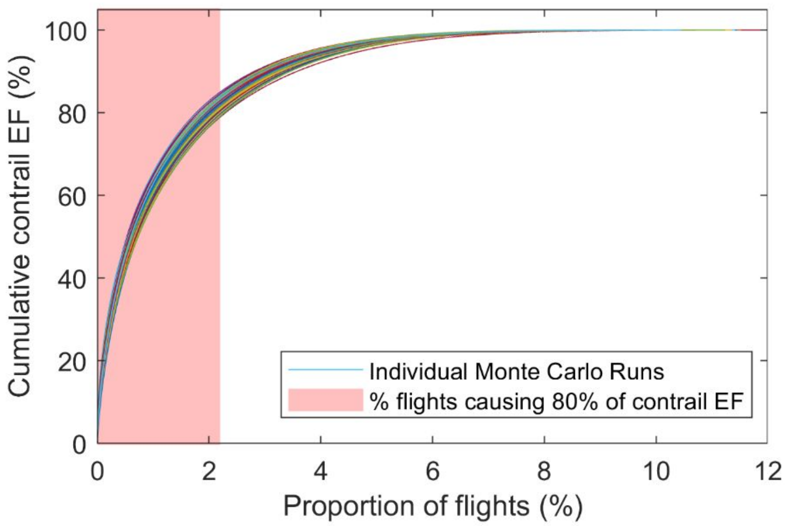

Figure S32: Cumulative plot showing the percentage of the total contrail EF (over the six one-week periods of air traffic data) versus the proportion of flights that is responsible for the contrail EF. The individual lines represent the results from each Monte Carlo simulation (n=100) which are simulated using the ERA5 EDA meteorological dataset, and the shaded regions (in red) represent the percentage of flights being responsible for 80% of the contrail EF.

A small-scale strategy which selectively diverts flights that contribute to the largest positive EF, could significantly reduce the contrail climate forcing and minimise the potential disruptions to air traffic management (ATM).

Figure S33 identifies the flights that contribute to 80% of the contrail EF for the six one-week periods of the CARATS Open Data. All the flights presented in Figure S35 have a positive EF because flights with a negative EF (cooling contrails) are not included. The average air traffic density (ATD) above 20,000 feet (shown in the right axis) is used to approximate the free airspace capacity that could be available for a diversion, and is calculated as follows[77],

$$\text{ATD}\ [\text{km}^{-1}\ \text{h}^{-1}] = \frac{\sum \text{Flight Distance Travelled}}{\text{Airspace Area}\ [\approx 3.476 \times 10^{6}\ \text{km}^{2}]}, \qquad \text{(S55)}$$

For a comparison, the ATD in the North Atlantic oceanic airspace ranges from 0.01 to 0.05 km^{-1} h^{-1}, and above 0.06 km^{-1} h^{-1} in North America and Europe[77].

As shown in Figure S33, flights with the largest warming EF predominantly occur between 15:00 and 06:00 Japan local time for reasons that are described in the main text. We also note that the time of day when the largest warming EF occurs also depend on seasonality. For example, during the summer (week of July-2012), contrails with the largest EF predominantly form later in the day (after 15:00 Japan local time), likely due to the late sunset time at around 19:00 local time, and contrails that were formed before 15:00 local time spends a larger proportion of time reflecting incoming solar radiation with a SW RF component. Conversely, contrails with a large EF are formed earlier in the day (10:00 to 15:00 local time) in spring and autumn (March-2012, May-2012 and September-2012) because of the long lifetime (> 8 h) and an earlier sunset time of around 17:45 to 18:30 local time. For the weeks of November-2012 and January-2013, these trends do not apply: Contrails with the largest EF are formed after 15:00 local time even when the sunset time occurs between 16:30 and 17:00 local time because the contrails formed during these weeks are generally short-lived (< 4 h).

Previous studies have shown that ice supersaturated regions (ISSR) typically have large horizontal extensions of 150 ± 250 km, but the vertical extensions are relatively shallow at around 0.7 ± 0.1 km (≈ 2300 ± 300 feet)[78–80]. A visual examination of the spatial distribution of the RHi and ambient temperature from the ERA5 HRES reanalysis (Figure S34) supports this statement: A small change in cruising altitude (± 2000 feet) could be sufficient to minimise the flight distance within regions where contrails could persist for long periods and spread, thereby reducing its lifetime and EF. Therefore, given the characteristics of an ISSR, a vertical diversion (via flight level changes) is preferred over a horizontal (lateral) diversion to minimise the increase in flight time, distance flown, fuel consumption and CO_2 emissions.

Based on these results (Figures S33 and S34), a small-scale strategy is proposed where flights are diverted vertically by ± 2000 feet, and diversions are prioritised for only flights with the largest contrail EF. The approach to implementing such a strategy is outlined in the next subsection.

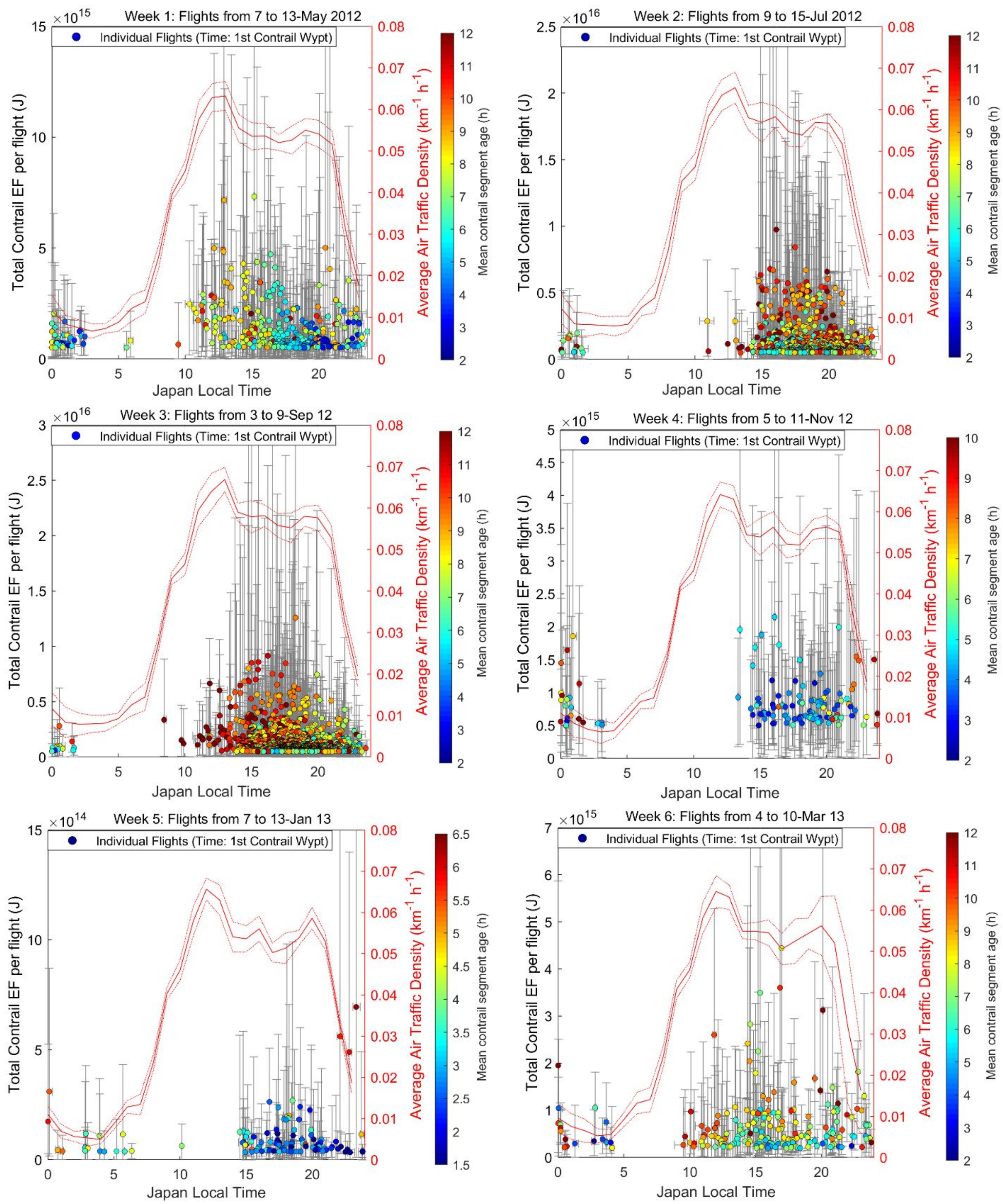

Figure S33: Flights that contribute to 80% of the total contrail EF and the times of day which these flights occur. Error bars denote the 95% CI. The air traffic density above 20,000 feet (average and standard deviation) for different times of the day is shown in the right axis, while data on the mean contrail segment age is shown by the symbol colour.

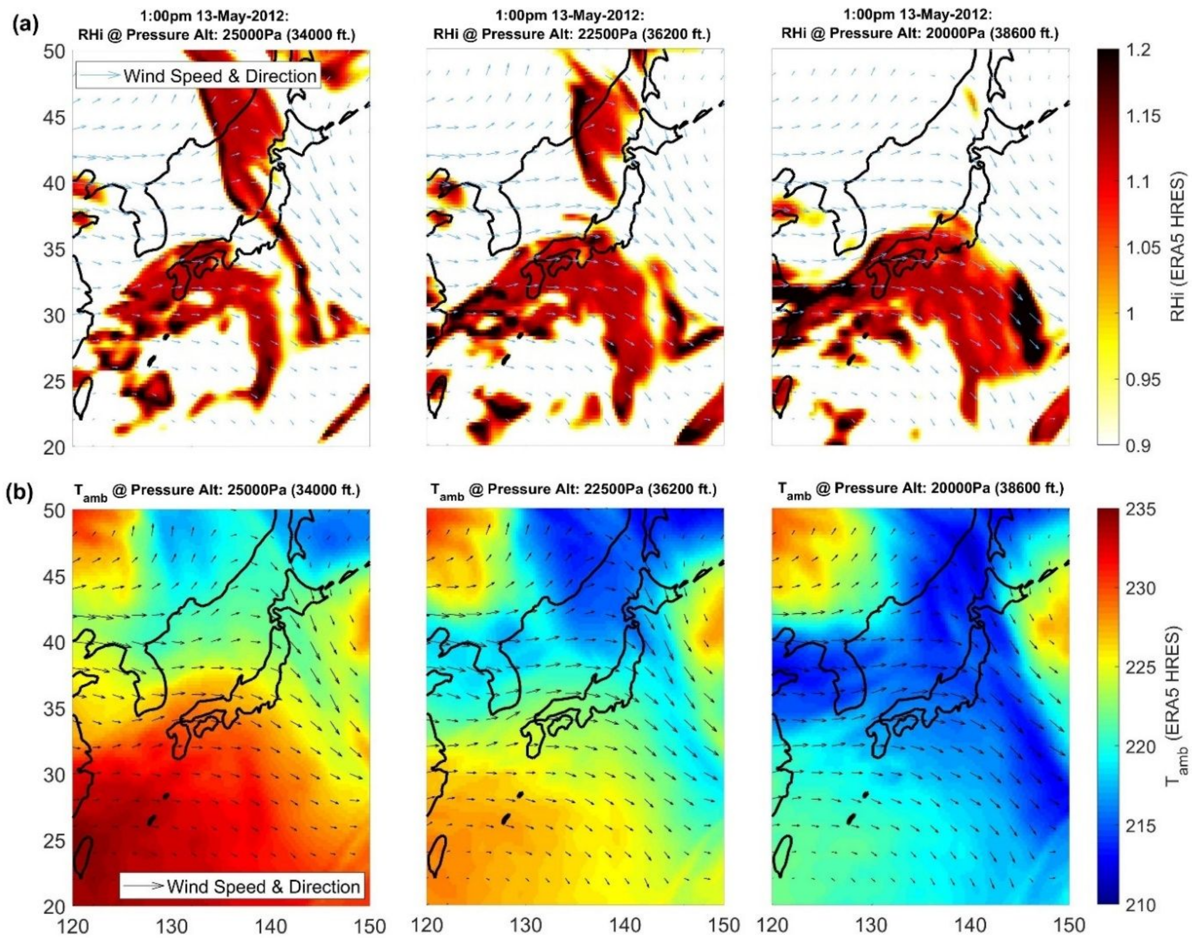

Figure S34: Spatial distribution of the RHi, ambient temperature and wind velocity vectors provided by the ERA5 HRES meteorological dataset at three distinct pressure altitudes: 25,000 Pa (34000 feet), 22,500 Pa (36200 feet), and 20,000 Pa (38600 feet).

S6.2 Approach

Figure S35 shows the flow chart outlining the procedure of this proposed small-scale diversion strategy. Results from the baseline scenario (SI §S5) is first used to identify the flights that contribute to 80% of the contrail EF. Alternative trajectories are then generated for these flights by modifying the cruising altitude by ± 2000 feet using the performance specifications for specific aircraft types provided by Eurocontrol[2], including the ROCD and altitude service ceiling. Examples of alternative trajectories are shown in Figure S36. These alternative trajectories also conform with the design of existing airspace structures where flights travelling at opposite directions are typically separated at vertical intervals of 1000 feet (ref.[81]).

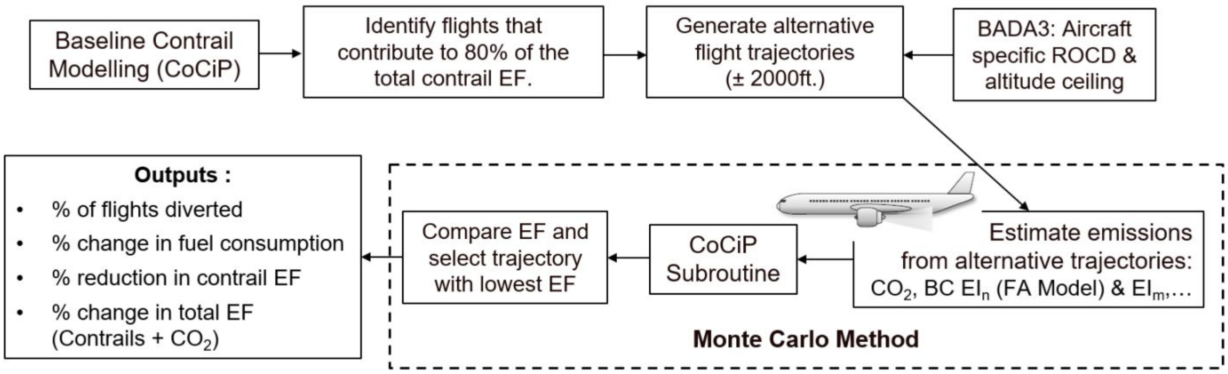

Figure S35: Flow chart outlining the procedure of a proposed small-scale contrail diversion strategy.

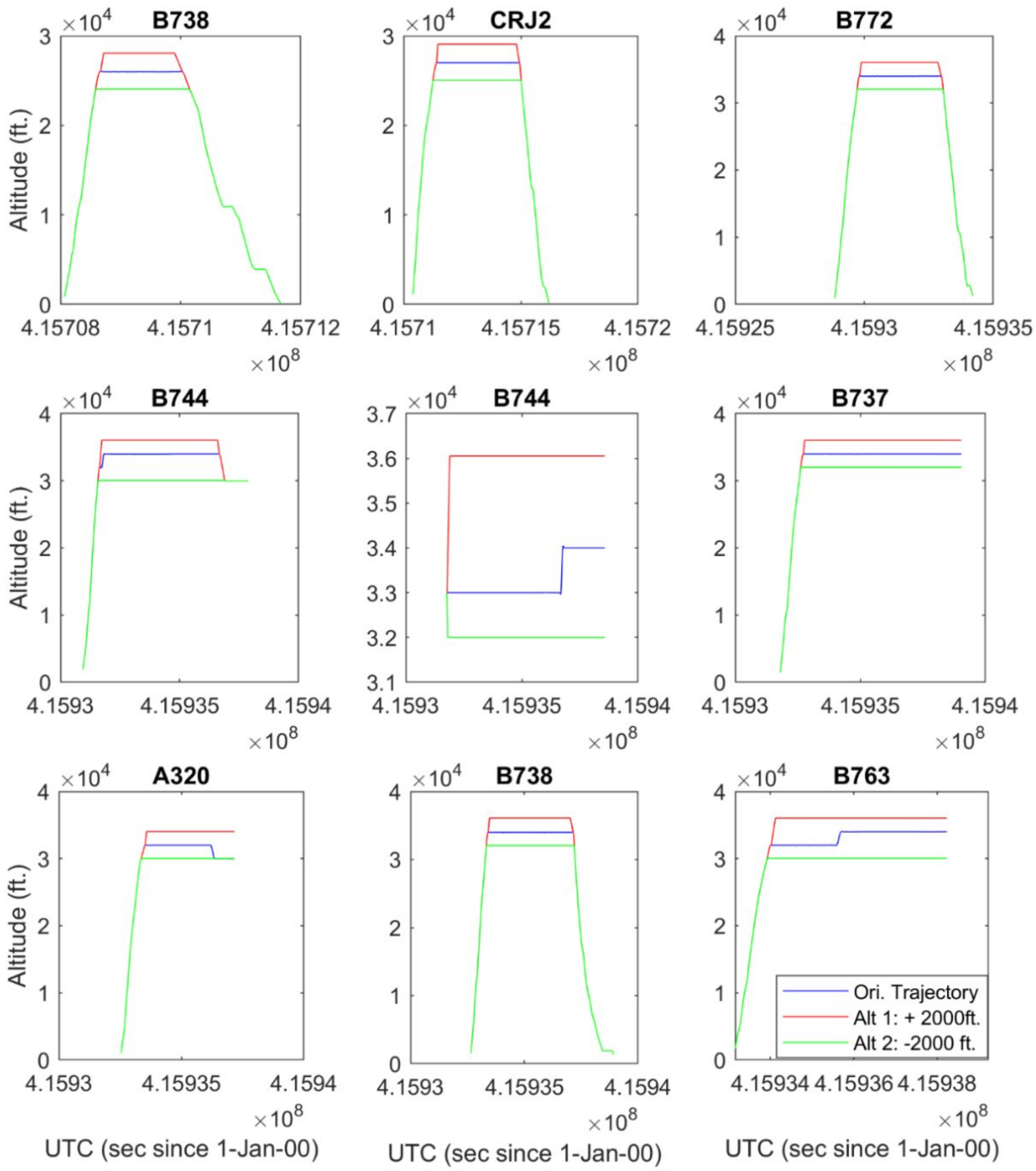

Figure S36: Examples of alternative trajectories, where the aircraft cruise altitude is modified by ± 2000 feet.

With the alternative trajectories now available, the same Monte Carlo simulation (outlined in the SI §S4.4) is then used to quantify uncertainties of the required model outputs. For each Monte Carlo simulation, distinct meteorological values provided by the ERA5 EDA are used to calculate the total fuel consumption from the original and alternative trajectories (BADA 3), BC EI_n (FA model), and the contrail EF (simulated with CoCiP). To account for the potential constraints in ATM, a strategy is formulated where: (i) all the flights that are identified to contribute to 80% of the contrail EF are instructed to divert during the night when the ATD is low (20:00 to 06:00 local time); while (ii) only a limited number of flights are allowed to divert during the times when air traffic is high but not at its peak (ATD < 0.06 km^{-1} h^{-1}, 15:00 to 20:00). For flights that are selected for a diversion, the trajectory yielding the lowest EF (which can be negative) is then selected. We note that mitigation is achieved not simply by contrail avoidance but by minimising the climate forcing of contrails, and therefore, the minimum selected is not a trajectory without contrails. After 100 runs, the 95% CI for various model outputs are calculated, including the percentage change in fuel consumption and reduction in contrail EF for individual flights and then aggregated across the fleet. Uncertainty in the total fuel consumption accounts for uncertainties in the ambient temperature and upper atmospheric winds (provided by the ERA5 EDA) but does not include known limitations[82,83] of BADA 3 (which was described in the main text).

The diversion of flights requires trade-offs to be made between minimising the contrail climate forcing and the potential increase in fuel consumption (and CO_2 emissions). To compare the climate forcing of contrails and CO_2 emissions, the absolute global warming potential (AGWP)[84], the time integral of the RF of CO_2 over time, is used as a first-order approximation to quantify the CO_2 EF and total EF (contrails plus CO_2),

$$\mathrm{CO_2\ EF\ [J]} = \int_0^{\mathrm{TH}} \mathrm{RF}_{\mathrm{CO_2}} \mathrm{d}t \times \mathrm{S_{Earth}} = [\mathrm{AGWP_{100}} \times (365 \times 24 \times 60^2)] \times \mathrm{TFC} \times \mathrm{EI_{CO2}} \times \mathrm{S_{Earth}}, \quad \text{(S56)}$$

where TH is the time horizon, TFC is the total fuel consumption, $\mathrm{AGWP_{100\ years}}$ is the AGWP with a 100-year TH (92.5 [68, 117] $\times 10^{-15}$ yr Wm^{-2} per kg-CO_2 at a 95% CI[84]), $\mathrm{EI_{CO2}}$ is the emissions index for CO_2 (3.16 kg kg^{-1})[85] and $\mathrm{S_{Earth}}$ (5.101×10^{14} m^2)[86] is the Earth's surface area. Although approximately 25% of the emitted CO_2 remains in the atmosphere after a millennium, we applied the 100-year TH to be in line with the Kyoto Protocol[84], and assumed that the AGWP is normally distributed in the Monte Carlo simulation. A 20- and 1000-year TH[84] are also used to determine the sensitivity of the CO_2 EF due to the choice of TH for the AGWP.

S6.3 Results & Discussion

For the six weeks of data, the results (presented in Figure 4a the main text) shows a significant mitigation potential where diverting up to 1.7% of the flights could reduce the contrail EF by 59.3% [52.4%, 65.6%]. On average, the results suggest that the contrail EF is more efficiently reduced when the aircraft cruising altitude is reduced by 2000 feet (57.9% of diverted flights) relative to an altitude increase of +2000 feet (42.1% of diverted flights). However, when the results are disaggregated into individual weeks, Figure S37 shows that flying lower (-2000 feet) reduces the contrail EF more efficiently during the summer months (64.2% of the diverted flights on average in May, July and September 2012), while the algorithm recommends flights to fly higher during the winter months (63.6% of the diverted flights on average in November 2012, January and March 2013). This could be due to the seasonal variation of the tropopause height[87], which tends to be higher during the summer months and the aircraft might not be able to reach the lower and drier stratosphere even when the cruising altitude is increased. Conversely, the lower tropopause height during the winter months imply that an increase in cruising altitude by 2000 feet could be sufficient for the aircraft to reach at the stratosphere.

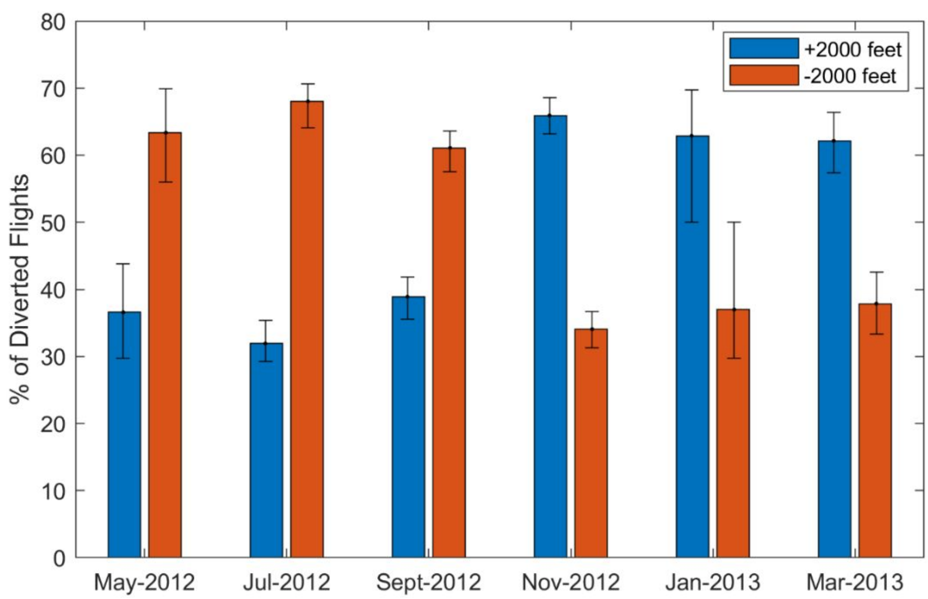

Figure S37: Percentage of cases where the diverted flights maximise the reduction in contrail EF by modifying their cruising altitude by ± 2000 feet. The results are broken down into individual weeks. Error bars denote the 95% CI.

For some flights, the percentage change in fuel consumption is greater than ± 5% (Figure S38), which has been verified to be accurate and realistic. For example, Figure S39 provides an example of a flight with a 40% increase in fuel consumption from the alternative trajectory (of increasing the cruising altitude by 2000 feet): For this particular flight, the total flight time over the Japanese airspace is 894 s (14.9 min), and hence, the absolute value of the total fuel consumption from the original trajectory is only 920 kg. The flight then spends 222 s (24.8% of the flight time in the Japanese airspace) climbing from 38,000 feet to 40,000 feet, resulting in a higher $\dot{m}_{\mathrm{f}}$ and the total fuel consumption computed by BADA3 from the new trajectory is 1292 kg (40.4% increase). However, due to the short flight distance (that is captured by the CARATS Open Dataset), the contrails length and EF produced in the Japanese airspace is small, and hence not selected for diversion (and not reflected in Figure S38).

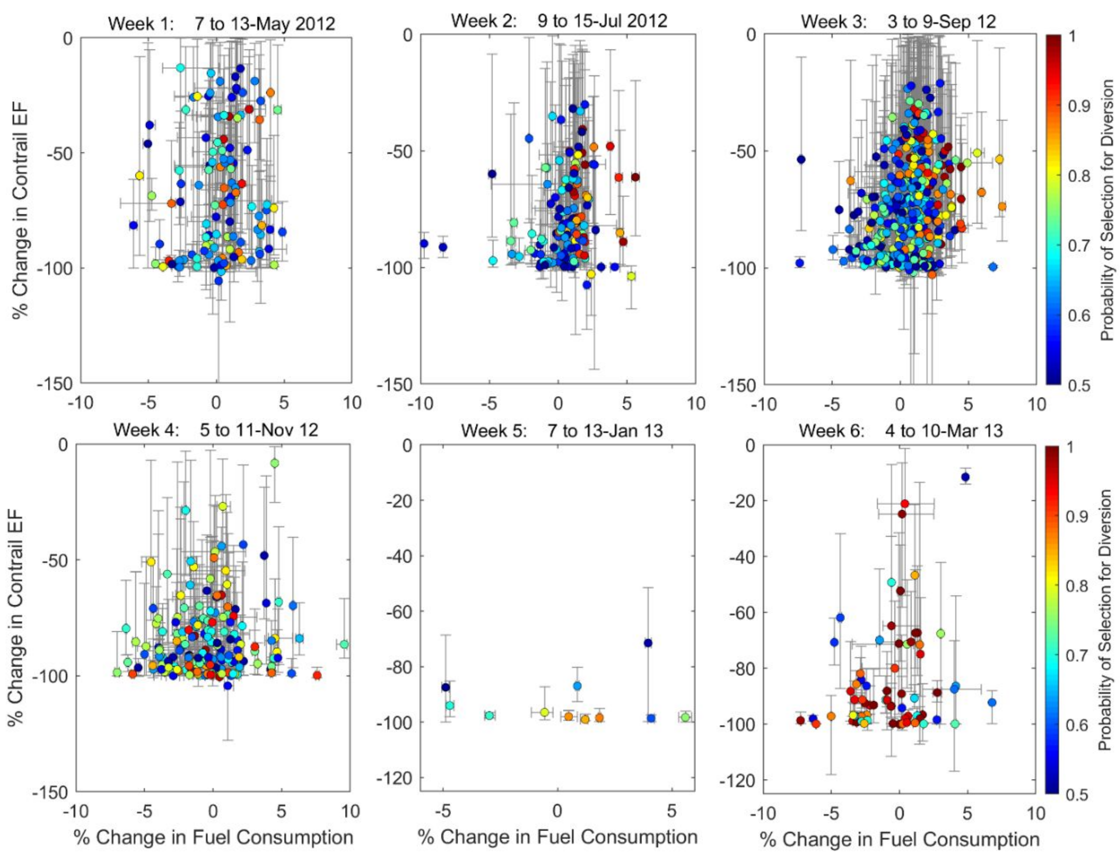

Figure S38: Percentage change in the contrail EF vs. the change in fuel consumption for each flight that are selected for a diversion. Error bars for both the percentage change in contrail EF and fuel consumption denote the uncertainties at a 95% CI.

The CO_2 EF (in units of J) is approximated using Eq. (S56), which assumes that the CO_2 emitted locally gets well-mixed and distributed over the Earth atmosphere at a mixing time far smaller than the mean atmospheric lifetime of CO_2. Using Eq. (S56) and an AGWP time horizon of 100 years, the CO_2 EF per unit mass of fuel burned is estimated to be 4.70 [3.45, 5.95] $\times 10^9$ J kg^{-1}. The estimated mean fuel consumption for all flights in the Japanese airspace (7.26 kg km^{-1}) is 53% higher than the estimated global mean fuel consumption from Schumann et al.[74] (4.75 kg km^{-1}). This is because 58% of all flights in the CARATS Open Data are short-haul domestic flights, where a higher proportion of time is spent in the take-off and climb phase of flight. Using our mean fuel consumption value of 7.26 kg km^{-1}, the CO_2 EF per flight distance is 3.41 [2.50, 4.32] $\times 10^7$ J m^{-1}. This value can be used as a reference when comparing with the contrail EF values per flight distance, which has an average of 5.35 [3.82, 6.62] $\times 10^7$ J m^{-1} over the six one-week periods in the Japanese airspace.

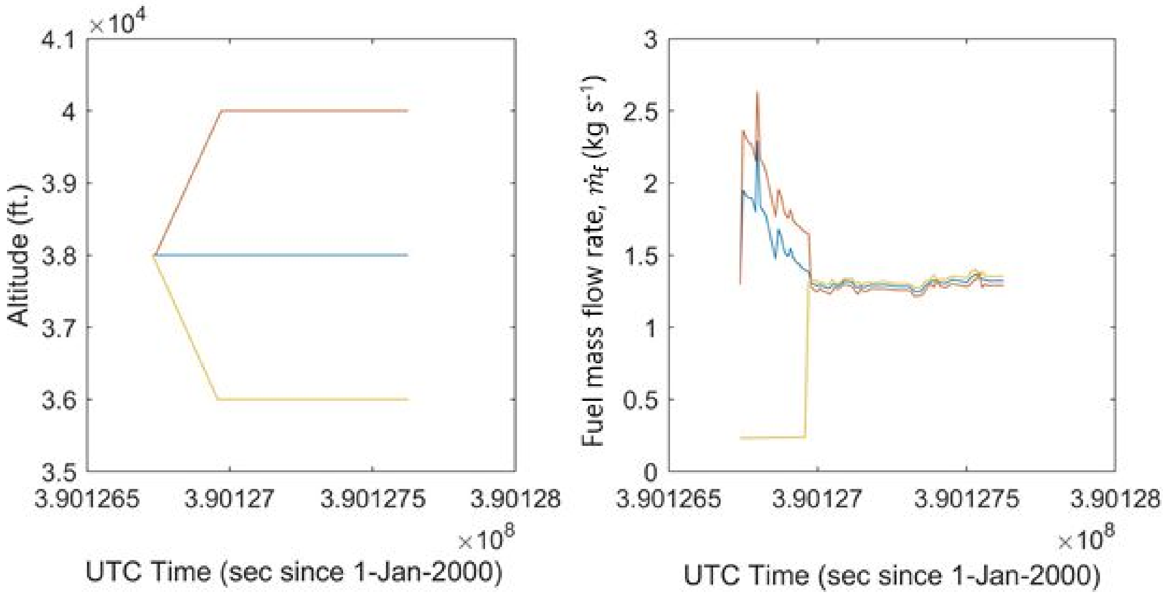

Figure S39: Example of a flight in which the percentage change in fuel consumption from flying the alternative trajectory (+2000 feet in cruising altitude) is greater than 10%.

For the entire fleet, Figure S40 shows the reduction in the total (nominal) EF versus the percentage of flights that are diverted. The baseline scenario (0% of flights diverted) show that 60.8% of the total EF originate from contrails, while the remaining 39.2% are from the CO_2 emissions from the entire fleet. For the six weeks of data, diverting up to 1.7% of the flights could reduce the total EF by 35.6% [27.6%, 44.2%]. The reduction in total EF is contributed almost entirely by the reduction in contrail EF, while the change in the CO_2 EF as a result of a diversion appears to be negligible. The sensitivity of CO_2 EF and the percentage reduction in total EF (contrails plus CO_2) due to the choice of AGWP TH is summarised in Table 3 in the main text. If an AGWP of a longer TH of

1000 years, $AGWP_{1000\ years}$ (548 [380, 716] $\times 10^{-15}$ yr Wm^{-2} per kg-CO_2 at a 95% CI[84]) is used to quantify the EF of CO_2, this sensitivity analysis suggest that the overall reduction in the total EF will be significantly smaller at 12.2% [7.55%, 23.1%]. In contrast, the total EF could be reduced by up to 50.1% [44.6%, 55.4%] if a shorter TH of 20-years (25.2 [20.7, 29.6] $\times 10^{-15}$ yr Wm^{-2} per kg-CO_2) is used.

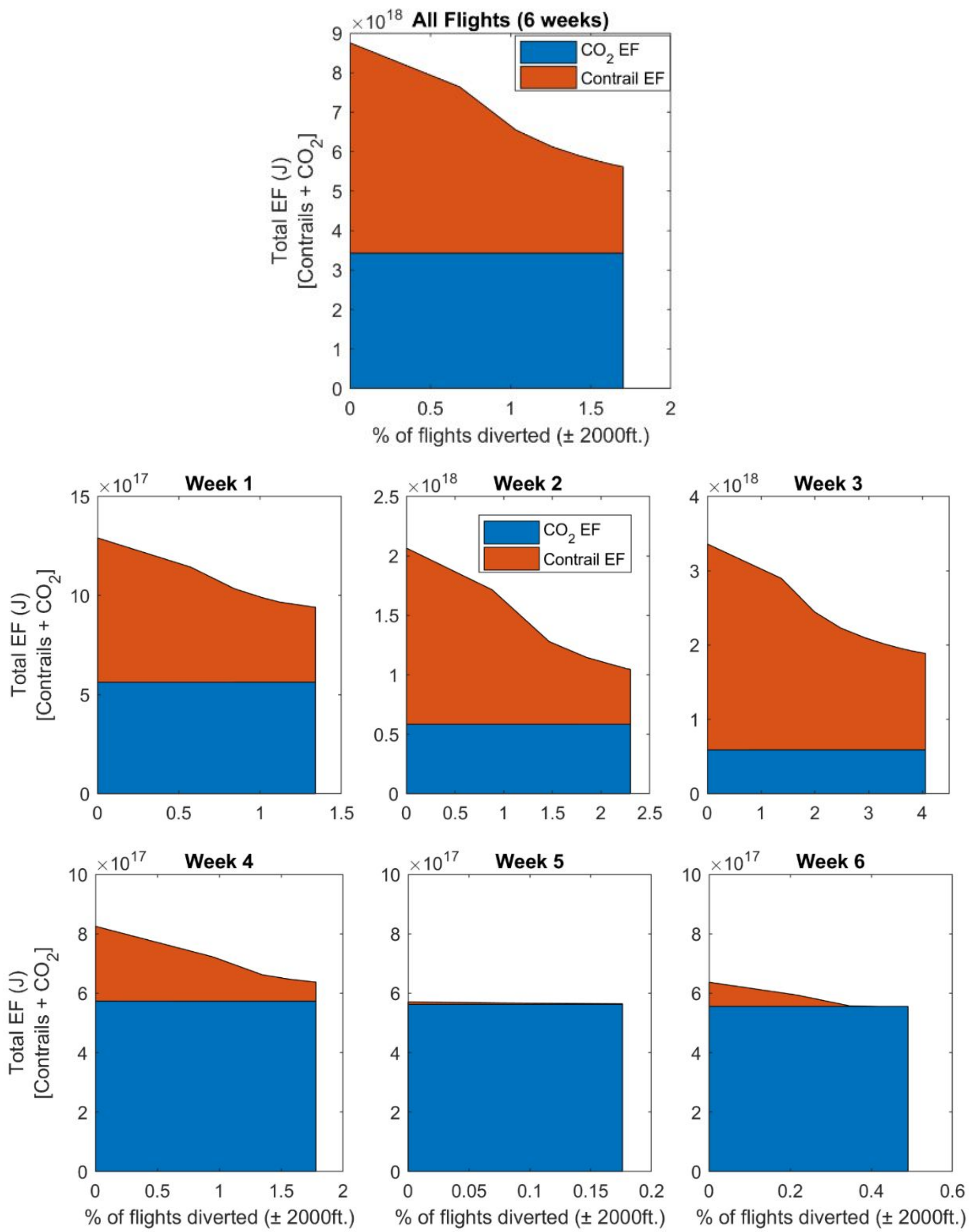

Figure S40: Reduction in the total (nominal) EF vs. the percentage of flights diverted.

While the potential changes in the global mean surface temperature, quantified using the Absolute Global Temperature Potential (AGTP) are also important, we have refrained from quantifying it because the current level of scientific understanding remains low[88].

S7 Mitigation Solution 2: Widespread Adoption of DAC Aircraft

Alternatively, a widespread use of aircraft powered by DAC engines could reduce the climate forcing of contrails over the longer term. For the baseline scenario (with no diversion), the contrail properties produced by aircraft powered by SAC and DAC engines are separately analysed. We note that SAC aircraft represent the majority of the flights in the CARATS Open Data (84%, or 35076 flights) while DAC aircraft represent around 16% of the dataset (6351 flights) over the six weeks. The methodology used to identify DAC aircraft were previously outlined in §S2.4. Figure S41 shows the distribution of the nominal contrail characteristics and climate forcing from individual aircraft powered by SAC and DAC engines for the baseline scenario. On average, the contrails produced by DAC engines have an average age of up to 10 h and τ of up to 0.8, relative to SAC aircraft with an average age and τ of up to 13.5 h and 1 respectively. Therefore, the magnitude and range of the contrail net RF' and EF produced by DAC aircraft are smaller relative to SAC aircraft.

A hypothetical scenario is formulated where all aircraft in the fleet are assumed to be powered by DACs. Under this scenario and coupled with the same Monte Carlo simulation, the fleet-aggregated contrail characteristics and climate forcing (Table S7) are compared with the baseline scenario with no diversion (results shown in Figure S42). The total and percentage of flights (and distance) forming contrails remains unchanged, but smaller values are computed for the fleet-average: (i) mean contrail segment age (-19.5% [-25.3%, -12.5%]); (ii) τ (-33.1% [-38.8%, -27.2%]); (iii) net RF (-27.4% [-37.7%, -18.9%]); and (iv) contrail EF (-68.8% [-82.1%, -45.2%]) relative to the baseline scenario. The uncertainty distribution of these variables (simulated under the hypothetical scenario) are similar to the base case, apart from the maximum contrail age which showed that a larger and near uniform distribution of between 18 to 24 h. Finally, a combination of the fleetwide adoption of DACs and the small-scale diversion strategy could reduce the contrail EF by up to 91.8% [88.6%, 95.8%] (Figure S43a), and a reduction of up to 56.5% [43.9%, 70.3%] for the total EF (Figure S43b). The large uncertainties in the percentage reduction in contrail EF in week 6 (Figure S43a) is due to a small denominator (baseline contrail EF = 8.14×10^{16} J).

Table S7: Fleet-average contrail characteristics and climate forcing over six weeks, which are simulated under the hypothetical scenario where all aircraft are assumed to be powered by a DAC engine.

CoCiP Outputs (6 weeks, fleet average, assuming that all aircraft are powered by DAC engines)	ERA5 EDA				% Difference in Nominal Values w.r.t. Base Case
	Nominal	Lower bound	Upper bound	% Uncertainty w.r.t. Nominal	
Total no. flights forming contrails	26517	25648	27360	[-3.28%, +3.18%]	-0.06%
% of flights forming contrails	17.8	17.2	18.4	[-3.28%, +3.18%]	-0.04%
% of flight distance forming contrails	7.14	6.64	7.74	[-6.91%, +8.46%]	-0.13%
Mean contrail segment age (h)	2.61	2.51	2.70	[-3.68%, +3.68%]	-19.5%
Maximum contrail segment age (h)	21.8	18.5	23.9	[-14.2%, +10.8%]	-9.94%
Ice particle volume mean radius (µm)	17.3	16.7	17.8	[-3.53%, +3.01%]	29.9%
Contrail optical depth (τ)	0.096	0.092	0.101	[-3.55%, +5.75%]	-33.1%
SW RF (W m^{-2})	-3.13	-3.39	-2.80	[-8.25%, +10.6%]	-29.2%
LW RF (W m^{-2})	4.37	4.17	4.67	[-4.71%, +6.68%]	-29.0%
Net RF (W m^{-2})	1.26	0.99	1.59	[-22.0%, +26.0%]	-27.4%
Contrail EF (× 10^{18} J)	1.68	1.19	2.11	[-29.2%, +25.3%]	-68.8%
EF per contrail m (× 10^{8} J m^{-1})	2.35	1.71	2.89	[-27.3%, +23.0%]	-68.7%
% of flights responsible for 80% of warming EF	2.24	2.03	2.48	[-9.46%, 10.7%]	2.33%

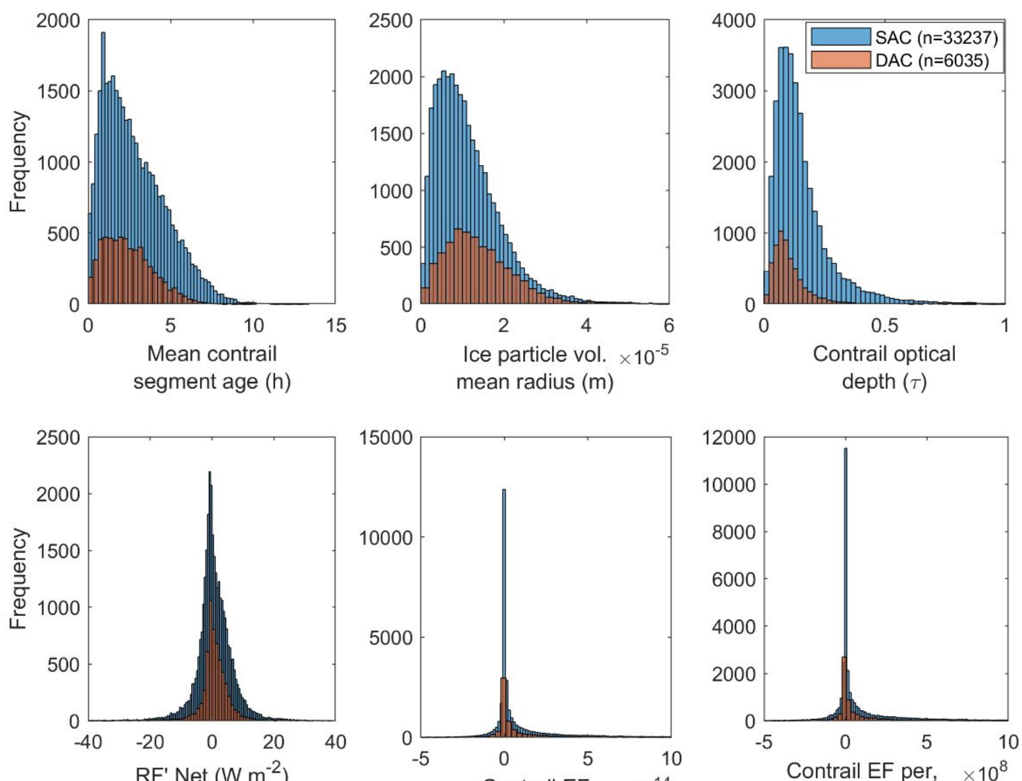

Figure S41: Distribution of the nominal contrail characteristics and climate forcing for aircraft powered by SAC (33237 flights) and DAC (6035 flights) engines over Japan for the baseline scenario. These results (baseline scenario) are simulated with CoCiP using meteorological inputs from the ERA5 EDA.

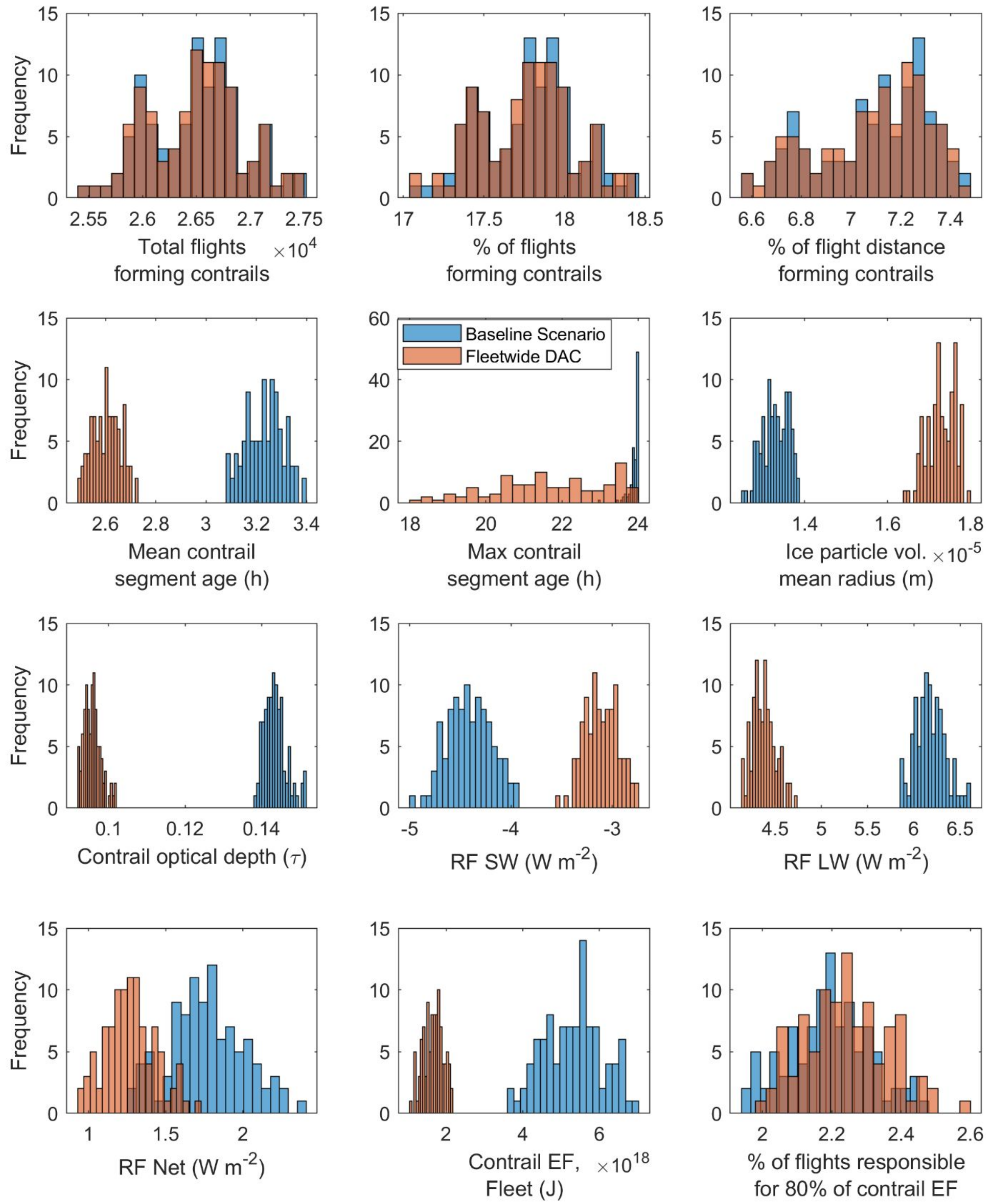

Figure S42: Histograms comparing the uncertainty distribution of the fleet statistics, contrail characteristics and climate forcing for the baseline scenario (blue bars) versus the hypothetical scenario where all aircraft are assumed to be powered by a DAC engine (red bars). These results are simulated using the ERA5 EDA meteorological dataset with a Monte Carlo simulation (100 runs).

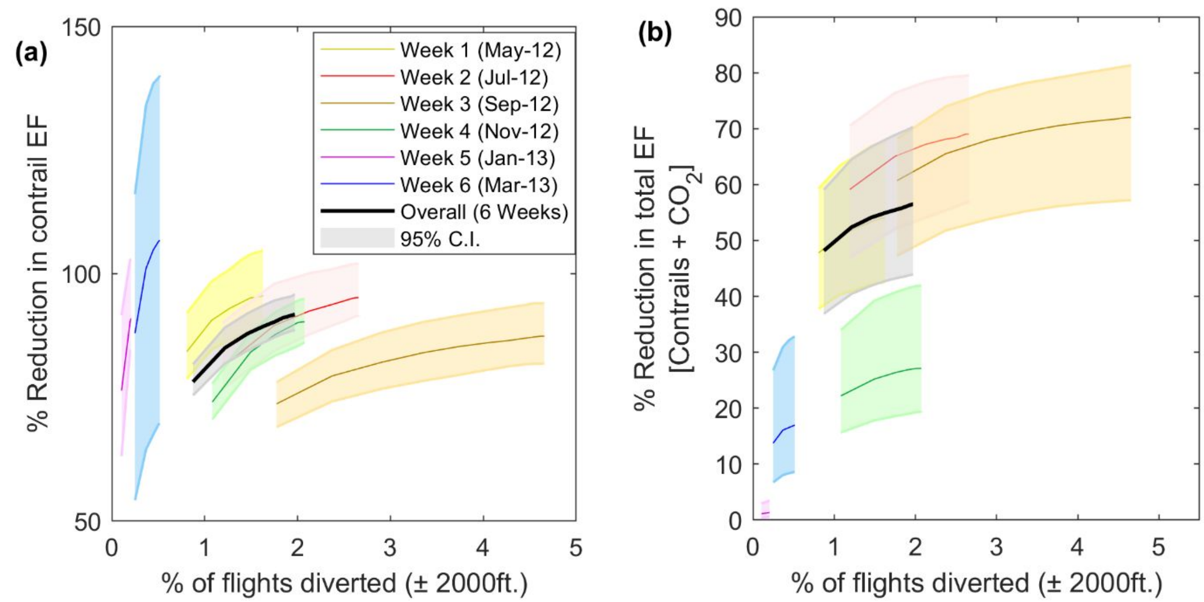

Figure S43: Percentage reduction in the (a) contrail EF and (b) total EF (contrails and CO_2 emissions) vs. the percentage of flights that are diverted by ± 2000 feet for the combination of a fleetwide DAC adoption and small-scale diversion strategy. The results are aggregated for the overall dataset (six weeks) and disaggregated for specific weeks. The percentage of flights diverted do not fall to 0% because all flights that contribute to 80% of the warming EF are allowed to divert at night.

END OF SUPPLEMENTARY INFORMATION

References

1. JCAB. On the use of “CARATS Open Data”. Ministry of Land, Infrastructure and Transport, Japan Civil Aviation Bureau. Air Navigation Service Department. Air Navigation Services Planning Division. Committee for Promoting Renovation of the Air Traffic System. 2014.
2. Eurocontrol. *User Manual for the Base of Aircraft Data (BADA) Revision 3.12.* Vol EEC Techni. Eurocontrol Experimental Centre; 2014. https://www.eurocontrol.int/sites/default/files/field_tabs/content/documents/sesar/user-manual-bada-3-12.pdf.
3. Teoh R, Stettler MEJ, Majumdar A, Schumann U, Graves B, Boies A. A methodology to relate black carbon particle number and mass emissions. *J Aerosol Sci*. 2019;132:44-59. doi:10.1016/J.JAEROSCI.2019.03.006
4. Schumann U. A contrail cirrus prediction model. *Geosci Model Dev*. 2012;5:543-580.
5. Schumann U, Baumann R, Baumgardner D, et al. Properties of individual contrails: A compilation of observations and some comparisons. *Atmos Chem Phys Discuss*. 2017:1-62.
6. Shigetomi S, Matsuda H, Kozuka T, Miyazawa Y. An Evaluation of CARATS Open Data Accuracy (Japanese Title: CARATS Open Data の精度に関する一検討). *Aerosp Technol Japan*. 2016;15:15-21.
7. Tobaruela G. A Framework to assess the ability of automation to deliver capacity targets in European airspace. *PhD Thesis*. 2015.
8. Lovegren J, Hansman RJ. Estimation of Potential Aircraft Fuel Burn Reduction in Cruise Via Speed and Altitude Optimization Strategies. April 2011. https://dspace.mit.edu/handle/1721.1/62196#files-area. Accessed February 11, 2019.
9. Savitzky A, Golay MJE. Smoothing and Differentiation of Data by Simplified Least Squares Procedures. *Anal Chem*. 1964;36(8):1627-1639. doi:10.1021/ac60214a047
10. Press WH, Teukolsky SA, Vetterling WT, Flannery BP. Numerical Recipes in Fortran 77: The Art of Scientific Computing. Cambridge University. Chapter 14.8 Savitzky-Golay Smoothing Filters. *Press Cambridge*. 1992.
11. Schafer R. What Is a Savitzky-Golay Filter? [Lecture Notes]. *IEEE Signal Process Mag*. 2011;28(4):111-117. doi:10.1109/MSP.2011.941097
12. Robusto CC. The Cosine-Haversine Formula. *Am Math Mon*. 1957;64(1):38. doi:10.2307/2309088
13. Hennermann K, Berrisford P. ERA5 Data Documentation. European Centre for Medium-Range Weather Forecast (ECMWF). https://confluence.ecmwf.int/display/CKB/ERA5+data+documentation#ERA5datadocumentation-Ensemblemeansandstandarddeviations. Published 2019. Accessed March 22, 2019.
14. European Commission. *COMMISSION REGULATION (EU) 2016/646 of 20 April 2016 - Amending Regulation (EC) No 692/2008 as Regards Emissions from Light Passenger and Commercial Vehicles (Euro 6).*; 2016. https://eur-lex.europa.eu/legal-content/EN/TXT/PDF/?uri=CELEX:32016R0646&from=EN.

Accessed February 11, 2019.

15. Wasiuk DK, Lowenberg MH, Shallcross DE. An aircraft performance model implementation for the estimation of global and regional commercial aviation fuel burn and emissions. *Transp Res Part D Transp Environ*. 2015;35:142-159.

16. Abrahamson JP, Zelina J, Andac MG, Vander Wal RL. Predictive Model Development for Aviation Black Carbon Mass Emissions from Alternative and Conventional Fuels at Ground and Cruise. *Environ Sci Technol*. 2016;50(21):12048-12055.

17. Anderson BE, Beyersdorf AJ, Hudgins CH, et al. Alternative aviation fuel experiment (AAFEX). *Rep No NASA/TM-2011-217059*. 2011.

18. Stettler MEJ, Boies A, Petzold A, Barrett SRH. Global civil aviation black carbon emissions. *Environ Sci Technol*. 2013;47(18):10397-10404.

19. Wey CC, Anderson BE, Hudgins C, et al. Aircraft particle emissions experiment (APEX). 2006.

20. Stettler MEJ, Eastham S, Barrett SRH. Air quality and public health impacts of UK airports. Part I: Emissions. *Atmos Environ*. 2011;45(31):5415-5424. doi:http://dx.doi.org/10.1016/j.atmosenv.2011.07.012

21. EASA. ICAO Aircraft Engine Emissions Databank. https://www.easa.europa.eu/document-library/icao-aircraft-engine-emissions-databank. Published 2011.

22. Durdina L, Brem BT, Setyan A, Siegerist F, Rindlisbacher T, Wang J. Assessment of Particle Pollution from Jetliners: from Smoke Visibility to Nanoparticle Counting. 2017.

23. Stickles R, Barrett J. *TAPS II Combustor Final Report. CLEEN Program*. Washington, DC.; 2013.

24. Neoh KG, Howard JB, Sarofim AF. Soot oxidation in flames. In: *Particulate Carbon*. Springer; 1981:261-282.

25. Boies AM, Stettler MEJ, Swanson JJ, et al. Particle emission characteristics of a gas turbine with a double annular combustor. *Aerosol Sci Technol*. 2015;49(9):842-855.

26. Lobo P, Durdina L, Smallwood GJ, et al. Measurement of aircraft engine non-volatile PM emissions: Results of the aviation-particle regulatory instrumentation demonstration experiment (A-PRIDE) 4 campaign. *Aerosol Sci Technol*. 2015;49(7):472-484.

27. Moore RH, Thornhill KL, Weinzierl B, et al. Biofuel blending reduces particle emissions from aircraft engines at cruise conditions. *Nature*. 2017;543(7645):411-415.

28. Agarwal A, Speth RL, Fritz TM, et al. SCOPE11 Method for Estimating Aircraft Black Carbon Mass and Particle Number Emissions. *Environ Sci Technol*. 2019;53(3):1364-1373. doi:10.1021/acs.est.8b04060

29. Wayson RL, Fleming GG, Iovinelli R. Methodology to estimate particulate matter emissions from certified commercial aircraft engines. *J Air Waste Manage Assoc*. 2009;59(1):91-100.

30. Stettler MEJ, Swanson JJ, Barrett SRH, Boies AM. Updated correlation between aircraft smoke number and black carbon concentration. *Aerosol Sci Technol*. 2013;47(11):1205-1214.

31. ICAO. *Annex 16: Environmental Protection, Volume II - Aircraft Engine Emissions. International Civil*

Aviation Organization. Montreal, Canada: International Civil Aviation Organization; 2008.

32. Durdina L, Brem BT, Abegglen M, et al. Determination of PM mass emissions from an aircraft turbine engine using particle effective density. *Atmos Environ*. 2014;99:500-507.
33. Lobo P, Hagen DE, Whitefield PD, Raper D. PM emissions measurements of in-service commercial aircraft engines during the Delta-Atlanta Hartsfield Study. *Atmos Environ*. 2015;104:237-245.
34. Stettler MEJ. No Title. *Aviat Emiss black carbon other air Pollut*. 2013.
35. Döpelheuer A, Lecht M. Influence of engine performance on emission characteristics. In: *Symposium of the Applied Vehicle Technology Pane-Gas Turbine Engine Combustion, Emissions and Alternative Fuels, Lisbon, Portugal*. Citeseer; 1998.
36. Cumpsty NA, Heyes A. *Jet Propulsion: A Simple Guide to the Aerodynamics and Thermodynamic Design and Performance of Jet Engines*. Third Edition. Cambridge University Press; 2015. https://books.google.co.uk/books?hl=en&lr=&id=YVsZCgAAQBAJ&oi=fnd&pg=PR7&dq=cumpsty+and+heyes&ots=b5F45iuQ7t&sig=kEueUVRfAA6sBdB3Hh-yvTrC-jI#v=onepage&q=cumpsty and heyes&f=false. Accessed July 10, 2019.
37. Petzold A, Döpelheuer A, Brock CA, Schröder F. In situ observations and model calculations of black carbon emission by aircraft at cruise altitude. *J Geophys Res Atmos*. 1999;104(D18):22171-22181.
38. Schumann U, Arnold F, Busen R, et al. Influence of fuel sulfur on the composition of aircraft exhaust plumes: The experiments SULFUR 1–7. *J Geophys Res Atmos*. 2002;107(D15).
39. Teoh R, Stettler M, Majumdar A. Aircraft black carbon particle number emissions—a new predictive method and uncertainty analysis. In: *21st ETH-Conference on Combustion Generated Naniparticles*. Zurich, Switzerland: ETH Zurich; 2017. http://www.nanoparticles.ch/archive/2017_Teoh_PO.pdf. Accessed February 13, 2019.
40. Roux E. *Turbofan and Turbojet Engines: Database Handbook*. Elodie Roux; 2007. https://books.google.co.uk/books?redir_esc=y&id=_5vA_5XK33sC&q=CFM56-2C1#v=onepage&q&f=false.
41. Cumpsty N. Jet Propulsion. A simple guide to the aerodynamic and thermodynamic design and performance of jet engines. Second Edition. 2003;1:13.
42. Abegglen M, Durdina L, Brem BT, et al. Effective density and mass-mobility exponents of particulate matter in aircraft turbine exhaust: Dependence on engine thrust and particle size. *J Aerosol Sci*. 2015;88:135-147. doi:10.1016/j.jaerosci.2015.06.003
43. Johnson TJ, Olfert JS, Symonds JPR, et al. Effective density and mass-mobility exponent of aircraft turbine particulate matter. *J Propuls Power*. 2015;31(2):573-582.
44. Park K, Kittelson DB, Zachariah MR, McMurry PH. Measurement of inherent material density of nanoparticle agglomerates. *J Nanoparticle Res*. 2004;6(2):267-272.
45. Dastanpour R, Rogak SN. Observations of a correlation between primary particle and aggregate size for soot particles. *Aerosol Sci Technol*. 2014;48(10):1043-1049.

46. Wiedensohler A, Wiesner A, Weinhold K, et al. Mobility particle size spectrometers: Calibration procedures and measurement uncertainties. *Aerosol Sci Technol*. 2018;52(2):146-164.

47. Coleman HW, Steele WG. *Experimentation, Validation, and Uncertainty Analysis for Engineers*. John Wiley & Sons; 2009.

48. ICAO. *2016 Environmental Report - On Board A Sustainable Future*. Montreal, Canada: International Civil Aviation Organization (ICAO); 2016. http://www.icao.int/environmental-protection/Documents/ICAO Environmental Report 2016.pdf.

49. Saltelli A, Ratto M, Andres T, et al. *Global Sensitivity Analysis: The Primer*. John Wiley & Sons; 2008.

50. Schumann U, Schlager H, Arnold F, et al. Pollution from aircraft emissions in the North Atlantic flight corridor: Overview on the POLINAT projects. *J Geophys Res Atmos*. 2000;105(D3):3605-3631. doi:10.1029/1999JD900941

51. Jeßberger P, Voigt C, Schumann U, et al. Aircraft type influence on contrail properties. *Atmos Chem Phys*. 2013;13(23):11965-11984.

52. Schumann U, Penner JE, Chen Y, Zhou C, Graf K. Dehydration effects from contrails in a coupled contrail–climate model. *Atmos Chem Phys*. 2015;15(19):11179-11199.

53. Schumann U, Graf K. Aviation-induced cirrus and radiation changes at diurnal timescales. *J Geophys Res Atmos*. 2013;118(5):2404-2421.

54. Schumann U, Jeßberger P, Voigt C. Contrail ice particles in aircraft wakes and their climatic importance. *Geophys Res Lett*. 2013;40(11):2867-2872.

55. Schumann U. On conditions for contrail formation from aircraft exhausts. *Meteorol Zeitschrift*. 1996;5:4-23.

56. Schumann U, Mayer B, Graf K, Mannstein H. A parametric radiative forcing model for contrail cirrus. *J Appl Meteorol Climatol*. 2012;51(7):1391-1406.

57. Hendricks J, Kärcher B, Lohmann U, Ponater M. Do aircraft black carbon emissions affect cirrus clouds on the global scale? *Geophys Res Lett*. 2005;32(12):n/a-n/a. doi:10.1029/2005GL022740

58. Caiazzo F, Agarwal A, Speth RL, Barrett SRH. Impact of biofuels on contrail warming. *Environ Res Lett*. 2017;12(11):114013.

59. Voigt C, Schumann U, Jurkat T, et al. In-situ observations of young contrails – overview and selected results from the CONCERT campaign. *Atmos Chem Phys*. 2010;10(18):9039-9056. doi:10.5194/acp-10-9039-2010

60. Giez A, Mallaun C, Zöger M, Dörnbrack A, Schumann U. Static Pressure from Aircraft Trailing-Cone Measurements and Numerical Weather-Prediction Analysis. *J Aircr*. 2017;54(5):1728-1737. doi:10.2514/1.C034084

61. Schmetz J, Menzel WP, Schmetz J, Menzel WP. A Look at the Evolution of Meteorological Satellites: Advancing Capabilities and Meeting User Requirements. *Weather Clim Soc*. 2015;7(4):309-320. doi:10.1175/WCAS-D-15-0017.1

62. Hersbach H, Dee D. ERA5 Reanalysis is in production. European Centre for Medium-Range Weather Forecast (ECMWF). https://www.ecmwf.int/en/newsletter/147/news/era5-reanalysis-production. Published

2016.

63. Hoffmann L, Günther G, Li D, et al. From ERA-Interim to ERA5: the considerable impact of ECMWF's next-generation reanalysis on Lagrangian transport simulations. *Atmos Chem Phys*. 2019;19(5):3097-3124. doi:10.5194/acp-19-3097-2019

64. Sonntag D. Advancements in the field of hygrometry. *Meteorol Zeitschrift*. 1994;3(2):51-66. doi:10.1127/metz/3/1994/51

65. Lamquin N, Gierens K, Stubenrauch CJ, Chatterjee R. Evaluation of upper tropospheric humidity forecasts from ECMWF using AIRS and CALIPSO data. *Atmos Chem Phys*. 2009;9(5):1779-1793. doi:10.5194/acp-9-1779-2009

66. Hennermann K, Berrisford P. Surface Radiation Parameters: Joule/m2 to Watt/m2. Copernicus Knowledge Base - ECMWF Confluence Wiki. https://confluence.ecmwf.int/pages/viewpage.action?pageId=104241513. Published 2018. Accessed June 17, 2019.

67. Tompkins AM, Gierens K, Rädel G. Ice supersaturation in the ECMWF integrated forecast system. *Q J R Meteorol Soc*. 2007;133(622):53-63. doi:10.1002/qj.14

68. Ovarlez J, Gayet J-F, Gierens K, et al. Water vapour measurements inside cirrus clouds in Northern and Southern hemispheres during INCA. *Geophys Res Lett*. 2002;29(16):60-1-60-64. doi:10.1029/2001GL014440

69. Koop T, Luo B, Tsias A, Peter T. Water activity as the determinant for homogeneous ice nucleation in aqueous solutions. *Nature*. 2000;406(6796):611-614. doi:10.1038/35020537

70. Korolev A V., Mazin IP. Supersaturation of Water Vapor in Clouds. *J Atmos Sci*. 2003;60(24):2957-2974. doi:10.1175/1520-0469(2003)060<2957:SOWVIC>2.0.CO;2

71. ECMWF. Forecast User Guide - 5.1 Generation of the Ensemble, Ensemble of Data Assimilations (EDA). https://confluence.ecmwf.int/display/FUG/Ensemble+of+Data+Assimilations+-+EDA. Published 2019.

72. MathWorks. sobolset - Sobol quasirandom point set. https://uk.mathworks.com/help/stats/sobolset.html. Published 2019. Accessed August 30, 2019.

73. Abegglen M, Brem BT, Ellenrieder M, et al. Chemical characterization of freshly emitted particulate matter from aircraft exhaust using single particle mass spectrometry. *Atmos Environ*. 2016;134:181-197.

74. Schumann U, Graf K, Mannstein H. Potential to reduce the climate impact of aviation by flight level changes. In: *3rd AIAA Atmospheric Space Environments Conference*. Honolulu, Hawaii: American Institute of Aeronautics and Astronautics; 2011. doi:10.2514/6.2011-3376

75. Vázquez-Navarro M, Mannstein H, Kox S. Contrail life cycle and properties from 1 year of MSG/SEVIRI rapid-scan images. *Atmos Chem Phys*. 2015;15(15):8739-8749. doi:10.5194/acp-15-8739-2015

76. Schumann U, Hempel R, Flentje H, et al. Contrail study with ground-based cameras. *Atmos Meas Tech*. 2013;6(12):3597-3612. doi:10.5194/amt-6-3597-2013

77. Graf K, Schumann U, Mannstein H, Mayer B. Aviation induced diurnal North Atlantic cirrus cover cycle. *Geophys Res Lett*. 2012;39(16).

78. Gierens K, Spichtinger P. On the size distribution of ice-supersaturated regions in the upper troposphere and lowermost stratosphere. In: *Annales Geophysicae*. Vol 18. Springer; 2000:499-504.

79. Spichtinger P, Gierens K, Leiterer U, Dier H. Ice supersaturation in the tropopause region over Lindenberg, Germany. *Meteorol Zeitschrift*. 2003;12(3):143-156.

80. Dickson NC, Gierens KM, Rogers HL, Jones RL. Probabilistic description of ice-supersaturated layers in low resolution profiles of relative humidity. *Atmos Chem Phys*. 2010;10(14):6749-6763. doi:10.5194/acp-10-6749-2010

81. ICAO. *Air Traffic Management - Procedures for Air Navigation Services*. Vol Doc 4444. Sixteenth. Montreal, Canada: International Civil Aviation Organisation; 2016. http://flightservicebureau.org/wp-content/uploads/2017/03/ICAO-Doc4444-Pans-Atm-16thEdition-2016-OPSGROUP.pdf.

82. Nuic A, Poles D, Mouillet V. BADA: An advanced aircraft performance model for present and future ATM systems. *Int J Adapt Control Signal Process*. 2010;24(10):850-866. doi:10.1002/acs.1176

83. Harada A, Miyamoto Y, Miyazawa Y, Funabiki K. Accuracy evaluation of an aircraft performance model with airliner flight data. *JSASS Aerosoace Tech Japan*. 2013. https://www.jstage.jst.go.jp/article/tastj/11/0/11_TJSAS-D-13-00017/_article/-char/ja/. Accessed February 11, 2019.

84. Joos F, Roth R, Fuglestvedt JS, et al. Carbon dioxide and climate impulse response functions for the computation of greenhouse gas metrics: a multi-model analysis. *Atmos Chem Phys*. 2013;13(5):2793-2825. doi:10.5194/acp-13-2793-2013

85. Wilkerson JT, Jacobson MZ, Malwitz A, et al. Analysis of emission data from global commercial aviation: 2004 and 2006. *Atmos Chem Phys*. 2010;10(13):6391-6408.

86. NASA. By the Numbers | Earth – NASA Solar System Exploration. https://solarsystem.nasa.gov/planets/earth/by-the-numbers/. Accessed November 27, 2019.

87. Reid GC, Gage KS. Interannual variations in the height of the tropical tropopause. *J Geophys Res*. 1985;90(D3):5629. doi:10.1029/JD090iD03p05629

88. Schumann U, Mayer B. Sensitivity of surface temperature to radiative forcing by contrail cirrus in a radiative-mixing model. *Atmos Chem Phys, 17, 13833–13848*. 2017. doi: 10.5194/acp-17-13833-2017.